

UNIVERSITÀ DI PISA

Scuola di Dottorato in Ingegneria “Leonardo da Vinci”



Corso di Dottorato di Ricerca in
Ingegneria dell'Informazione

SSD: ING-INF/03

Tesi di Dottorato di Ricerca

Physical Layer Techniques for Wireless Communication Systems

Autore:

Leonardo Marchetti

Relatori:

Prof. Ruggero Reggiannini

Prof. Michele Morelli

Dr. Luca Sanguinetti

Anno 2015

Sommario

La crescente diffusione di dispositivi mobili dotati sempre e ovunque di connessioni affidabili ed idonee a supportare l'utilizzo delle più comuni applicazioni, ha richiesto negli ultimi anni la messa in opera di reti di telecomunicazioni basate su tecnologie in grado di rispondere efficacemente alle richieste del mercato, in continua crescita ed ancora lontane da livelli di saturazione.

Le tecniche di trasmissione multiportante, utilizzate ampiamente negli standard per reti locali (Wi-Fi) e per reti metropolitane (WiMAX) e già da anni oggetto di ricerca, sono state adottate definitivamente a partire dalla quarta generazione di sistemi di comunicazione cellulare (LTE). L'impiego di tali tecniche di segnalazione, se da una parte risulta di notevole vantaggio nel contrastare effetti deleteri che si riscontrano in ambienti con canale di propagazione particolarmente ostile, dall'altra pone dei requisiti molto stringenti per quanto riguarda la sensibilità ad errori di recupero del carrier frequency offset (CFO) con il conseguente impatto sulla corretta rivelazione del segnale.

È in questo ambito che si focalizza la tesi, andando ad investigare alcuni aspetti legati alle procedure di sincronizzazione per sistemi basati su segnalazione multiportante. Si farà riferimento in particolare ad una procedura utilizzata per l'associazione di un utente ad una rete radiomobile in sistemi LTE, a soluzioni per il recupero del CFO in sistemi basati su OFDM e filtered multitone modulation e ad uno studio di tecniche di recupero del CFO in ricevitori a conversione diretta.

Altri contributi inerenti a problematiche di strato fisico in sistemi di comunicazione, sia radio che su portante acustico, completano la tesi.

Abstract

The increasing diffusion of mobile devices requiring, everywhere and every time, reliable connections able to support the more common applications, induced in the last years the deployment of telecommunication networks based on technologies capable to respond effectively to the ever-increasing market demand, still a long way off from saturation level.

Multicarrier transmission techniques employed in standards for local networks (Wi-Fi) and metropolitan networks (WiMAX) and for many years hot research topic, have been definitely adopted beginning from the fourth generation of cellular systems (LTE). The adoption of multicarrier signaling techniques if on one hand has brought significant advantages to counteract the detrimental effects in environments with particularly harsh propagation channel, on the other hand, has imposed very strict requirements on sensitivity to recovery errors of the carrier frequency offset (CFO) due to the resulting impact on correct signal detection.

The main focus of the thesis falls in this area, investigating some aspects relating to synchronization procedures for system based on multicarrier signaling. Particular reference will be made to a network entry procedure for LTE networks and to CFO recovery for OFDM, filtered multitone modulation and direct conversion receivers.

Other contributions pertaining to physical layer issues for communication systems, both radio and over acoustic carrier, conclude the thesis.

Contents

List of Figures	ix
List of Tables	xiii
List of Symbols and Operators	xv
List of Acronyms	xvii
1 Introduction	1
1.1 Motivation	1
1.2 Organization of the thesis and major contributions	5
2 Random Access for Long-Term Evolution Networks	9
2.1 Introduction	9
2.2 System description and signal model	12
2.3 Problem formulation	14
2.4 RA algorithm based on the GLRT criterion	16
2.4.1 Code detection and timing estimation	16
2.4.2 Power estimation	17
2.4.3 Implementation and complexity analysis	18
2.5 Numerical results	21
2.5.1 System parameters	21
2.5.2 Performance evaluation	21
2.5.3 Computational complexity	27
2.6 Concluding remarks	27

3	Frequency Estimation and Preamble Identification in OFDMA Systems	29
3.1	Introduction	29
3.2	System model	32
3.3	ML frequency estimation	35
3.3.1	Derivation of the ML estimator	35
3.3.2	Accuracy and estimation range of MLE	36
3.3.3	Implementation and complexity analysis of MLE	39
3.3.4	Low-complexity estimation of the FFO	40
3.4	Estimation of the integral CFO and preamble index	41
3.4.1	Derivation of the joint ML estimator	41
3.4.2	Simplification of the joint ML estimator	43
3.4.3	Remarks	45
3.5	Simulation results	46
3.5.1	System parameters	46
3.5.2	Performance assessment	47
3.5.3	Complexity comparison	52
3.6	Concluding remarks	52
3.7	Appendix	53
4	Frequency Estimation in OFDM Direct-Conversion Receivers	55
4.1	Introduction	55
4.2	Signal model in the presence of I/Q imbalance	58
4.2.1	Direct conversion receiver	58
4.2.2	Signal model	60
4.3	CFO estimation in the absence of I/Q imbalance	62
4.3.1	Estimator's design	62
4.3.2	Performance analysis	62
4.3.3	Remarks	63
4.4	Joint ML estimation of the unknown parameters	64
4.4.1	Estimator's design	64
4.4.2	Performance analysis	65
4.4.3	Remarks	66
4.5	Constrained joint ML estimation of the unknown parameters	67

4.5.1	Estimator's design	67
4.5.2	Remarks	68
4.6	CRB analysis	69
4.7	Simulation results	71
4.7.1	Simulation model	71
4.7.2	Performance assessment for FO estimation	72
4.8	Concluding remarks	78
	Appendix A	79
	Appendix B	80
	Appendix C	82
5	Carrier Frequency Recovery for Filtered Multitone Modulations	83
5.1	Introduction	83
5.2	Signal and channel models	85
5.3	CFO estimation algorithm	85
5.3.1	Exact ML estimator	87
5.3.2	Approximate ML estimator	87
5.4	System definition and simulation results	88
5.4.1	Signal format	88
5.4.2	Pilot pattern	88
5.4.3	Impact of PP on acquisition range	90
5.4.4	Channel estimator	90
5.4.5	Simulation results	91
5.5	Concluding remarks	94
6	Distributed Power Control over Interference Channels	95
6.1	Introduction	95
6.2	System model and problem formulation	97
6.3	Game formulation	98
6.4	Distributed algorithm	99
6.5	Simulation results	102
6.6	Concluding remarks	106

7	An Efficient Receiver Structure for Underwater Acoustic Commu- nications	107
7.1	Introduction	107
7.2	Signal and channel models	109
7.3	Modem architecture	111
7.4	Timing and channel estimation	112
7.5	Design issues and hardware implementation	115
7.5.1	Conditions for path resolvability	115
7.5.2	Merging branch outputs	117
7.5.3	Hardware implementation	118
7.6	Experimental results	121
7.7	Concluding remarks	127
8	VFIDES - An Autonomous Vehicle for Underwater Identification, Detection and Exploration	129
8.1	Introduction	129
8.1.1	Features of the acoustic sensors and radio equipment	130
8.1.2	Selection and performance evaluation of radio and sonar systems	131
8.1.3	Integration of acoustic and radio equipment	131
8.2	Experimental tests	131
8.2.1	Hydrophone testing and calibration	132
8.2.2	Pool test of the acoustic communication system	134
8.2.3	Radio modem test over the sea surface	136
8.2.4	The VFIDES	138
	Conclusions	139
	Bibliography	141

List of Figures

1.1	Active mobile-broadband subscriptions in developed countries per 100 inhabitants.	2
2.1	Block diagram of the receiver for a RA scheme based on GLRT.	20
2.2	$\text{var}(\hat{\theta}_1)$ vs. M_θ for GLRT-RA with $K = 1$, $R = 1$ and different SNR values.	22
2.3	$\text{var}(\hat{\theta}_1)$ vs. SNR for the investigated schemes with $K = 1$ and $R = 1$	22
2.4	$\text{nvar}(\hat{p}_1^{(f)})$ vs. M_P for GLRT-RA with $K = 1$, $R = 1$ and different SNR values.	23
2.5	$\text{nvar}(\hat{p}_1^{(f)})$ vs. the SNR for the investigated schemes with $K = 1$ and $R = 1$	24
2.6	$\text{var}(\hat{\theta}_1)$ vs. the SNR for GLRT-RA with $K = 1$ and $R = 1, 2$ or 4	25
2.7	$\text{nvar}(\hat{p}_1^{(f)})$ vs. the SNR for GLRT-RA with $K = 1$ and $R = 1, 2$ or 4	25
2.8	$\text{var}(\hat{\theta}_1)$ vs. K for GLRT-RA when SNR= 12 dB and $R = 1$ or 4	26
2.9	$\text{nvar}(\hat{p}_1^{(f)})$ vs. K of GLRT-RA when SNR= 12 dB and $R = 1$ or 4	26
3.1	Expectation of the CFO metric obtained at SINR = 10 dB using the IEEE 802.16e training preamble.	37
3.2	Estimation error $\nu - \hat{\nu}_{MLE}$ over 10^3 runs for SINR = 10 dB using the IEEE 802.16e preamble.	38
3.3	MSE of the FFO estimates provided by MLE and LCE versus SINR.	48
3.4	Probability of failure versus SINR for $\tau_d = 0$ and $\hat{\varepsilon} = \varepsilon$	49
3.5	Probability of failure versus SINR for $\tau_d = 20$ and $\hat{\varepsilon} = \varepsilon$	49
3.6	Probability of failure versus SINR for $\tau_d = 40$ and $\hat{\varepsilon} = \varepsilon$	50

3.7	Probability of failure versus τ_d for SINR=-10 dB and $\hat{\varepsilon} = \varepsilon$	51
3.8	Probability of failure versus $\Delta\varepsilon$ for SINR=-10 dB and $\tau_d = 20$	51
4.1	Basic architecture of a direct-conversion receiver.	58
4.2	Baseband equivalent of the receiver front-end.	59
4.3	Accuracy of CJML vs δ for different SNR values in the severe I/Q imbalance scenario.	73
4.4	Accuracy of the CFO estimators vs φ in the severe I/Q imbalance scenario with SNR = 15 dB.	74
4.5	Accuracy of the CFO estimators vs φ in the moderate I/Q imbalance scenario with SNR = 15 dB.	74
4.6	Accuracy of the CFO estimators vs φ in the severe I/Q imbalance scenario with SNR = 30 dB.	75
4.7	Accuracy of the CFO estimators vs φ in the moderate I/Q imbalance scenario with SNR = 30 dB.	76
4.8	Accuracy of the CFO estimators vs SNR in the severe I/Q imbalance scenario.	77
4.9	Accuracy of the CFO estimators vs SNR in the moderate I/Q imbalance scenario.	77
5.1	From top to bottom: PP1, PP2, PP3. P = pilot, D = data.	89
5.2	MSEE vs. ν for the SF scenario; $E_s/N_0 = 15$ dB.	92
5.3	MSEE vs. ν for the FF scenario; $E_s/N_0 = 15$ dB.	92
5.4	FER vs. E_b/N_0 for the SF scenario.	93
5.5	FER vs. E_b/N_0 for the FF scenario.	94
6.1	SINR vs. number of packets when $K = 4$ and $\beta = 0.9$	103
6.2	Transmit power vs. number of packets when $K = 4$ and $\beta = 0.9$	103
6.3	SINR vs. number of packets when $K = 6$ and $\beta = 0.9$	104
6.4	Transmit power vs. number of packets when $K = 6$ and $\beta = 0.9$	104
6.5	SINR vs. number of packets when $K = 4$ and $\beta = 0.5$	105
6.6	SINR vs. number of packets with $\beta = 0.9$	105
7.1	Modem architecture.	111

7.2	A sample correlation function (square modulus). The vertical scale is arbitrary.	114
7.3	Power spectral density of the received signal after downconversion/de-spreading of the strongest path ($k = 0$). The vertical scale is arbitrary. The system parameters are the same as in Fig. 7.1 and are specified in Tabs. 7.1–7.3.	117
7.4	Test bench: NI chassis hosting controller and data acquisition board, PC with LabView, spectrum analyzer.	119
7.5	Transmitted signal displayed on spectrum analyzer.	119
7.6	LabView control interface: particular of the main control panel. . . .	120
7.7	LabView control interface: particular of the analysis tools.	120
7.8	A functional block of the synchronization circuitry (LabView code). .	121
7.9	Ray tracing produced by <i>Bellhop</i>	121
7.10	Geometry of the UWA link.	122
7.11	BER vs SNR, uncoded transmission, 3-path channel, single-branch and three-branch receivers.	124
7.12	BER vs SNR, coded transmission, 3-path channel, single-branch and three-branch receivers.	125
7.13	RMSEE vs SNR, 3-path channel, delay estimate for $k = 0, 1, 2$	126
8.1	Particular of the test pool with the bridge crane and the rotating shaft. .	132
8.2	Hydrophone under testing.	133
8.3	Projectors used throughout the tests.	133
8.4	Detail of the USBL modem.	134
8.5	Detail of the modem hanged on a winch before the immersion.	135
8.6	Modems lowered in the test pool.	135
8.7	Receiving station during the test on Massaciuccoli lake.	136
8.8	Transmitting station during the test in Viareggio.	137
8.9	Detail of the modem connections to control station and antenna. . . .	137
8.10	Paths of the tested radio links highlighted on a map.	138
8.11	The VFIDES.	138

List of Tables

3.1	Complexity of MLE and LCE for FFO recovery.	40
3.2	Complexity of AMLE and CE for the joint recovery of IFO and preamble index.	46
7.1	Main acoustic and geometric parameters of the UWA scenario.	122
7.2	Power-delay profile for the 3-path channel.	123
7.3	Physical layer parameters.	123

List of Symbols and Operators

modulus	$ \cdot $
conjugate transposition	$(\cdot)^H$
floor function (rounding downward)	$\lfloor \cdot \rfloor$
transposition	$(\cdot)^T$
Euclidean norm	$\ \cdot\ $
vector	\mathbf{x}
expectation	$\mathbb{E}\{\cdot\}$
complex conjugation	$(\cdot)^*$
matrix	\mathbf{X}
diagonal matrix with entries $a(n)$ along its main diagonal	$\text{diag}\{a(n)\}$
identity matrix of order N	\mathbf{I}_N
null matrix of order N	$\mathbf{0}_N$
inverse of a matrix \mathbf{A}	\mathbf{A}^{-1}
modulo- δ operation reducing x to the interval $[-\delta/2, \delta/2)$	$(x)_{\text{mod } \delta}$
argument	$\arg\{\cdot\}$
real part	$\Re\{\cdot\}$
imaginary part	$\Im\{\cdot\}$
(k, ℓ) th entry of a matrix \mathbf{A}	$[\mathbf{A}]_{k, \ell}$
trial value of an unknown parameter λ	$\tilde{\lambda}$

List of Acronyms

3GPP	Third-Generation Partnership Project
ACK	acknowledgement
ACRB	asymptotic CRB
AR	acquisition range
AUV	autonomous underwater vehicle
AWGN	additive white gaussian noise
BER	bit error rate
BS	base station
CFO	carrier frequency offset
CINR	channel-to-interference-plus-noise ratio
CIR	channel impulse response
CP	cyclic prefix
CRB	Cramer-Rao bound
CSI	channel state information
DAC	digital-to-analog converter
DCR	direct-conversion receiver

DFT	discrete Fourier transform
DL	downlink
DS-SS	direct-sequence spread-spectrum
FDD	frequency division duplexing
FER	frame error rate
FFO	fractional frequency offset
FFT	fast Fourier transform
FMT	filtered multitone
GLRT	generalized likelihood ratio test
GNE	generalized Nash equilibrium
IBI	interblock interference
ICI	inter-cell interference
IDFT	inverse DFT
IF	intermediate-frequency
IFO	integral frequency offset
IR	initial ranging
I/Q	in-phase/quadrature
LLF	log-likelihood function
LO	local oscillator
LPF	low-pass filter
LTE	Long-Term Evolution
MAI	multiple-access interference
MIMO	multiple-input multiple-output

ML	maximum-likelihood
MRC	maximal ratio combining
MSEE	mean square estimation error
MT	mobile terminal
NACK	negative ACK
OFDM	orthogonal frequency-division multiplexing
OFDMA	orthogonal frequency-division multiple-access
PA	pilot aided
PN	pseudo-noise
PP	pilot pattern
PRACH	Physical Random Access Channel
QoS	quality of service
RA	random access
RF	radio-frequency
RHS	right-hand side
RMSEE	root mean square estimation error
S2C	sweep-spread carrier
SC-FDMA	single-carrier frequency- division multiple-access
SC	subcarrier
SINR	signal-to-noise-plus-interference ratio
SIR	signal-to-image ratio
SNR	signal-to-noise ratio
TDD	time division duplexing

TEDS	TETRA Release 2 Enhanced Data Service
TP	training preamble
UE	user equipment
UL	uplink
UWA	underwater acoustic
WGN	white gaussian noise
WLAN	wireless local area network
WMAN	wireless metropolitan area network
ZC	Zadoff-Chu
ZMCSG	zero-mean circularly-symmetric gaussian

Chapter 1

Introduction

1.1 Motivation

The ever-increasing coverage with high-speed connectivity via cellular and wireless networks, the widespread diffusion of mobile devices such as smartphones, tablets, notebooks and the resulting popularization of many useful or trendy applications, have changed the way we communicate, our lifestyle and working habits. Taking as reference some simple data [1], allows us to get an impression of how the mobile technology has already become pervasive and ubiquitous. For example Fig. 1.1 shows the trend of active mobile-broadband subscriptions in developed countries as indicated by the International Telecommunication Union and consisting primarily of connections via mobile cellular phones, USB dongle/modem or add-on data packages. We can observe how this surprising increase, started in 2007 (year of the beginning for this time series), has led to a penetration greater than eighty broadband subscriptions for one hundred inhabitants, with 2.3 billion of world-wide subscriptions reached during 2014 and a double-digit growth rate on annual basis. Other interesting data, to give a big picture of the *information era* we are going through, are the number of mobile-cellular subscriptions, that has overtaken during 2014 the level of 6.9 billion in the world (one for inhabitant on average!), and the global number of individuals using the Internet, greater than 2.9 billion in the entire world with a peak of 78 percent of the population in the developed countries.

In view of this, it is easy to figure out that the general trend is to rapidly reach,

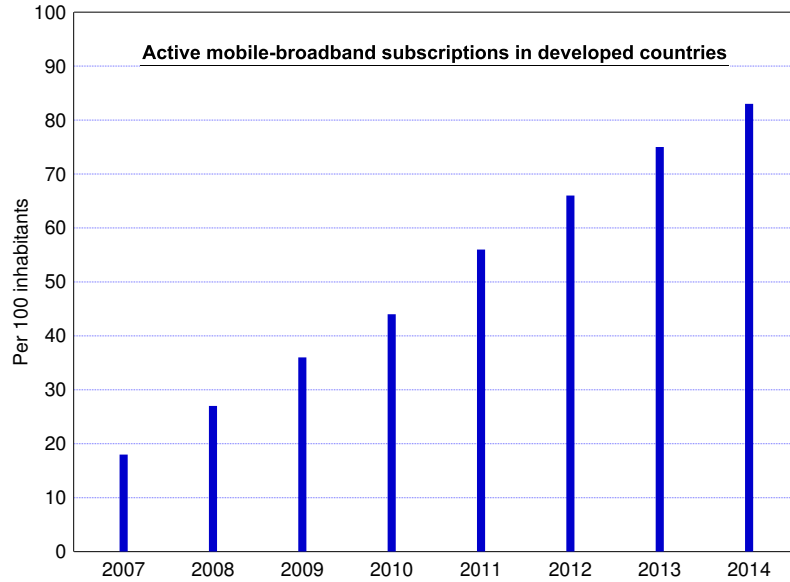


Figure 1.1: *Active mobile-broadband subscriptions in developed countries per 100 inhabitants.*

at least in developed areas, an almost total diffusion of broadband services and, at the same time, a replacement or coexistence of mobile-cellular devices with mobile broadband connections.

Going into more technical details, wireless communication systems, that already nowadays provide wideband access to a large numbers of subscribers, will be required to guarantee more and more demanding quality of service requirements in terms of coverage area, connection reliability, data rate and so on.

The design challenges for the communication system engineers, many and difficult, arise primarily but not only, from the scarcity of frequency spectrum, the limitation on total transmit power and the nature of wireless channel. For the latter, the issues to face are principally due to broadband communication with mobile devices and in general to the need of self-adapting receiving algorithms able to operate in a rapidly changing environment both in time and in space. All this motivated and inspired the huge effort of the research activity in the field, of both academia and industry.

One of the previously cited challenges, the harsh nature of the communication channel, is principally due to the phenomena of scattering, diffraction, reflection

and Doppler effects to which the radiated electromagnetic waves arriving at the receiving antennas are subjected. As a result, the receiver observes the superposition of several attenuated and delayed copies of the transmitted signal. The constructive or destructive combination of these copies causes large fluctuations in the received signal strength with a corresponding degradation of the link quality. Moreover the unpredictable variations of the propagation environment characteristics and the relative motion between transmitter and receiver lead to a randomly time varying channel. A further and very tricky impairment of wireless transmissions may be the interference arising from channel reuse.

The adoption of a multicarrier air-interface is a common feature of many current wireless standards for high-rate wireless communication and can efficiently cope with the previously problems. Some examples of largely adopted commercial implementations of these standards are Wi-Fi, WiMAX, LTE, TEDS, DVB-T. The main idea behind multicarrier signaling is to split the high-rate data stream into many low-rate substreams. The substreams are then transmitted simultaneously over orthogonal narrowband subchannels characterized by partially overlapping spectra. If the system parameters are properly tuned, each orthogonal subchannel can be approximated as a flat fading channel with constant channel gain and with respect to single-carrier transmissions, this technique can provide the system with increased resistance against narrowband interference and channel distortions. Furthermore, the adoption of multicarrier transmission ensures a high level of flexibility since transmission parameters like power, constellation size and coding rate can be selected independently over each subchannel and can also be combined with conventional multiple-access techniques to operate in a multiuser scenario. Even though the basic principle of multicarrier signaling techniques is well established among researchers and communication engineers, their practical implementation is far from being trivial as it requires rather sophisticated signal processing techniques in order to fully achieve the attainable system performance. Furthermore, practical algorithms implementation must be able to guarantee a real-time execution, often a very tight constraint, which makes the computational complexity an additional aspect to be tackled. Synchronization, channel estimation and radio resource management are only a few examples of the numerous challenges related to multicarrier technology.

Among the recalled physical layer design aspects, that if correctly designed can lead to an efficient, reliable, and robust wireless multicarrier communication system, a

major (and often key) role is played by the synchronization procedures. Essentially, these functions aim at retrieving some reference parameters from the received signal that are necessary for reliable data detection.

A fundamental synchronization task discussed within this work is relevant to the network searching procedure accomplished when a mobile device is switched on for the first time, during an handover, or if synchronization is lost. Power adjustment, timing offset estimation, and synchronization between a base station (BS) and all users within a cell are done through this process. The complexity arises from the fact that the uplink waveform arriving at the BS is a mixture of signals transmitted by different users, each characterized by different timing and frequency offsets.

Other contributions of this thesis address the problem of carrier frequency offset (CFO) recovery in multicarrier systems. The CFO is a frequency error between the received carrier and the local oscillator used for signal demodulation and results in a loss of orthogonality among subcarriers with ensuing limitations of the system performance. Frequency synchronization aims at restoring orthogonality by compensating for any frequency offset caused by oscillator inaccuracies or Doppler shifts. In particular the CFO problem is here discussed for OFDMA-based systems, filtered multitone modulations and for OFDM direct-conversion receivers, an alternative wireless receiver architecture to superheterodyne that offers significant advantages in terms of cost, package size, and power consumption.

A further section is devoted to describe an algorithm developed for a network composed of several single-antenna transmitter-receiver pairs. The target in this case is the minimization of the power required to achieve a given signal-to-interference-plus-noise ratio in a limited-feedback scenario and the proposed solution is based on a non-cooperative game.

The thesis is completed by two contributions relevant to underwater acoustic communications. The former treats an enhanced modem structure using a particular wideband communication technique with a focus on synchronization issues, while the latter shows some highlight on the design of the communication and sensor subsystems for an autonomous underwater vehicle.

To better appreciate the contents of this dissertation some theoretical basis are needed. For the first part the reader can refer to [2] for an excellent introduction to synchronization issues in multicarrier systems with particular reference to OFDM, while an interesting introduction to filtered multitone modulations is reported in [3].

For the mathematical and theoretical foundation of the estimation theory, [4] is an optimum reference, while for general digital communication basis [5] can be consulted. The foundation of game theory, useful to understand the theoretical framework of one contribution of the thesis, can be found in [6]. Finally, an excellent treatise of underwater acoustic is [7].

1.2 Organization of the thesis and major contributions

The thesis is organized as follows.

In **Chapter 2** a novel Random Access algorithm for initial synchronization in LTE systems is derived on the basis of a generalized likelihood ratio test. In contrast to existing alternatives, the proposed approach provides better results by properly taking into account the frequency selectivity of the channel. Computer simulations are employed to assess the effectiveness of the proposed solution and to make comparisons with existing alternatives.

In **Chapter 3** the joint maximum likelihood (ML) estimation of the CFO and preamble index in a multicarrier system compliant with the WiMAX specifications is investigated, and a novel expression of the relevant Cramer-Rao bound (CRB) is derived. Since the exact ML solution is prohibitively complex in its general formulation, suboptimal algorithms are developed which can provide a reasonable trade-off between estimation accuracy and processing load. Specifically, it is shown that the fractional CFO can be recovered by combining the ML estimator with an existing algorithm that attains the CRB in all practical scenarios. The integral CFO and preamble index are subsequently retrieved by a suitable approximation of their joint ML estimator. Compared to existing alternatives, the resulting scheme exhibits improved accuracy and reduced sensitivity to residual timing errors.

In **Chapter 4** the problem of CFO recovery in an OFDM receiver affected by frequency-selective in-phase/quadrature (I/Q) imbalances is investigated. The analysis is based on ML methods and relies on the transmission of a training preamble with a repetitive structure in the time domain. After assessing the accuracy of the conventional ML (CML) scheme in a scenario characterized by I/Q impairments, the joint ML (JML) estimator of all unknown parameters is reviewed and its theoretical

performance is evaluated. In order to improve the estimation accuracy a novel CFO recovery method that exploits some side-information about the signal-to-interference ratio is also presented. It turns out that both CML and JML can be derived from this scheme by properly adjusting the value of a design parameter. The accuracy of the investigated methods are compared with the relevant CRB. These results can be used to check whether conventional CFO recovery algorithms can work properly or not in the presence of I/Q imbalances and also to measure the potential gain achievable by more sophisticated schemes.

Chapter 5 is concerned with ML pilot-aided frequency offset recovery for filtered multitone modulations such as that employed in TETRA Release 2 Enhanced Data Service (TEDS). An approach is proposed improving on previously published algorithms. When pilot symbols are arranged on a rectangular time-frequency grid, the acquisition range of a pilot-based frequency synchronizer may occur to be very narrow as it cannot exceed the inverse of pilot spacing in the time domain. It is shown here that the above drawback can be relieved resorting to a non-rectangular pilot pattern where the pilot symbols are simply shifted in time along the subcarriers with respect to the rectangular arrangement.

Chapter 6 presents a network composed of several single-antenna transmitter-receiver pairs in which each pair aims at selfishly minimizing the power required to achieve a given signal-to-interference-plus-noise ratio. This is obtained modeling the transmitter-receiver pairs as rational agents that engage in a non-cooperative game. Capitalizing on the well-known results on the existence and structure of the generalized Nash equilibrium (GNE) point of the underlying game, a low complexity, iterative and distributed algorithm is derived to let each terminal reach the GNE using only a limited feedback in the form of link-layer acknowledgement (ACK) or negative acknowledgement (NACK). Numerical results are used to prove that the proposed solution is able to achieve convergence in a scalable and adaptive manner under different operating conditions.

In **Chapter 7** an improved receiver architecture for Sweep-Spread-Carrier (S2C) modulation is presented. S2C is a spread-spectrum technique recently proposed to effectively contrast the effects of time dispersion over multipath propagation channels in underwater acoustic wireless links. The proposed structure is capable to take advantage of the energy received from all propagation paths rather than only from the strongest one, as envisaged in previous works dealing with this modulation technique.

A hardware version of the modem was implemented in laboratory and its behavior was assessed and compared, using standard propagation models, to that exhibited by the traditional single-path-based scheme in terms of bit error rate. Results are presented showing that gains of a few decibels of signal-to-noise-plus-interference ratio can be achieved. Issues relevant to carrier/symbol synchronization and channel estimation are also addressed.

In **Chapter 8** an overview of the VFIDES project is reported for completeness as it represented a substantial part of the doctoral activity. The project was carried out in collaboration with *Whitehead Sistemi Subacquei (WASS)* located in Livorno and other high-tech companies. *WASS* is a *Finmeccanica* leading company operating in the sector of advanced underwater systems. The goal of the project is the development of an innovative autonomous underwater vehicle with advanced capabilities. The main tasks were inherent to the selection, simulation and integration activities concerning communication and sensor subsystems of the vehicle. Unlike the other contributions within the thesis, for this activity, only a high level description is reported being this topic far from the main theme of the thesis and because many project details and obtained results pertain to industrial classified information.

Finally some **Conclusions** are given.

Chapter 2

Random Access for Long-Term Evolution Networks

2.1 Introduction

Long-term evolution (LTE) has been introduced by the Third-Generation Partnership Project (3GPP) in order to face the ever-increasing demand for packet-based mobile broadband communications. This emerging technology employs orthogonal frequency-division multiple-access (OFDMA) for downlink transmission and single-carrier frequency-division multiple-access (SC-FDMA) in the uplink [8]. To maintain orthogonality among subcarriers of different users, the 3GPP-LTE specifies a network entry procedure called random access (RA) by which uplink signals can arrive at the eNodeB aligned in time and with approximately the same power level [9], [10].

In its basic form, the RA function is a contention-based procedure, which essentially develops through the same steps specified by the Initial Ranging (IR) process of the IEEE 802.16 wireless metropolitan area network [11]. Specifically, each user equipment (UE) trying to enter the network computes frequency and timing estimates on the basis of a suitably designed downlink control channel. The estimated parameters are next used in the subsequent uplink phase, during which the UE selects a time-slot

and transmits a randomly chosen code over the Physical Random Access Channel (PRACH), which is composed by a specified set of adjacent subcarriers. The codes are obtained by applying different cyclic shifts to a Zadoff-Chu (ZC) sequence so as to ensure their mutual orthogonality [12]. As a consequence of the different terminals' positions within the cell, uplink signals are subject to users' specific propagation delays and arrive at the eNodeB at different time instants. After identifying which codes are actually present in the PRACH (active codes), the eNodeB must extract the corresponding timing and power information. Then, it will broadcast a response message indicating the detected codes and giving instructions for timing and power adjustment.

From the above discussion, it follows that code identification as well as multiuser timing and power estimation are the main tasks of the eNodeB during the RA process. These problems have received great attention in the last few years and some solutions are currently available [13]–[22]. The methods illustrated in [13] and [14] perform code detection and timing recovery by correlating the received samples with time-shifted versions of a training sequence. The code is detected if the correlation peak exceeds a specified threshold, with the peak position providing the timing information. Since these schemes operate in the time-domain, they are not suited for multicarrier systems, wherein users' codes are transmitted over a subset of the available subcarriers. In such a case, the frequency-domain correlation approach outperforms its time-domain counterpart as it can easily extract the PRACH from data-bearing subcarriers [15]. A simple energy detector is employed in [16] to reveal the presence of a network entry request. However, since this approach requires that the user's codes are real-valued, it cannot be applied to the ZC sequences employed in the LTE. A timing recovery scheme devised for the LTE uplink is discussed in [17]. Here, the PRACH is firstly extracted from the uplink multiuser signal by means of a discrete Fourier transform (DFT) operation. Then, the corresponding frequency-domain samples are multiplied by the root ZC sequence and converted in the time-domain using an inverse DFT (IDFT) device. The code detection process searches for the peak of the resulting timing metric within an observation window that is univocally specified by the cyclic shift associated to the tested code. If the peak exceeds a suitably designed threshold, the code is declared to be active and the corresponding timing estimate is obtained as the difference between the peak location and the beginning of the observation window. This method is expected to work properly as long as the received codes

maintain their orthogonality after passing through the propagation channel. In the presence of multipath distortions, however, the PRACH subcarriers may experience different attenuations and phase shifts, thereby leading to a loss of code orthogonality. This gives rise to multiple-access interference (MAI), which may severely degrade the code detection capability.

Possible approaches to mitigate the MAI are proposed in [18]–[22]. More precisely, in [18] the users' codes are divided into several groups which are mapped over exclusive sets of subcarrier in order to make them perfectly separable in the frequency domain. In the signal design illustrated in [19], the codes are transmitted in the time direction over a specified number of OFDMA blocks. This way, the code orthogonality is maintained as long as the channel response keeps constant over the entire transmission slot. However, using a relatively large number of OFDMA blocks increases the sensitivity to residual carrier frequency offsets (CFOs), which may compromise the orthogonality of the received codes. Ranging schemes that are robust to frequency errors are presented in [20] and [21], where users' CFOs are estimated by resorting to subspace-based methods. In [22], the generalized likelihood ratio test (GLRT) criterion is applied to decide whether a given code is present or not in the ranging subchannel. The proposed scheme is fully compliant with the IEEE 802.16 specifications and inherently takes into account the multipath distortions introduced by the propagation channel.

Despite their resilience to MAI, the schemes discussed in [18]–[22] are based on signal designs that cannot be supported by the PRACH structure and, accordingly, they are not suited for LTE systems.

In this chapter, we derive a novel RA method which is specifically tailored for LTE applications with single or multiple receive antennas and makes use of the generalized likelihood ratio test (GLRT) to decide whether a given code is present or not in the PRACH. In formulating our testing problem, the PRACH is divided into sub-bands referred to as *tiles*, each composed by a certain number of *adjacent* subcarriers over which the channel is assumed to be constant. The timing error and the channel frequency response of the hypothesized codes are assumed to be unknown and are jointly estimated using the maximum-likelihood (ML) criterion. The power level of the detected codes is eventually retrieved from the estimated channel frequency response. Compared to [17], our approach provides the system with improved resilience against multipath distortions. However, this advantage is achieved at the price of an increase of the system complexity.

2.2 System description and signal model

Our system is compliant with the LTE-3GPP standard for wireless data communications. We denote by B the available bandwidth and assume that K UEs are simultaneously trying to enter the network. As mentioned previously, each UE notifies its entry request by transmitting a randomly chosen code over the PRACH. According to the standard, a set \mathcal{C} of 64 different RA codes are available in each cell. These codes are generated by cyclically shifting one or more ZC root sequences of prime-length $N_{ZC} = 839$. Specifically, denoting by

$$\xi_u(n) = e^{-j\pi un(n+1)/N_{ZC}} \quad n = 0, 1, \dots, N_{ZC} - 1 \quad (2.1)$$

the elements of the u th ZC root sequence, the ν th RA code obtained from $\xi_u(n)$ has entries

$$x_{u,\nu}(n) = \xi_u((n + C_\nu) \bmod N_{ZC}) \quad (2.2)$$

where C_ν denotes the ν th cyclic shift. The latter is given by $C_\nu = \nu N_{CS}$, where N_{CS} is a system parameter related to the cell radius (the larger the radius, the greater N_{CS}) and ν is an integer belonging to the set $\{0, 1, \dots, N_U - 1\}$, with $N_U = \lfloor N_{ZC}/N_{CS} \rfloor$ and $\lfloor x \rfloor$ rounding x to the smallest integer. Bearing in mind that 64 different codes must be available in \mathcal{C} and observing that a total of N_U codes are generated from a single ZC root sequence, it follows that two or more root sequences are necessary whenever $N_U < 64$. For simplicity we set $N_{CS} = 13^1$, which amounts to assuming a cell radius of approximately 1.5 km. In these circumstances we have $N_U = 64$ and, accordingly, one single root sequence is sufficient for the generation of the 64 codes in \mathcal{C} . For this reason, in the sequel we omit the root index u . Also, without loss of generality, we assume that different UEs select different codes with indices $\{1, 2, \dots, K\}$.

As specified in [9], the PRACH occupies a bandwidth $B_{RA} = 1.08 \text{ MHz}^2$ with subcarrier spacing $\Delta f_{RA} = 1.25 \text{ kHz}$. Vector $\mathbf{x}_k = [x_k(0), x_k(1), \dots, x_k(N_{ZC} - 1)]^T$ is transmitted over the PRACH subcarriers using an OFDM modulator, which comprises an IDFT unit of size $N = B/\Delta f_{RA}$ along with the insertion of a cyclic prefix and a guard time of N_{CP} and N_{GT} samples, respectively. This produces the $N_B =$

¹All the provided results can be easily extended to different values of N_{CS} .

²This value corresponds to the smallest uplink bandwidth of six resource blocks in which LTE may operate.

$N + N_{CP} + N_{GT}$ time-domain samples given by

$$s_k(l) = \begin{cases} b_k(l) & 0 \leq l \leq N + N_{CP} - 1 \\ 0 & N + N_{CP} \leq l \leq N_B - 1 \end{cases} \quad (2.3)$$

where

$$b_k(l) = \frac{1}{\sqrt{N}} \sum_{n=0}^{N_{ZC}-1} x_k(n) e^{j2\pi i_n l / N} \quad (2.4)$$

with i_n being the frequency index of the n th PRACH subcarrier. Samples $s_k(l)$ are eventually fed to a digital-to-analog converter (DAC) with impulse response $g(t)$ and signaling interval $T = 1/B$ or, equivalently, $T = 1/(N\Delta f_{RA})$. The complex envelop of the signal transmitted by the k th UE takes the form

$$z_k(t) = \sum_{\ell=0}^{N_B-1} s_k(\ell) g(t - \ell T) \quad (2.5)$$

where $g(t)$ is the DAC impulse response. This signal propagates through a multipath channel and arrives at the eNodeB, which is assumed to be equipped with R antennas. At each antenna, the received signal is down-converted to baseband and sampled at a rate $1/T$. The resulting time domain samples are next passed to an N -point DFT unit to extract the PRACH. Due to the different positions occupied by the users within the cell, the uplink signals are received at the eNodeB with specific timing offsets. We denote by θ_k the timing error of the k th UE expressed in sampling intervals. As mentioned previously, each UE performs its uplink transmission by using the frequency estimates obtained during the downlink phase. Accordingly, the received signals are also affected by the CFOs induced by downlink estimation errors and/or Doppler effects. The presence of uncompensated CFOs destroys orthogonality among PRACH subcarriers and gives rise to inter-channel interference. We assume that downlink estimation errors are within a few percents of the subcarrier spacing and consider low mobility applications characterized by negligible Doppler shifts so as to reasonably neglect any residual CFO. Moreover, we assume that users other than those performing RA have been successfully synchronized to the eNodeB so that they do not generate significant interference over the PRACH [17]. In these hypotheses, the DFT output over the i_n th subcarrier at the r th antenna can be approximated as

follows

$$Z^{(r)}(i_n) = \sum_{k=1}^K x_k(n) H_k^{(r)}(i_n) e^{-j2\pi i_n \theta_k / N} + w^{(r)}(i_n) \quad (2.6)$$

where $H_k^{(r)}(i_n)$ is the k th channel frequency response over the i_n th subcarrier at the r th antenna, while $w^{(r)}(i_n)$ accounts for background noise and is modeled as a circularly-symmetric complex Gaussian random variable with zero mean and variance σ_w^2 .

2.3 Problem formulation

The eNodeB exploits the quantities $\{Z^{(r)}(i_n)\}$ to detect the active codes and for extracting the associated timing and power information. Since it has no knowledge as to which codes are actually present in the PRACH, the summation in (2.6) must be extended over the entire code set \mathcal{C} , with the assumption that $H_k^{(r)}(i_n) = 0$ if the k th code is not active. Then, we have

$$Z^{(r)}(i_n) = \sum_{k \in \mathcal{C}} x_k(n) H_k^{(r)}(i_n) e^{-j2\pi i_n \theta_k / N} + w^{(r)}(i_n). \quad (2.7)$$

As mentioned previously, we divide the RA subcarriers into M tiles, each composed by $V = \lfloor N_{ZC}/M \rfloor$ adjacent subcarriers. We denote by $i_m + v$ the index of the v th subcarrier within the m th tile. Moreover, we assume that the channel response is nearly flat over a tile and replace the quantities $\{H_k^{(r)}(i_m + v)\}_{v=0}^{V-1}$ with an *average* frequency response given by

$$S_k^{(r)}(m) = \frac{e^{-j2\pi i_m \theta_k / N}}{V} \sum_{v=0}^{V-1} H_k^{(r)}(i_m + v). \quad (2.8)$$

In such a case, we may rewrite (2.7) as

$$Z^{(r)}(i_m + v) = \sum_{k \in \mathcal{C}} x_k(mV + v) S_k^{(r)}(m) e^{-j2\pi v \theta_k / N} + w^{(r)}(i_m + v) \quad (2.9)$$

while the power that the eNodeB receives from the k th UE is found to be

$$p_k = \frac{1}{MR} \sum_{r=0}^{R-1} \sum_{m=0}^{M-1} |S_k^{(r)}(m)|^2. \quad (2.10)$$

To proceed further, we collect the DFT outputs corresponding to the m th tile into a single vector $\mathbf{Z}^{(r)}(m) = [Z^{(r)}(i_m), Z^{(r)}(i_m + 1), \dots, Z^{(r)}(i_m + V - 1)]^T$. Then, we have

$$\mathbf{Z}^{(r)}(m) = \sum_{k \in \mathcal{C}} \mathbf{X}_k(m) \mathbf{a}(\theta_k) S_k^{(r)}(m) + \mathbf{w}^{(r)}(m) \quad (2.11)$$

where $\mathbf{w}^{(r)}(m) = [w^{(r)}(i_m), w^{(r)}(i_m + 1), \dots, w^{(r)}(i_m + V - 1)]^T$ is the noise vector, $\mathbf{X}_k(m)$ is a $V \times V$ diagonal matrix with elements $\{x_k(mV + v)\}_{v=0}^{V-1}$ along its main diagonal and $\mathbf{a}(\theta_k)$ is expressed by

$$\mathbf{a}(\theta_k) = \left[1, e^{-j2\pi\theta_k/N}, \dots, e^{-j2\pi(V-1)\theta_k/N} \right]^T. \quad (2.12)$$

Code detection is now accomplished by resorting to a single-user strategy that operates *individually* for any $\mathbf{x}_k \in \mathcal{C}$. More precisely, for each $\ell = 1, 2, \dots, |\mathcal{C}|$ (where $|\cdot|$ denotes the cardinality of the enclosed set) the eNodeB decides in favour of one of the following two hypotheses: \mathcal{H}_0) the code \mathbf{x}_ℓ is not present in the observation vector $\mathbf{Z} = [\mathbf{Z}^{(0)T}, \mathbf{Z}^{(1)T}, \dots, \mathbf{Z}^{(R-1)T}]^T$, with $\mathbf{Z}^{(r)} = [\mathbf{Z}^{(r)T}(0), \mathbf{Z}^{(r)T}(1), \dots, \mathbf{Z}^{(r)T}(M-1)]^T$; \mathcal{H}_1) \mathbf{x}_ℓ is present in \mathbf{Z} . In doing so, the contribution of the active codes \mathbf{x}_k with indices $k \neq \ell$ is treated as a disturbance term which inevitably degrades the system performance. Although suboptimal, this approach has the advantage of allowing a simple formulation of the detection problem as a composite binary hypothesis test:

$$\mathcal{H}_0 : \mathbf{Y}_\ell^{(r)}(m) = \mathbf{n}_\ell^{(r)}(m) \quad (2.13)$$

$$\mathcal{H}_1 : \mathbf{Y}_\ell^{(r)}(m) = \mathbf{a}(\theta_\ell) S_\ell^{(r)}(m) + \mathbf{n}_\ell^{(r)}(m) \quad (2.14)$$

where $\mathbf{n}_\ell^{(r)}(m)$ accounts for the contribution of MAI plus thermal noise, while $\mathbf{Y}_\ell^{(r)}(m)$ is defined as

$$\mathbf{Y}_\ell^{(r)}(m) = \mathbf{X}_\ell^H(m) \mathbf{Z}^{(r)}(m). \quad (2.15)$$

In all subsequent derivations, the entries of $\mathbf{n}_\ell^{(r)}(m)$ are modeled as statistically independent Gaussian random variables with zero mean and unknown power σ^2 .

Vector $\mathbf{Y}_\ell = [\mathbf{Y}_\ell^{(0)T}, \mathbf{Y}_\ell^{(1)T}, \dots, \mathbf{Y}_\ell^{(R-1)T}]^T$, with $\mathbf{Y}_\ell^{(r)} = [\mathbf{Y}_\ell^{(r)T}(0), \dots, \mathbf{Y}_\ell^{(r)T}(M-1)]^T$, is eventually exploited to make a decision between the two hypotheses \mathcal{H}_0 and \mathcal{H}_1 . From (2.13) and (2.14), it is seen that this task is complicated by the presence of the unknown parameters $(\mathbf{S}_\ell, \theta_\ell, \sigma^2)$, where $\mathbf{S}_\ell = [\mathbf{S}_\ell^{(0)T}, \mathbf{S}_\ell^{(1)T}, \dots, \mathbf{S}_\ell^{(R-1)T}]^T$ and $\mathbf{S}_\ell^{(r)} = [S_\ell^{(r)}(0), S_\ell^{(r)}(1), \dots, S_\ell^{(r)}(M-1)]^T$. To overcome this problem, the GLRT criterion is applied in the sequel.

2.4 RA algorithm based on the GLRT criterion

Let $\text{pdf}_{\mathcal{H}_i}$ be the probability density function (pdf) of \mathbf{Y}_ℓ under the hypothesis \mathcal{H}_i for $i = 0, 1$. Then, from (2.13) and (2.14), we have

$$\text{pdf}_{\mathcal{H}_0}(\mathbf{Y}_\ell; \sigma^2) = \frac{1}{(\pi\sigma^2)^{MVR}} e^{-\frac{1}{\sigma^2} \sum_{r=0}^{R-1} \sum_{m=0}^{M-1} \|\mathbf{Y}_\ell^{(r)}(m)\|^2} \quad (2.16)$$

and

$$\text{pdf}_{\mathcal{H}_1}(\mathbf{Y}_\ell; \mathbf{S}_\ell, \theta_\ell, \sigma^2) = \frac{1}{(\pi\sigma^2)^{MVR}} e^{-\frac{1}{\sigma^2} \sum_{r=0}^{R-1} \sum_{m=0}^{M-1} \|\mathbf{Y}_\ell^{(r)}(m) - \mathbf{a}(\theta_\ell) S_\ell^{(r)}(m)\|^2} \quad (2.17)$$

The GLRT is mathematically formulated as

$$\frac{\text{pdf}_{\mathcal{H}_1}(\mathbf{Y}_\ell; \hat{\mathbf{S}}_\ell, \hat{\theta}_\ell, \hat{\sigma}_{\mathcal{H}_1}^2)}{\text{pdf}_{\mathcal{H}_0}(\mathbf{Y}_\ell; \hat{\sigma}_{\mathcal{H}_0}^2)} \underset{\mathcal{H}_0}{\overset{\mathcal{H}_1}{\gtrless}} \lambda \quad (2.18)$$

where λ is a suitable threshold, $(\hat{\mathbf{S}}_\ell, \hat{\theta}_\ell)$ is the ML estimate of $(\mathbf{S}_\ell, \theta_\ell)$ and $\hat{\sigma}_{\mathcal{H}_i}^2$ is the ML estimate of σ^2 conditioned on \mathcal{H}_i for $i = 0, 1$.

2.4.1 Code detection and timing estimation

Maximizing $\text{pdf}_{\mathcal{H}_0}(\mathbf{Y}_\ell; \sigma^2)$ in (2.16) with respect to σ^2 produces

$$\hat{\sigma}_{\mathcal{H}_0}^2 = \frac{\|\mathbf{Y}_\ell\|^2}{MVR} \quad (2.19)$$

from which it follows that

$$\text{pdf}_{\mathcal{H}_0}(\mathbf{Y}_\ell; \hat{\sigma}_{\mathcal{H}_0}^2) = \left(\frac{MVR}{\pi e \|\mathbf{Y}_\ell\|^2} \right)^{MVR}. \quad (2.20)$$

We now look for the maximum of $\text{pdf}_{\mathcal{H}_1}(\mathbf{Y}_\ell; \mathbf{S}_\ell, \theta_\ell, \sigma^2)$ in (2.17) with respect to θ_ℓ , while keeping σ^2 and \mathbf{S}_ℓ fixed. This yields

$$\hat{\theta}_\ell = \arg \max_{0 \leq \tilde{\theta} \leq \theta_{\max}} \Lambda_\ell(\tilde{\theta}) \quad (2.21)$$

where θ_{\max} is the maximum round trip delay while $\Lambda_\ell(\tilde{\theta})$ takes the form

$$\Lambda_\ell(\tilde{\theta}) = \frac{1}{MVR} \sum_{r=0}^{R-1} \sum_{m=0}^{M-1} \left| \mathbf{a}^H(\tilde{\theta}) \mathbf{Y}_\ell^{(r)}(m) \right|^2. \quad (2.22)$$

Maximizing $\text{pdf}_{\mathcal{H}_1}(\mathbf{Y}_\ell; \mathbf{S}_\ell, \hat{\theta}_\ell, \sigma^2)$ with respect to \mathbf{S}_ℓ leads to

$$\hat{S}_\ell^{(r)}(m) = \frac{1}{V} \mathbf{a}^H(\hat{\theta}_\ell) \mathbf{Y}_\ell^{(r)}(m) \quad (2.23)$$

with $m = 0, 1, \dots, M-1$. Substituting this result back into $\text{pdf}_{\mathcal{H}_1}(\mathbf{Y}_\ell; \mathbf{S}_\ell, \hat{\theta}_\ell, \sigma^2)$ and maximizing with respect to σ^2 produces

$$\hat{\sigma}_{\mathcal{H}_1}^2 = \frac{1}{MVR} \left[\|\mathbf{Y}_\ell\|^2 - MR\Lambda_\ell(\hat{\theta}_\ell) \right] \quad (2.24)$$

from which we get

$$\text{pdf}_{\mathcal{H}_1}(\mathbf{Y}_\ell; \hat{\mathbf{S}}_\ell, \hat{\theta}_\ell, \hat{\sigma}_{\mathcal{H}_1}^2) = \left[\frac{MVR}{\pi e \left(\|\mathbf{Y}_\ell\|^2 - MR\Lambda_\ell(\hat{\theta}_\ell) \right)} \right]^{MVR}. \quad (2.25)$$

From the above results, the GLRT is eventually found to be

$$\left[\frac{\|\mathbf{Y}_\ell\|^2}{\|\mathbf{Y}_\ell\|^2 - MR\Lambda_\ell(\hat{\theta}_\ell)} \right]^{MVR} \underset{\mathcal{H}_0}{\overset{\mathcal{H}_1}{\gtrless}} \lambda \quad (2.26)$$

or, equivalently,

$$\frac{\Lambda_\ell(\hat{\theta}_\ell)}{\|\mathbf{Y}_\ell\|^2} \underset{\mathcal{H}_0}{\overset{\mathcal{H}_1}{\gtrless}} \eta \quad (2.27)$$

with $\eta = [1 - \lambda^{-1/(MVR)}]/(MR)$.

2.4.2 Power estimation

Using the invariance property of the ML estimator, from (2.10) it follows that the estimate of the power p_ℓ can be obtained as

$$\hat{p}_\ell = \frac{1}{MR} \sum_{r=0}^{R-1} \sum_{m=0}^{M-1} \left| \hat{S}_\ell^{(r)}(m) \right|^2 \quad (2.28)$$

or, equivalently,

$$\hat{p}_\ell = \frac{\Lambda_\ell(\hat{\theta}_\ell)}{V} \quad (2.29)$$

having used (2.22) and (2.23). It is worth noting that, if the timing offset is perfectly estimated (i.e., $\hat{\theta}_\ell = \theta_\ell$), then we have

$$\mathbb{E} \{ \hat{p}_\ell \} = p_\ell + \frac{\sigma^2}{MVR} \quad (2.30)$$

and

$$\mathbb{E} \{ \hat{\sigma}_{\mathcal{H}_1}^2 \} = \frac{MR(V-1)}{MVR} \sigma^2 \quad (2.31)$$

from which it follows that \hat{p}_ℓ and $\hat{\sigma}_{\mathcal{H}_1}^2$ are biased estimates of p_ℓ and σ^2 , respectively. From the above results, an unbiased estimate of p_ℓ is found to be

$$\hat{p}_\ell^{(f)} = \hat{p}_\ell - \frac{\hat{\sigma}_{\mathcal{H}_1}^2}{MR(V-1)} \quad (2.32)$$

which can also be rewritten as

$$\hat{p}_\ell^{(f)} = \frac{1}{V-1} \left[\Lambda_\ell(\hat{\theta}_\ell) - \frac{\|\mathbf{Y}_\ell\|^2}{MVR} \right]. \quad (2.33)$$

Using standard computations, it turns out that the variance of \hat{p}_ℓ for $\hat{\theta}_\ell = \theta_\ell$ is given by

$$\text{var}\{\hat{p}_\ell\} = \frac{2p_\ell}{MVR} \sigma^2 + \frac{\sigma^4}{MVR(V-1)}. \quad (2.34)$$

Numerical results shown later indicate that different values of (M, V) should be used to optimize the accuracy of the power and timing estimators. This results into a modified scheme in which M and V are respectively replaced by M_θ and $V_\theta = \lfloor N_{ZC}/M_\theta \rfloor$ for the evaluation of the timing metric $\Lambda_\ell(\tilde{\theta})$ for $\tilde{\theta} = 0, 1, \dots, \theta_{\max}$. After obtaining the timing estimate $\hat{\theta}_\ell$, $\Lambda_\ell(\hat{\theta}_\ell)$ is recomputed from (2.22) after replacing M and V by M_P and $V_P = \lfloor N_{ZC}/M_P \rfloor$, respectively. Finally, $\Lambda_\ell(\hat{\theta}_\ell)$ is used in (2.33) to get the power estimate.

In the sequel, we refer to the above procedure as the GLRT-based RA scheme (GLRT-RA).

2.4.3 Implementation and complexity analysis

The computational load of GLRT-RA is mainly involved in the evaluation of the timing metric $\Lambda_\ell(\tilde{\theta})$ for any possible code in the set \mathcal{C} and for $\tilde{\theta} = 0, 1, \dots, \theta_{\max}$. In the ensuing discussion, we show how the quantities $\Lambda_\ell(\tilde{\theta})$ can be computed by exploiting the specific properties of the ZC sequences. We begin by expanding the right-hand side (RHS) of (2.22) so as to obtain

$$\Lambda_\ell(\tilde{\theta}) = \frac{1}{MVR} \sum_{r=0}^{R-1} \sum_{m=0}^{M-1} \Lambda_\ell^{(r)}(m, \tilde{\theta}) \quad (2.35)$$

where we have used (2.12) and (2.14) and we have defined

$$\Lambda_\ell^{(r)}(m, \tilde{\theta}) = \left| \sum_{v=0}^{V-1} e^{j2\pi v \tilde{\theta}/N} x_\ell^*(mV + v) Z^{(r)}(i_m + v) \right|^2. \quad (2.36)$$

Collecting (2.1) and (2.2), we get

$$x_k(n) = \xi(n) e^{-j2\pi u n C_k / N_{ZC}} e^{-j\phi_k} \quad (2.37)$$

from which it follows that the quantities $\{x_k(n)\}$ are obtained by superimposing a phase shift on the root sequence $\{\xi(n)\}$. Substituting (2.37) into (2.36) yields

$$\Lambda_\ell^{(r)}(m, \tilde{\theta}) = \left| \sum_{v=0}^{V-1} e^{j \frac{2\pi}{N} v (u C_\ell \frac{N}{N_{ZC}} + \tilde{\theta})} Z_\xi^{(r)}(mV + v) \right|^2 \quad (2.38)$$

where

$$Z_\xi^{(r)}(mV + v) = \xi^*(mV + v) Z^{(r)}(i_m + v). \quad (2.39)$$

Denoting by

$$a^{(r)}(m, l) = \sum_{n=0}^{N-1} A^{(r)}(m, n) e^{j2\pi n l / N} \quad (2.40)$$

the N -point IDFT of the sequence

$$A^{(r)}(m, n) = \begin{cases} Z_\xi^{(r)}(mV + n) & 0 \leq n \leq V-1 \\ 0 & V \leq n \leq N-1 \end{cases} \quad (2.41)$$

we may rewrite the RHS of (2.38) as follows

$$\Lambda_\ell^{(r)}(m, \tilde{\theta}) = \left| a^{(r)}(m, \left\lfloor u C_\ell N / N_{ZC} + \tilde{\theta} \right\rfloor) \right|^2. \quad (2.42)$$

From the above equation it is seen that, for any $\ell \in \mathcal{C}$ and $\tilde{\theta} = 0, 1, \dots, \theta_{\max}$, the quantities $\Lambda_\ell^{(r)}(m, \tilde{\theta})$ are obtained from a single N -point IDFT operation applied to the sequence $\{A^{(r)}(m, n)\}$, thereby leading to the scheme depicted in Fig. 2.1. It is worth observing that the IDFT operation in Fig. 2.1 requires approximately $5\eta N \log_2 N$ floating-point operations (flops), with

$$\eta = 1 - \frac{\log_2(N/V) + 2(V/N - 1)}{\log_2 N} \quad (2.43)$$

accounting for the computational saving achievable by skipping the operations on the zero entries of $\{A^{(r)}(m, n)\}$ [23]. Since the IDFT operation must be performed

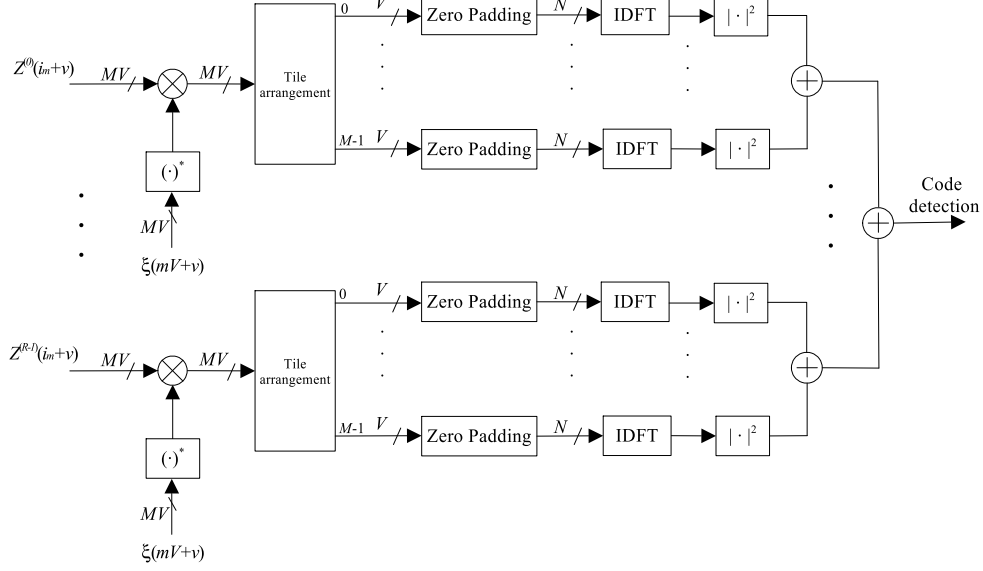


Figure 2.1: Block diagram of the receiver for a RA scheme based on GLRT.

for any value of r and m , the total amount of flops required to evaluate the timing metrics $\Lambda_\ell(\tilde{\theta})$ in (2.42) is $5MR\eta N \log_2 N$. Recalling that different values of M and V are required for power and timing estimation, it follows that the overall number of flops needed by GLRT-RA is eventually given by $5(M_\theta\eta_\theta + M_P\eta_P)RN \log_2 N$ where η_θ and η_P are obtained from (2.43) after replacing V with V_θ and V_P , respectively. It is worth noting that a single IDFT operation is required when $M_\theta = M_P = 1$ and in such a case the scheme depicted in Fig. 2.1 reduces to the one illustrated in [17]. This means that GLRT-RA is equivalent to [17] under the assumption of a flat fading channel. Since in practical applications the received signal is typically affected by multipath distortions, the GLRT-RA is expected to provide some potential benefits with respect to [17]. As we shall see, such an advantage is achieved at the price of a higher complexity since the required IDFT operations involved by GLRT-RA increases with the tile number.

2.5 Numerical results

2.5.1 System parameters

The system parameters are chosen in compliance with the LTE standard [9]. The signal bandwidth is $B = 7.68$ MHz, so that the DFT size is $N = B/\Delta f_{RA} = 6144$ and the sampling interval T is 130 ns. The cyclic prefix and guard time have duration of 0.1 ms, which corresponds to $N_{CP} = N_{GT} = 768$ samples. The carrier frequency is 2.6 GHz and the CFO of each UE is uniformly distributed in the interval $[-0.01, 0.01]$. We use a root-raised cosine function with roll-off $\alpha = 0.22$ and duration $T_g = 6T$ as a modulation pulse. The path gains are modeled as statistically independent and circularly symmetric Gaussian random variables with zero mean and power delay profile as specified in the ITU IMT-2000 Vehic. A channel model [24]. A new channel snapshot is generated at each simulation run. The channel impulse responses of the active UEs have a maximum order of 30 and unit average power. Recalling that we assume a cell radius of 1.5 km, the maximum propagation delay (normalized by the sampling period T) θ_{\max} is equal to 80. The performance of GLRT-RA is first assessed in the presence of a single UE with a fixed timing offset $\theta_1 = 25$, while the case of multiple UEs is considered later.

2.5.2 Performance evaluation

We start evaluating the impact of the number of tiles on the timing estimation accuracy of GLRT-RA. Figure 2.2 illustrates the variance of the timing estimate $\hat{\theta}_1$, defined as $\text{var}(\hat{\theta}_1) = \text{E}\{(\hat{\theta}_1 - \text{E}\{\hat{\theta}_1\})^2\}$, vs. M_θ for different values of SNR and with $K = 1$ and $R = 1$. It is worth observing that, since θ_1 is the timing error normalized by the sampling period T , its estimate $\hat{\theta}_1$ is a dimensionless quantity. As it is seen, the best results are obtained for $4 \leq M_\theta \leq 7$, while a degradation is observed for larger values of M_θ as the SNR decreases. As expected, some advantage is achieved with respect to $M_\theta = 1$, which corresponds to the conventional RA scheme (CRA) illustrated in [17]. Since the number of flops required by GLRT-RA increases with M_θ , in all subsequent simulations M_θ is fixed to 4. Figure 2.3 illustrates $\text{var}(\hat{\theta}_1)$ as a function of the SNR with $K = 1$ and $R = 1$. Although the estimation accuracy of both CRA and GLRT-RA is only marginally affected by the SNR, a remarkable gain is achieved by using GLRT-RA in place of CRA.

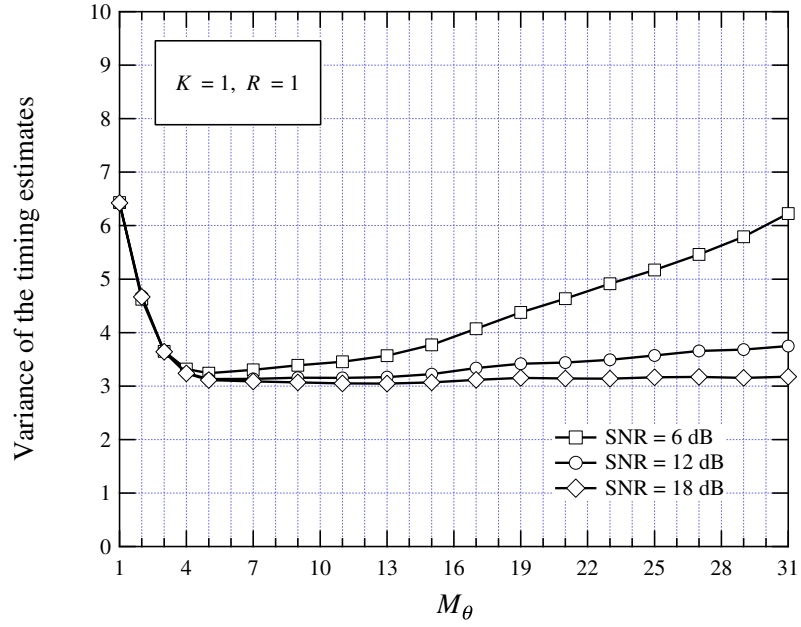


Figure 2.2: $\text{var}(\hat{\theta}_1)$ vs. M_θ for GLRT-RA with $K = 1, R = 1$ and different SNR values.

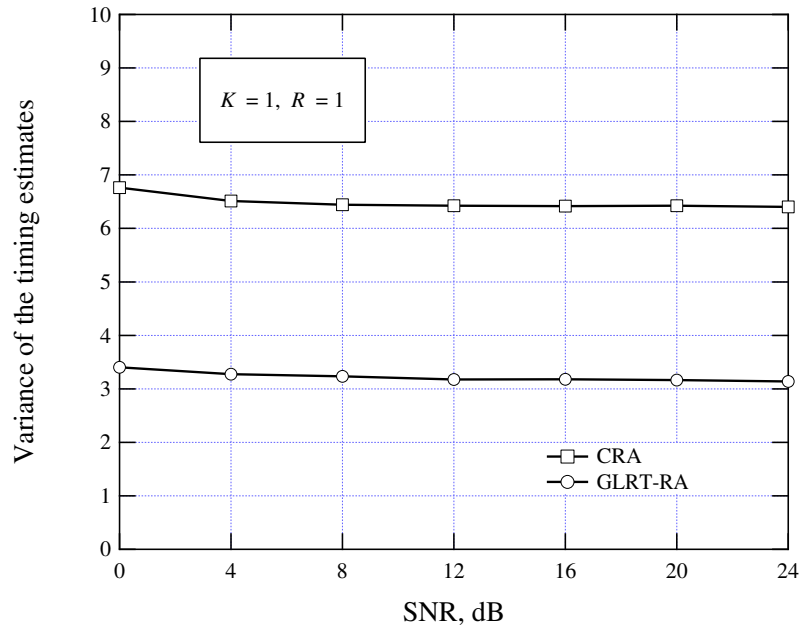


Figure 2.3: $\text{var}(\hat{\theta}_1)$ vs. SNR for the investigated schemes with $K = 1$ and $R = 1$.

We now assess the performance of the power estimator. For this purpose, Fig. 2.4 illustrates the *normalized* variance of the power estimate, say $\text{nvar}(\hat{p}_1^{(f)}) = \text{var}\{\hat{p}_1^{(f)}\} / [\text{E}\{p_1\}]^2$, as a function of M_P for different SNR values and with $K = 1$ and $R = 1$. The theoretical results given in (2.34) are also shown for comparison. As is seen, the agreement between numerical results and theoretical analysis is achieved only when M_P is adequately large. In order to achieve a good trade-off between accuracy and system complexity, the value of M_P is chosen equal to 25.

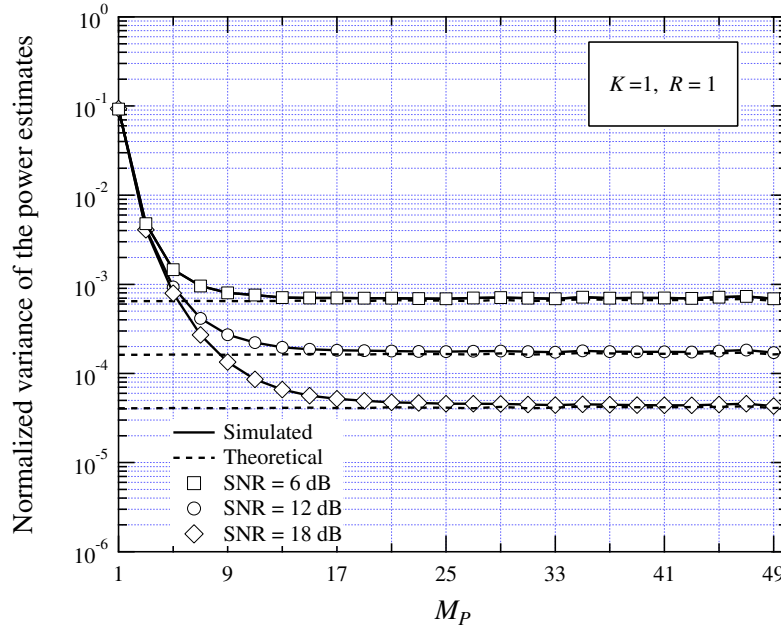


Figure 2.4: $\text{nvar}(\hat{p}_1^{(f)})$ vs. M_P for GLRT-RA with $K = 1$, $R = 1$ and different SNR values.

In Fig. 2.5 we show $\text{nvar}(\hat{p}_1^{(f)})$ as a function of the SNR with $K = 1$ and $R = 1$. As before, comparisons are made with the CRA scheme, which corresponds to setting $M_P = 1$. We see that GLRT-RA attains the theoretical results at all SNR values, while the accuracy of CRA is virtually independent of the SNR and exhibits a significant loss compared to GLRT-RA. The code detection capability of the investigated schemes is assessed in terms of mis-detection probability P_{md} and false alarm probability P_{fa} . For this purpose, the SNR is set to 12 dB and we let $K = R = 1$. Numerical results averaged over 50,000 channel realizations have shown that for threshold values centered around $\eta = 0.1$ both GLRT-RA and CRA provide

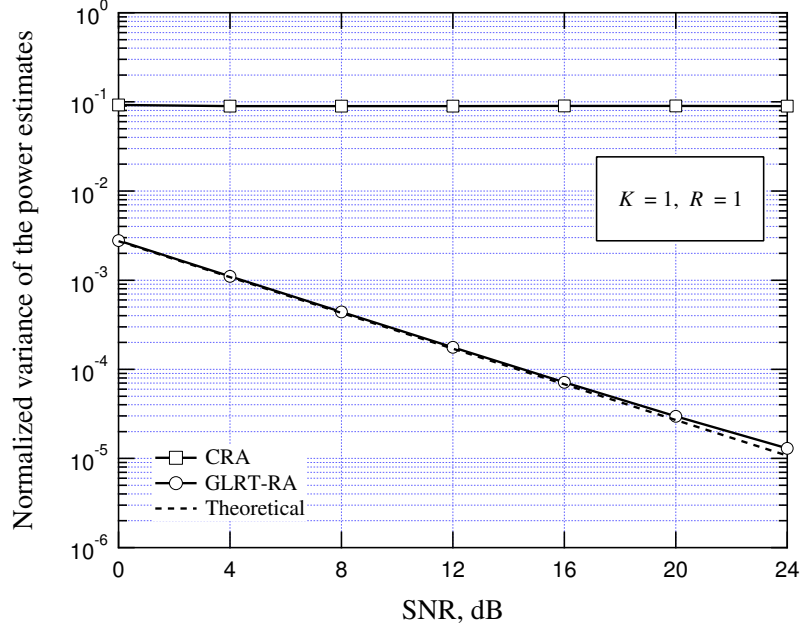


Figure 2.5: $\text{nvar}(\hat{p}_1^{(f)})$ vs. the SNR for the investigated schemes with $K = 1$ and $R = 1$.

a P_{fa} smaller than $2 \cdot 10^{-5}$. On the other hand, GLRT-RA achieves a P_{md} in the order of $7 \cdot 10^{-4}$, while CRA provides $P_{md} = 4 \cdot 10^{-3}$. This means that GLRT-RA exhibits improved code detection capability with respect to CRA. The performance of GLRT-RA when multiple antennas are employed at the eNodeB is now investigated. Figures 2.6 and 2.7 illustrate $\text{var}(\hat{\theta}_1)$ and $\text{nvar}(\hat{p}_1^{(f)})$ as a function of the SNR with $K = 1$ and $R = 1, 2$ or 4 . As expected, increasing R improves the timing and power estimation accuracy of GLRT-RA. In particular, for SNR values smaller than 16 dB an array gain equal to $10 \log R$ dB is achieved in terms of $\text{nvar}(\hat{p}_1^{(f)})$ with respect to a single-antenna scenario. The performance of GLRT-RA in the presence of K UEs is reported in Figs. 2.8 and 2.9 for $R = 1$ or 4 . Here, the timing offset of the k th UE (with $k = 1, \dots, K$) is chosen equal to $\theta_k = 25 + 5(k - 1)$, while the average signal power of all active UEs is set to unity. Without loss of generality, the system performance is measured on the basis of the signal received from the first UE. Inspection of Fig. 2.8 reveals that the accuracy of the timing estimates is virtually independent of the number of UEs, while the results in Fig. 2.9 indicate that the accuracy of the power estimator deteriorates as K increases. Moreover, from Fig. 2.9 it follows that using more than one antenna has no practical benefit when $K \geq 2$.

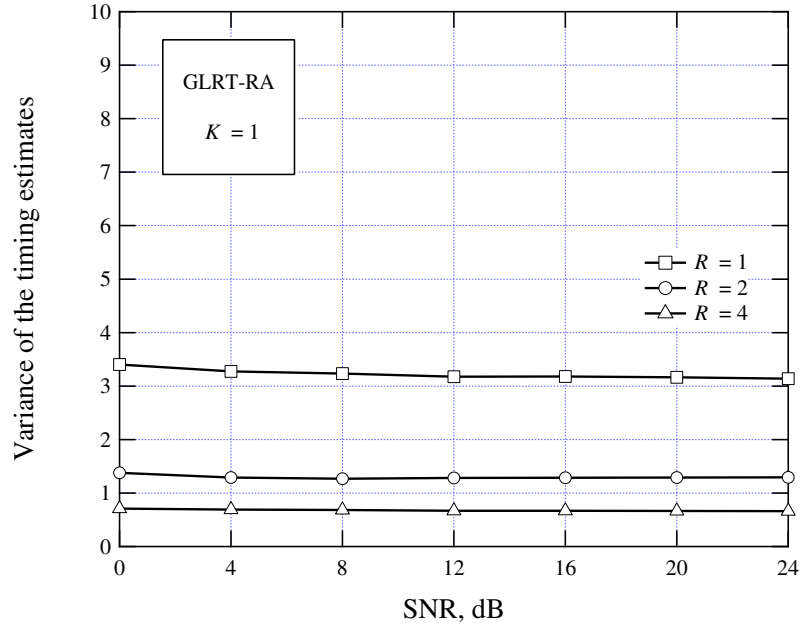


Figure 2.6: $\text{var}(\hat{\theta}_1)$ vs. the SNR for GLRT-RA with $K = 1$ and $R = 1, 2$ or 4 .

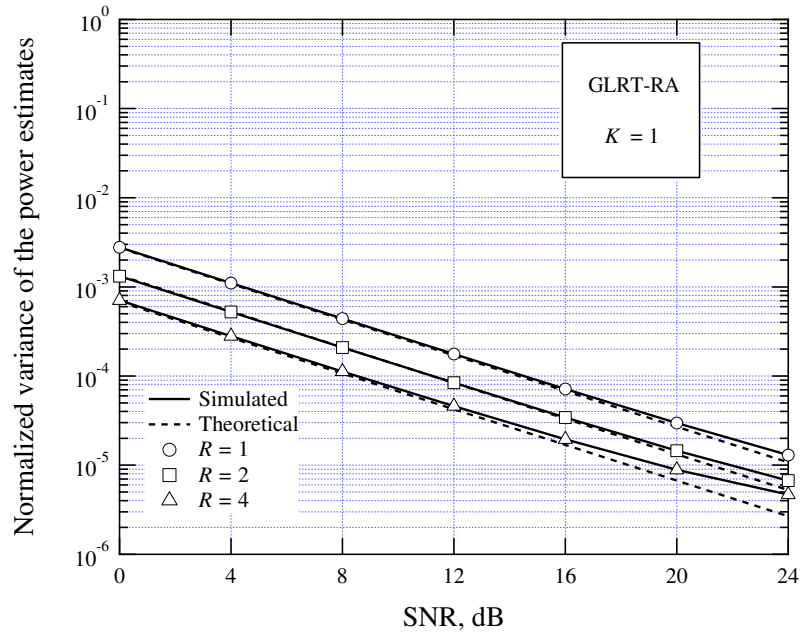


Figure 2.7: $\text{nvar}(\hat{p}_1^{(f)})$ vs. the SNR for GLRT-RA with $K = 1$ and $R = 1, 2$ or 4 .

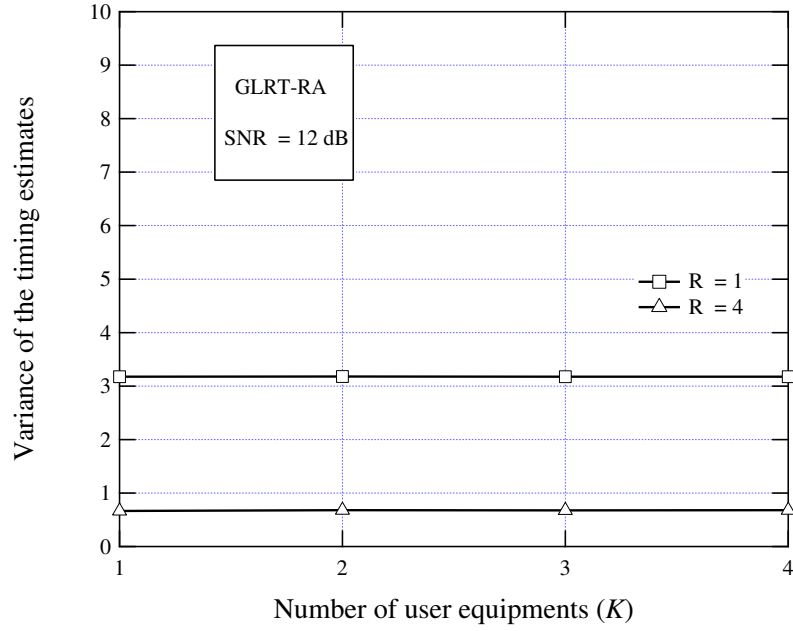


Figure 2.8: $\text{var}(\hat{\theta}_1)$ vs. K for GLRT-RA when SNR= 12 dB and $R = 1$ or 4.

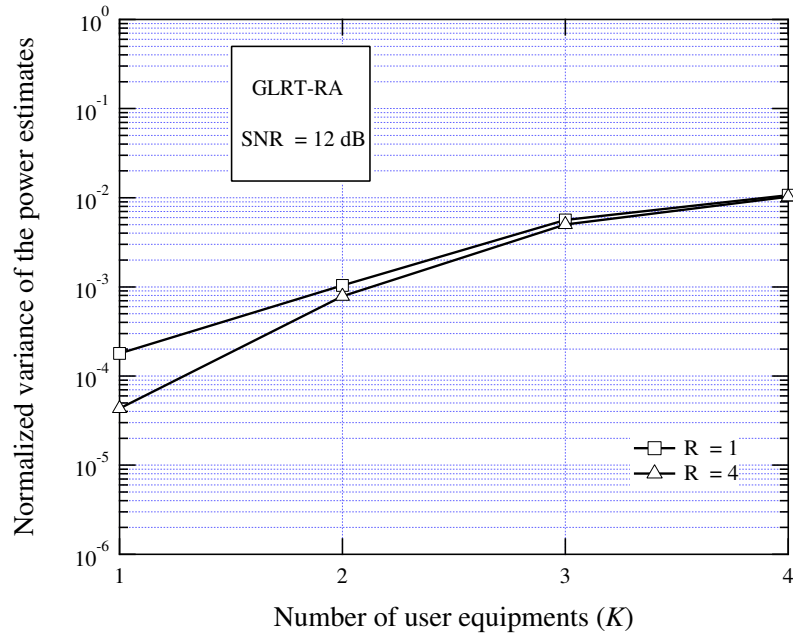


Figure 2.9: $\text{nvar}(\hat{p}_1^{(f)})$ vs. K of GLRT-RA when SNR= 12 dB and $R = 1$ or 4.

2.5.3 Computational complexity

It is interesting to compare the investigated schemes in terms of their computational requirement. In doing so it is worth pointing out that, even though $N = 6144$ is not a power of two, the number of flops involved in the IDFT operation in Fig. 2.1 is still well approximated by $5\eta N \log_2 N$ just because the IDFT size can be decomposed into the product of an integer number and a power of two as $N = 3 \cdot 2^{11}$. Hence, setting $M_\theta = 4$, $V_\theta = 209$, $M_P = 25$, $V_P = 33$ and $R = 1$, the complexity of GLRT-RA is approximately 18.7 times higher than that involved by CRA. This means that the improved performance of GLRT-RA is achieved at the price of an increased computational load. However, the results shown in Fig. 2.4 indicate that, at practical SNR values around 10 dB, parameter M_P can be reduced from 25 to 11 with only a marginal loss of the estimation accuracy. The same value can be used for M_θ without incurring any significant degradation in the timing estimation accuracy for $\text{SNR} \geq 12$ dB. In these circumstances, one single IDFT operation can be used, thereby reducing the complexity of GLRT-RA by a factor 2.4. These arguments allow the system designer to achieve the desired trade-off between computational requirement and system performance.

2.6 Concluding remarks

In this chapter we presented a novel RA method which is specifically devised for low-mobility LTE-3GPP systems characterized by negligible Doppler shifts. The proposed scheme relies on the GLRT criterion to decide whether a given code is present or not in the PRACH and inherently takes into account the multipath distortions introduced by the propagation channel. After modeling the MAI as white Gaussian noise, the ML principle is employed to estimate the timing error and power level of the detected codes. Computer simulations indicate that the resulting scheme (GLRT-RA) outperforms the conventional RA method derived under the simplifying assumption of a flat-fading channel. The price for such a performance gain is a certain increase of the computational complexity. However, a judicious design of the algorithm parameters allows one to reduce the processing load without incurring any significant performance degradation.

Chapter 3

Frequency Estimation and Preamble Identification in OFDMA Systems

3.1 Introduction

Orthogonal frequency-division multiple-access (OFDMA) is a popular technology for multiuser high-speed wireless transmissions. Due to its recognized advantages in terms of spectral efficiency, dynamic channel allocation and resilience to multipath distortions, OFDMA has been selected by the WiMAX alliance as one of the physical layer modulation technique for fixed and nomadic broadband access in a wireless metropolitan area network (WMAN) [11].

WiMAX systems compliant with the IEEE 802.16e specifications support multi-cell communications and operate in a time division duplexing (TDD) mode, with each TDD frame being fragmented into a downlink (DL) subframe and an uplink (UL) subframe. Each cell is divided into three sectors known as *segments*, and is identified by an integer number called *cell ID*. Upon entering the network or during an handover operation, the mobile terminal (MT) has to recover both the segment number and cell ID in order to establish a radio link with the serving base station (BS). This operation is known as *cell search* and is accomplished by exploiting a suitably designed training

preamble placed at the start of the DL subframe. Such a preamble conveys one out of 114 possible pseudo-noise (PN) pilot sequences which univocally identifies the segment number and cell ID. In addition to cell search, the preamble is also used for other fundamental tasks, including frame detection as well as initial time and frequency synchronization.

Most pilot-based synchronization algorithms for multicarrier transmissions exploit the repetitive structure of a training preamble [25]–[27]. For example, in the IEEE 802.11a/g wireless local area network (WLAN) [28] the preamble consists of ten identical short symbols for timing acquisition and fractional frequency offset (FFO) estimation, followed by two identical long symbols which are used to recover the integral frequency offset (IFO) [29]. Unfortunately, the same approach cannot be adopted in a WiMAX cellular network for a couple of reasons [30]. First, the preamble specified in the IEEE 802.16e standard is modulated on every third subcarrier, which results into a non-perfectly periodic structure in the time domain. Second, the MT has only partial knowledge of the received preamble waveform as it ignores which pilot sequence has been selected by the BS out of all 114 possible candidates. These facts significantly complicate the cell search problem and the synchronization task in a WiMAX system.

Although in principle it is possible to consider the joint estimation of the timing error, the FFO, the IFO and the preamble index, the resulting complexity would make such a method unsuitable for practical implementation. A more pragmatic approach relies on the following two-stage procedure. Firstly, timing acquisition and FFO recovery are accomplished in a blind fashion without exploiting any information about the received preamble sequence. In the second stage, after timing alignment and FFO compensation, the IFO and preamble index are jointly detected. These problems have recently attracted much attention in the open literature and several solutions are currently available. Specifically, in [30] a new timing metric for frame synchronization is proposed by exploiting the conjugate symmetry property of the IEEE 802.16e training preamble. In a multipath scenario, however, the metric exhibits several secondary peaks which may result into a false detection of the frame boundary. The FFO is estimated in [31]–[33] by measuring the phase shift between the last part of an OFDM block and its cyclic prefix (CP) extension. This method was originally presented in [34] and does not require the transmission of any specific pilot sequence. Its main drawback is that in the presence of multipath dispersion the CP is affected by

interblock interference (IBI), which may seriously degrade the estimation accuracy. A similar problem occurs in [35], where the authors suggest a modification of the Schmidl and Cox algorithm [25] which provides accurate results only in the absence of any channel distortion. A universal FFO estimator for OFDM systems employing training preambles composed by non-identical segments is illustrated in [36]. This scheme can be applied to WiMAX systems [37] and provides accurate estimates with affordable complexity. Regarding the joint detection of the IFO and preamble index, the conventional approach operates in the frequency domain and shifts the discrete Fourier transform (DFT) of the received signal by the hypothesized IFO values. The shifted sequence is next correlated with all possible pilot sequences, and the unknown parameters are eventually retrieved through non-coherent differential detection methods [38]- [41]. The resulting scheme is computationally heavy as it requires an exhaustive search over all candidate IFO and preamble index pairs. As shown in [40], however, the number of candidates is reduced by a factor of three if an energy detection method is firstly applied to find the location of the modulated subcarriers. Further simplifications are suggested in [41], where early dropping of bad candidates is proposed by resorting to the principle of dynamic metric thresholding. In [42], the authors present the joint maximum likelihood (ML) estimator of the channel impulse response (CIR) and preamble index under the simplifying assumption that the IFO has been previously recovered in some way.

With the only exception of [42], all the aforementioned methods have been derived by following heuristic reasoning. In order to check whether their performance can be substantially improved or not, it is of interest to make comparisons with alternative approaches based on some optimality criterion. With this goal in mind, in the present chapter we employ ML methods to study the problem of carrier frequency offset (CFO) estimation and preamble index identification in the presence of a training preamble composed by some correlated but non-identical parts (as specified by the IEEE 802.16e standard). In doing so, we assume that timing information has been previously acquired and is available with some residual error. In particular, after modeling the channel-distorted pilot symbols as nuisance parameters, we address the CFO estimation problem and derive the relevant Cramer-Rao bound (CRB). It turns out that, in principle, the CFO estimator is able to retrieve the entire frequency error without the need for splitting it into fractional and integer parts. In practice, however, such a decomposition is recommended to avoid large errors that might

otherwise occur. We also show that the heuristic algorithm proposed in [36] has virtually the same accuracy of the ML frequency estimator, but provides ambiguous estimates. In order to remove such an ambiguity, we combine this method with the ML estimator and obtain a scheme that approaches the CRB in all practical scenarios while requiring affordable complexity. We next investigate the joint estimation of the IFO and preamble index, and suggest some approximations to the exact ML solution in order to trade system performance against computational burden.

In summary, this chapter provides a threefold contribution. First, we present a novel expression of the CRB for CFO recovery which, in contrast to other bounds available in the literature, can be applied to the WiMAX preamble. Second, we show that combining the FFO recovery scheme illustrated in [36] with the ML estimator leads to an accurate and low-complexity algorithm which turns out to be a promising candidate for WiMAX applications. Third, we derive a novel ML-based approach for joint IFO and preamble index recovery which outperforms existing methods in terms of increased accuracy and improved resilience against residual timing errors.

3.2 System model

We consider the downlink of a TDD multi-cell OFDMA system having N available subcarriers with indices in the interval $[-N/2, N/2 - 1]$ and frequency spacing Δf . In order to facilitate the synchronization and cell search tasks, each DL subframe begins with a training preamble modulated by a pilot sequence of length $N_p < N$. This sequence is chosen from a set of candidates $\{\mathbf{p}_u = [p_u(0), p_u(1), \dots, p_u(N_p - 1)]^T; u = 0, 1, \dots, N_U - 1\}$, where N_U is the number of possible sequences, $p_u(n) = \pm A$ are pseudo-noise (PN) binary symbols and u is the *preamble index* belonging to the set $I_U = \{0, 1, \dots, N_U - 1\}$. The latter univocally determines the *cell segment* m_u and the *cell ID* ℓ_u through a mapping rule $u \rightarrow (m_u, \ell_u)$ reported in [11]. In general, the receiver has full knowledge of the sequences \mathbf{p}_u , but ignores which of them has been selected for transmission. During the training preamble, the pilot symbols are placed at the subcarrier indices

$$i_{n,u} = N_1 + m_u + n\delta \quad 0 \leq n \leq N_p - 1 \quad (3.1)$$

where δ is the interval between two used subcarriers and $N_1 + m_u$ is the index of the first used subcarrier. It is worth observing that the cell segment m_u belongs to the

interval $\{0, 1, \dots, \delta - 1\}$ and defines δ distinct sets of pilot positions. The illustrated pilot pattern is general enough to include the WiMAX preamble defined in the IEEE 802.16e standard, where $A = 2\sqrt{2}$, $N_1 = -426$ and $\delta = 3$.

The transmitted waveform propagates through a multipath channel with discrete-time impulse response $\{h(\ell); 0 \leq \ell \leq L - 1\}$ of order L . At the MT receiver, the incoming signal is down-converted to baseband and sampled with period T_s . We assume that a coarse timing estimate is available such that the set of N time-domain samples $\mathbf{x} = [x(0), x(1), \dots, x(N - 1)]^T$ belonging to the training preamble can be identified without incurring any IBI. Then, assuming that the u th pilot sequence has been selected by the BS, we have

$$x(k) = e^{j2\pi f_d k/N} s_u(k - \tau_d) + w_I(k) + w_n(k) \quad 0 \leq k \leq N - 1 \quad (3.2)$$

where f_d is the CFO (normalized to Δf), τ_d denotes the residual timing error (normalized to T_s), $w_I(k)$ accounts for possible inter-cell interference (ICI) and $w_n(k)$ is the noise term, which is Gaussian distributed with zero mean and power σ_n^2 . Finally, $s_u(k)$ is the sample taken at $t = kT_s$ of the useful signal waveform

$$s_u(t) = \frac{1}{\sqrt{N}} \sum_{n=0}^{N_p-1} p_u(n) H(i_{n,u}) e^{j2\pi i_{n,u} t/T} \quad (3.3)$$

where $T = NT_s$ and

$$H(n) = \sum_{\ell=0}^{L-1} h(\ell) e^{-j2\pi n\ell/N} \quad (3.4)$$

is the channel frequency response over the n th subcarrier. The quantities $\{w_I(k); k = 0, 1, \dots, N - 1\}$ in (3.2) are the superposition of OFDMA signals from neighbouring cells and can reasonably be approximated as zero-mean Gaussian random variables with power σ_I^2 and negligible cross-correlation [43]. Accordingly, in the sequel we replace the sum $w_I(k) + w_n(k)$ by a single term $w(k)$, which is modeled as a circularly-symmetric white Gaussian process with zero mean and power $\sigma_w^2 = \sigma_I^2 + \sigma_n^2$. From (3.3) we see that the average power of $s_u(k)$ is $\sigma_s^2 = \sigma_H^2 A^2 N_p / N$, with $\sigma_H^2 = \mathbb{E}\{|H(n)|^2\}$ being the average channel power. The signal-to-noise-plus-interference ratio (SINR) [44] is thus given by

$$\text{SINR} = \frac{\sigma_s^2}{\sigma_w^2} = \frac{\sigma_H^2 A^2 N_p}{N \sigma_w^2}. \quad (3.5)$$

It is worth noting that, although $s_u(t)$ is periodic with period T/δ , the repetition structure is not preserved in the sampled sequence $s_u(k)$ if N is not an integer multiple of δ .

After defining the quantities

$$\xi_u(n) = p_u(n)H(i_{n,u})e^{-j2\pi i_{n,u}\tau_d/N} \quad 0 \leq n \leq N_p - 1 \quad (3.6)$$

we may rewrite $x(k)$ as

$$x(k) = e^{j2\pi\nu k/N} \frac{1}{\sqrt{N}} \sum_{n=0}^{N_p-1} \xi_u(n) e^{j2\pi k(N_1+n\delta)/N} + w(k) \quad (3.7)$$

where $\nu = f_d + m_u$ can be interpreted as an *equivalent* frequency error comprising both the true CFO value f_d and the frequency shift m_u , which is artificially superimposed on the transmitted training preamble to specify the cell segment. Letting $\boldsymbol{\xi}_u = [\xi_u(0), \xi_u(1), \dots, \xi_u(N_p - 1)]^T$ and $\mathbf{w} = [w(0), w(1), \dots, w(N - 1)]^T$, we may put (3.7) into the equivalent form

$$\mathbf{x} = \mathbf{\Gamma}(\nu)\mathbf{F}\boldsymbol{\xi}_u + \mathbf{w} \quad (3.8)$$

where \mathbf{F} is an $N \times N_p$ matrix with entries

$$[\mathbf{F}]_{k,n} = \frac{1}{\sqrt{N}} e^{j2\pi k(N_1+n\delta)/N} \quad 0 \leq k \leq N - 1, \quad 0 \leq n \leq N_p - 1 \quad (3.9)$$

and $\mathbf{\Gamma}(\nu) = \text{diag}\{e^{j2\pi n\nu/N}; n = 0, 1, \dots, N-1\}$. To proceed further, we define the diagonal matrices $\mathbf{P}_u = \text{diag}\{p_u(n); n = 0, 1, \dots, N_p-1\}$ and $\mathbf{D}(\tau_d) = \text{diag}\{e^{-j2\pi\tau_d n\delta/N}; n = 0, 1, \dots, N_p - 1\}$. Then, from (3.6) it follows that

$$\boldsymbol{\xi}_u = \mathbf{P}_u \mathbf{D}(\tau_d) \mathbf{G} \mathbf{c} \quad (3.10)$$

where \mathbf{G} has entries

$$[\mathbf{G}]_{n,\ell} = e^{-j2\pi\ell n\delta/N} \quad 0 \leq n \leq N_p - 1, \quad 0 \leq \ell \leq L - 1 \quad (3.11)$$

and $\mathbf{c} = [c(0), c(1), \dots, c(L - 1)]^T$ is an L -dimensional vector which collects the *modified* CIR

$$c(\ell) = h(\ell) e^{-j2\pi(\ell+\tau_d)(m_u+N_1)/N} \quad 0 \leq \ell \leq L - 1. \quad (3.12)$$

Our goal is the estimation of the frequency error ν and preamble index u based on the received vector \mathbf{x} . Inspection of (3.8) and (3.10) indicates that this task is complicated by the presence of the nuisance parameters τ_d and \mathbf{c} . Since the joint ML estimation of all unknown quantities cannot be pursued with affordable complexity, in what follows we adopt a suboptimal approach wherein ν and ξ_u are firstly recovered by applying the ML strategy to the signal model (3.8), while (u, τ_d, \mathbf{c}) are subsequently retrieved on the basis of (3.10).

3.3 ML frequency estimation

3.3.1 Derivation of the ML estimator

Given the unknown parameters (ξ_u, ν) , from (3.8) it turns out that \mathbf{x} is Gaussian distributed with mean $\mathbf{\Gamma}(\nu)\mathbf{F}\xi_u$ and covariance matrix $\sigma_w^2\mathbf{I}_N$. Hence, the joint ML estimate of (ξ_u, ν) is found by looking for the global maximum of the log-likelihood function (LLF)

$$\Lambda(\tilde{\xi}_u, \tilde{\nu}) = -N \ln(\pi\sigma_w^2) - \frac{1}{\sigma_w^2} \left\| \mathbf{x} - \mathbf{\Gamma}(\tilde{\nu})\mathbf{F}\tilde{\xi}_u \right\|^2. \quad (3.13)$$

Maximizing with respect to $\tilde{\xi}_u$ produces

$$\hat{\xi}_u(\tilde{\nu}) = (\mathbf{F}^H\mathbf{F})^{-1}\mathbf{F}^H\mathbf{\Gamma}^H(\tilde{\nu})\mathbf{x} \quad (3.14)$$

with $\mathbf{F}^H\mathbf{F} = \mathbf{I}_{N_p}$. The *concentrated* likelihood function of ν is obtained after substituting $\hat{\xi}_u(\tilde{\nu})$ into the right-hand-side of (3.13). Skipping irrelevant factors and additive terms independent of $\tilde{\nu}$, we obtain

$$\Lambda_1(\tilde{\nu}) = \frac{1}{N_p} \left\| \mathbf{F}^H\mathbf{\Gamma}^H(\tilde{\nu})\mathbf{x} \right\|^2 \quad (3.15)$$

from which the ML estimate (MLE) of ν is obtained as

$$\hat{\nu}_{MLE} = \arg \max_{\tilde{\nu}} \{ \Lambda_1(\tilde{\nu}) \}. \quad (3.16)$$

A physical interpretation of the MLE is found by rewriting $\Lambda_1(\tilde{\nu})$ as

$$\Lambda_1(\tilde{\nu}) = \frac{1}{N_p} \sum_{n=0}^{N_p-1} |X(N_1 + n\delta; \tilde{\nu})|^2 \quad (3.17)$$

where

$$X(m; \tilde{\nu}) = \frac{1}{\sqrt{N}} \sum_{k=0}^{N-1} x(k) e^{-j2\pi(m+\tilde{\nu})k/N} \quad (3.18)$$

is the DFT of the received samples $\{x(k)\}$ counter-rotated at an angular speed $2\pi\tilde{\nu}/N$. Hence, from (3.17) it follows that $\hat{\nu}_{MLE}$ is the value of $\tilde{\nu}$ that maximizes the overall energy received onto the subcarriers with indices $\{N_1 + n\delta\}$ for $n = 0, 1, \dots, N_p - 1$.

A special situation occurs when $N = N_p\delta$. In such a case the preamble sequence $s_u(k)$ is periodic of period N/δ and the MLE metric takes the conventional form [45]

$$\Lambda_1(\tilde{\nu}) = C_0 + 2\Re \left\{ \sum_{m=1}^{\delta-1} C_m e^{-j2\pi m\tilde{\nu}/\delta} \right\} \quad (3.19)$$

where C_m is the auto-correlation of \mathbf{x} with lag mN/δ , i.e.,

$$C_m = \frac{1}{N} \sum_{k=mN/\delta}^{N-1} x(k)x^*(k - mN/\delta). \quad (3.20)$$

Interestingly, when $\delta = 2$ the global maximum of (3.19) is located at $\hat{\nu}_{MLE} = \arg\{C_1\}$, which coincides with the FFO estimator proposed in [25].

3.3.2 Accuracy and estimation range of MLE

By invoking the asymptotic efficiency property of the MLE [4], we expect that $\hat{\nu}_{MLE}$ is unbiased and attains the asymptotic CRB (ACRB) for large data records. The ACRB is computed in the Appendix and is found to be

$$\text{ACRB}\{\nu\} = \frac{3(\text{SINR})^{-1}}{2\pi^2 N(1 - 1/N^2)[1 - \gamma(N, N_p, \delta)]} \quad (3.21)$$

where the SINR is expressed in (3.5) and $\gamma(N, N_p, \delta)$ is defined as

$$\gamma(N, N_p, \delta) = \frac{6}{N_p(N^2 - 1)} \sum_{m=1}^{N_p-1} \frac{N_p - m}{\sin^2(\pi m\delta/N)}. \quad (3.22)$$

It is worth noting that the bound (3.21) represents a modified version of the CRB expressed in [26] and [45], the difference lying in the presence of the factor $1 - \gamma(N, N_p, \delta)$ in the denominator. Since this factor is less than one, the novel ACRB in (3.21) turns out to be tighter than the CRB available in the literature.

The estimation range of the MLE can be inferred from the expected value of the CFO metric $\Lambda_1(\tilde{\nu})$. Skipping the details, it is found that

$$\mathbb{E}\{\Lambda_1(\tilde{\nu})\} = \sigma_H^2 A^2 \sum_{m=-N_p+1}^{N_p-1} \left(1 - \frac{|m|}{N_p}\right) f_N^2(\tilde{\nu} - \nu - m\delta) + \sigma_w^2 \quad (3.23)$$

with

$$f_N(x) = \frac{\sin(\pi x)}{N \sin(\pi x/N)}. \quad (3.24)$$

Figure 3.1 illustrates $\mathbb{E}\{\Lambda_1(\tilde{\nu})\}$ over a wide range of $\tilde{\nu}$ values for SINR = 10 dB. The training preamble is taken from the IEEE 802.16e standard with $N = 1024$, $N_p = 284$ and $\delta = 3$. Without any loss of generality, the average channel power σ_H^2 is normalized to unity and the CFO value is fixed to $\nu = 0$. A zoom is also shown on the top right of the figure to better highlight the shape of the metric over the restricted range $\tilde{\nu} \in [-10, 10]$. We see that the metric exhibits a global maximum placed at the true CFO value $\tilde{\nu} = \nu$, while secondary peaks are present at $\tilde{\nu} = \nu + m\delta$ ($m = \pm 1, \pm 2, \dots$). Furthermore, from (3.23) it follows that $\mathbb{E}\{\Lambda_1(\tilde{\nu})\}$ is

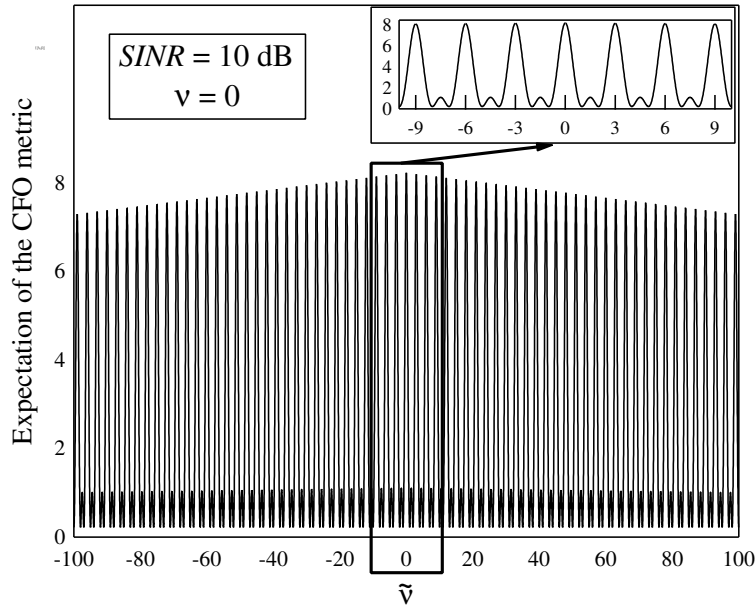


Figure 3.1: Expectation of the CFO metric obtained at SINR = 10 dB using the IEEE 802.16e training preamble.

periodic of period N . Collecting these facts together we conclude that, in principle, the MLE is able to recover the CFO over the full range $[-N/2, N/2)$. However, since the amplitude of the secondary peaks of $E\{\Lambda_1(\tilde{\nu})\}$ decreases slowly with $|m|$, in the presence of ICI and/or noise the global maximum of the frequency metric may occur in the proximity of $\nu + m\delta$ for some $m \neq 0$. In such a case, $\hat{\nu}_{MLE}$ would be ambiguous by multiples of δ , thereby resulting into large errors (*outliers*). This situation is depicted in Fig. 3.2, which reports the estimation error $\nu - \hat{\nu}_{MLE}$ measured over 1000 simulation runs using the IEEE 802.16e preamble. Here, the SINR is set to 10 dB and the maximum of $\Lambda_1(\tilde{\nu})$ is found through a grid-search over the interval $\tilde{\nu} \in [-12, 12]$. We see that several outliers are present, with disabling effects on the receiver performance. One possible approach to avoid the outliers is to decompose ν

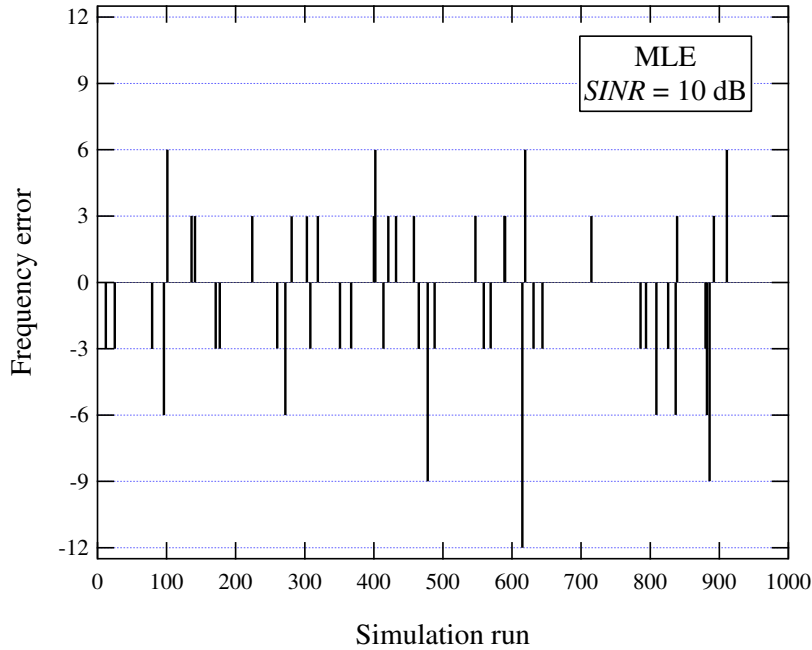


Figure 3.2: Estimation error $\nu - \hat{\nu}_{MLE}$ over 10^3 runs for $SINR = 10$ dB using the IEEE 802.16e preamble.

into a fractional part (FFO) ε , less than $\delta/2$ in magnitude, plus an integer part (IFO) which is a multiple of δ . This amounts to putting

$$\nu = \varepsilon + \eta\delta \quad (3.25)$$

where η is an integer and ε belongs to the interval $[-\delta/2, \delta/2)$. Due to its potential ambiguity by multiples of δ , the MLE can only be used to retrieve the FFO in the form

$$\hat{\varepsilon}_{MLE} = \arg \max_{\varepsilon \in [-\delta/2, \delta/2)} \{\Lambda_1(\tilde{\varepsilon})\} \quad (3.26)$$

while η is subsequently estimated as specified later.

3.3.3 Implementation and complexity analysis of MLE

In practice, the maximization of the MLE metric $\Lambda_1(\tilde{\varepsilon})$ in (3.26) can be accomplished by following a two-step procedure. The first step (*coarse search*) evaluates $\Lambda_1(\tilde{\varepsilon})$ over a set of $\tilde{\varepsilon}$ values, say $\{\tilde{\varepsilon}_i\}$, and determines the location $\tilde{\varepsilon}_M$ of the maximum over this set. In the second step (*fine search*), the samples $\Lambda_1(\tilde{\varepsilon}_i)$ are interpolated and the local maximum nearest $\tilde{\varepsilon}_M$ is found. Without any loss of generality, the quantities $\{\tilde{\varepsilon}_i\}$ are uniformly distributed within the search region $[-\delta/2, \delta/2)$ and take the form

$$\tilde{\varepsilon}_i = -\frac{\delta}{2} + \frac{i}{N_s} \quad i = 0, 1, \dots, N_s\delta - 1 \quad (3.27)$$

where $N_s \in \mathbb{N}$ is a design parameter (*pruning factor*) representing the number of trial FFO values in a frequency band equal to the subcarrier spacing. The coarse search can be efficiently performed by considering the following zero-padded sequence of length $N_{ZP} = N_s N$

$$x_{ZP}(k) = \begin{cases} x(k) & 0 \leq k \leq N - 1 \\ 0 & N \leq k \leq N_{ZP} - 1 \end{cases} \quad (3.28)$$

and computing its fast Fourier transform (FFT) at the frequencies $f_m = m/N_{ZP}$, with $-N_{ZP}/2 \leq m \leq N_{ZP}/2 - 1$. This produces the quantities $X(N_1 + n\delta; \tilde{\varepsilon}_i)$, which are next exploited to evaluate $\Lambda_1(\tilde{\varepsilon}_i)$ in (3.17).

The computational requirement of the MLE can be assessed as follows. The N_{ZP} -point FFT needs $2\zeta N_{ZP} \log_2 N_{ZP}$ real multiplications plus $3\zeta N_{ZP} \log_2 N_{ZP}$ real additions, for a total of $5\zeta N_{ZP} \log_2 N_{ZP}$ floating point operations (flops). Here, the coefficient

$$\zeta = 1 - \frac{\log_2 N_s + 2(1/N_s - 1)}{\log_2 N_{ZP}} \quad (3.29)$$

accounts for the computational saving achievable by skipping the operations on the zeros in the FFT of $x_{ZP}(k)$ [46]. Once the FFT output is available, additional $4N_p N_s \delta$ flops are required to evaluate $\Lambda_1(\tilde{\varepsilon}_i)$ over the set of $N_s \delta$ values $\tilde{\varepsilon}_i$. The overall complexity of MLE is summarized in the first row of Tab. 3.1. In writing this figure we have neglected the operations involved with the fine search, which is comparatively easier than the coarse search.

Algorithm	Number of flops
MLE	$4N_p N_s \delta + 5\zeta N_s N \log_2(N_s N)$
LCE	$4N_p \delta + N(14 + 5 \log_2 N)$

Table 3.1: Complexity of MLE and LCE for FFO recovery.

3.3.4 Low-complexity estimation of the FFO

Evaluating $\hat{\varepsilon}_{MLE}$ as indicated in the previous subsection requires a computationally demanding grid search over the $\tilde{\varepsilon}_i$ values specified in (3.27). An alternative low-complexity scheme for FFO recovery in WiMAX systems has been derived by Ruan, Reed and Shi (RRS) in [36]. This method computes the following correlations of lags $N_\delta = \lfloor N/\delta \rfloor$ and $N - N_\delta$

$$R_1 = \sum_{k=0}^{N-N_\delta-1} x(k + N_\delta) x^*(k) \quad (3.30)$$

$$R_2 = \sum_{k=0}^{N_\delta-1} x(k + N - N_\delta) x^*(k) \quad (3.31)$$

and provides an FFO estimate in a closed-form as

$$\hat{\varepsilon}_{RRS} = \frac{1}{2\pi} \arg \{R_1 R_2\}. \quad (3.32)$$

Numerical simulations shown later indicate that the accuracy of $\hat{\varepsilon}_{RRS}$ attains the ACRB at intermediate SINR values, thereby making RRS a promising candidate for practical applications. However, since $\arg \{R_1 R_2\}$ takes values in the interval $[-\pi, \pi)$, from (3.32) it follows that $\hat{\varepsilon}_{RRS}$ is ambiguous by multiples of unity. In order to remove such an ambiguity, we define a set of δ candidate FFO values $J = \{(\hat{\varepsilon}_{RRS} + m)_{\text{mod } \delta}; 0 \leq m \leq \delta - 1\}$ and look for the maximum of the ML metric $\Lambda_1(\tilde{\varepsilon})$

when $\tilde{\varepsilon} \in J$. This leads to the following low-complexity estimator (LCE)

$$\hat{\varepsilon}_{LCE} = \arg \max_{\tilde{\varepsilon} \in J} \{\Lambda_1(\tilde{\varepsilon})\} \quad (3.33)$$

which exhibits the same accuracy of RRS while extending its estimation range to the interval $[-\delta/2, \delta/2]$.

In assessing the computational burden of LCE, we observe that $\hat{\varepsilon}_{RRS}$ is obtained from (3.30)-(3.32) with N complex product plus N complex additions, for a total of $8N$ flops. Furthermore, evaluating $\hat{\varepsilon}_{LCE}$ in (3.33) requires the computation of the metric $\Lambda_1(\tilde{\varepsilon})$ for $\tilde{\varepsilon} \in J$. This is achieved as indicated in (3.17), where the quantities $\{X(N_1 + n\delta; \tilde{\varepsilon}); \tilde{\varepsilon} \in J\}$ are efficiently obtained through the N -point FFT of the sequence $\{x(k)e^{-j2\pi\tilde{\varepsilon}_{RRS}k/N}; k = 0, 1, \dots, N-1\}$. Such operations involve $N(6 + 5\log_2 N)$ flops, while additional $4N_p\delta$ flops are necessary to get $\{\Lambda_1(\tilde{\varepsilon}); \tilde{\varepsilon} \in J\}$ from the FFT output. The overall complexity of LCE is reported in the second row of Tab. 3.1.

3.4 Estimation of the integral CFO and preamble index

3.4.1 Derivation of the joint ML estimator

The estimated FFO $\hat{\varepsilon}_{LCE}$ is used to counter-rotate the received samples at an angular speed $2\pi\hat{\varepsilon}_{LCE}/N$. This produces the quantities $y(k) = e^{-j2\pi\hat{\varepsilon}_{LCE}k/N}x(k)$, which are collected into an N -dimensional vector $\mathbf{y} = [y(0), y(1), \dots, y(N-1)]^T$. To facilitate the ensuing discussion, we assume ideal FFO compensation, i.e., $\hat{\varepsilon}_{LCE} = \varepsilon$. Hence, from (3.8) and (3.10) it follows that

$$\mathbf{y} = \mathbf{\Gamma}(\eta\delta)\mathbf{F}\mathbf{P}_u\mathbf{D}(\tau_d)\mathbf{G}\mathbf{c} + \mathbf{w}' \quad (3.34)$$

where $\mathbf{w}' = \mathbf{\Gamma}^H(\hat{\varepsilon}_{LCE})\mathbf{w}$ is statistically equivalent to \mathbf{w} . Our goal is the estimation of η and the preamble index u based on the observation of \mathbf{y} . Unfortunately, the dependence of \mathbf{y} on the unknown parameters τ_d and \mathbf{c} greatly complicates this task. One possible solution is to consider τ_d and \mathbf{c} as nuisance quantities and proceed to the joint ML estimation of the extended parameter set $(\eta, u, \tau_d, \mathbf{c})$. Following this approach, we write the corresponding LLF in the form

$$\Phi(\tilde{\eta}, \tilde{u}, \tilde{\tau}_d, \tilde{\mathbf{c}}) = -N \ln(\pi\sigma_w^2) - \frac{1}{\sigma_w^2} \|\mathbf{y} - \mathbf{\Gamma}(\tilde{\eta}\delta)\mathbf{F}\mathbf{P}_{\tilde{u}}\mathbf{D}(\tilde{\tau}_d)\mathbf{G}\tilde{\mathbf{c}}\|^2 \quad (3.35)$$

and look for its global maximum over the set spanned by $(\tilde{\eta}, \tilde{u}, \tilde{\tau}_d, \tilde{\mathbf{c}})$. The maximum with respect to $\tilde{\mathbf{c}}$ occurs at

$$\hat{\mathbf{c}}(\tilde{\eta}, \tilde{u}, \tilde{\tau}_d) = (\mathbf{G}^H \mathbf{G})^{-1} \mathbf{G}^H \mathbf{D}^H(\tilde{\tau}_d) \mathbf{Z}(\tilde{\eta}, \tilde{u}) \quad (3.36)$$

with $\mathbf{Z}(\tilde{\eta}, \tilde{u}) = \mathbf{P}_{\tilde{u}}^H \mathbf{F}^H \mathbf{\Gamma}^H(\tilde{\eta} \delta) \mathbf{y}$. Denoting by

$$Y(n) = \frac{1}{\sqrt{N}} \sum_{k=0}^{N-1} y(k) e^{-j2\pi nk/N} - \frac{N}{2} \leq n \leq \frac{N}{2} - 1 \quad (3.37)$$

the N -point DFT of \mathbf{y} , we may put the entries of $\mathbf{Z}(\tilde{\eta}, \tilde{u})$ in the form

$$Z(\tilde{\eta}, \tilde{u}; n) = p_{\tilde{u}}^*(n) Y(N_1 + n\delta + \tilde{\eta}\delta) \quad 0 \leq n \leq N_p - 1 \quad (3.38)$$

which can be physically interpreted as the cross-correlation of the \tilde{u} th pilot sequence with the hypothesized set of modulated subcarriers. Substituting (3.36) back into (3.35) and skipping some irrelevant additive terms independent of $(\tilde{\eta}, \tilde{u}, \tilde{\tau}_d)$, yields the concentrated LLF

$$\Phi_1(\tilde{\eta}, \tilde{u}, \tilde{\tau}_d) = \mathbf{Z}^H(\tilde{\eta}, \tilde{u}) \mathbf{D}(\tilde{\tau}_d) \mathbf{B}_1 \mathbf{D}^H(\tilde{\tau}_d) \mathbf{Z}(\tilde{\eta}, \tilde{u}) \quad (3.39)$$

with $\mathbf{B}_1 = \mathbf{G}(\mathbf{G}^H \mathbf{G})^{-1} \mathbf{G}^H$. After standard computations, it turns out that (3.39) can be equivalently rewritten as

$$\Phi_1(\tilde{\eta}, \tilde{u}, \tilde{\tau}_d) = \rho_0(\tilde{\eta}) + 2\Re \left\{ \sum_{m=1}^{N_p-1} \rho_m(\tilde{\eta}, \tilde{u}) e^{j2\pi m \tilde{\tau}_d \delta / N} \right\} \quad (3.40)$$

with

$$\rho_m(\tilde{\eta}, \tilde{u}) = \sum_{n=m}^{N_p-1} [\mathbf{B}_1]_{n-m, n} Z(\tilde{\eta}, \tilde{u}; n) Z^*(\tilde{\eta}, \tilde{u}; n-m) \quad (3.41)$$

from which the joint MLE of the unknown parameters is eventually obtained as

$$(\hat{\eta}, \hat{u}, \hat{\tau}_d)_{MLE} = \arg \max_{(\tilde{\eta}, \tilde{u}, \tilde{\tau}_d)} \{\Phi_1(\tilde{\eta}, \tilde{u}, \tilde{\tau}_d)\}. \quad (3.42)$$

Unfortunately, implementation of the MLE as indicated in (3.42) requires a grid-search over the multi-dimensional domain spanned by $(\tilde{\eta}, \tilde{u}, \tilde{\tau}_d)$. Since this operation is computationally unfeasible, in the next subsection we make some approximations to the MLE and arrive at a suboptimal but practically implementable scheme for the joint estimation of η and u .

3.4.2 Simplification of the joint ML estimator

We begin by observing that $\mathbf{G}^H \mathbf{G}$ is an $L \times L$ Toeplitz matrix with entries

$$[\mathbf{G}^H \mathbf{G}]_{\ell_1, \ell_2} = e^{j\pi(\ell_1 - \ell_2)(N_p - 1)\delta/N} N_p f_{N_p}[(\ell_1 - \ell_2)N_p \delta/N] \quad 0 \leq \ell_1, \ell_2 \leq L-1 \quad (3.43)$$

where $f_N(x)$ is defined in (3.24). Inspection of (3.43) reveals that $\mathbf{G}^H \mathbf{G}$ reduces to $N_p \mathbf{I}_L$ in the specific case $N_p \delta = N$ and under the reasonable assumption that $L < N_p$. In a more general situation where the ratio $N_p \delta/N$ is close to unity, we expect that replacing $\mathbf{G}^H \mathbf{G}$ by $N_p \mathbf{I}_L$ may only lead to a negligible perturbation of the ML estimates. Thus, a first simplification of MLE is achieved by assuming $\mathbf{G}^H \mathbf{G} \simeq N_p \mathbf{I}_L$, which amounts to replacing \mathbf{B}_1 in (3.39) with a new matrix $\mathbf{B}_2 = (\mathbf{G} \mathbf{G}^H)/N_p$ such that

$$[\mathbf{B}_2]_{n_1, n_2} = \frac{L}{N_p} e^{j\pi(n_2 - n_1)(L-1)\delta/N} f_L[(n_2 - n_1)\mu] \quad 0 \leq n_1, n_2 \leq N_p - 1 \quad (3.44)$$

with $\mu = L\delta/N$. This results into a modified objective function

$$\Phi_2(\tilde{\eta}, \tilde{u}, \tilde{\tau}_T) = \frac{L}{N_p} R_0(\tilde{\eta}) \frac{2L}{N_p} \Re \left\{ \sum_{m=1}^{N_p-1} f_L(m\mu) R_m(\tilde{\eta}, \tilde{u}) e^{j2\pi m \tilde{\tau}_T \delta/N} \right\} \quad (3.45)$$

where

$$R_m(\tilde{\eta}, \tilde{u}) = \sum_{n=m}^{N_p-1} Z(\tilde{\eta}, \tilde{u}; n) Z^*(\tilde{\eta}, \tilde{u}; n-m) \quad (3.46)$$

is the auto-correlation of the sequence $Z(\tilde{\eta}, \tilde{u}; n)$ with lag m , while

$$\tilde{\tau}_T = \tilde{\tau}_d + \frac{L-1}{2} \quad (3.47)$$

can be interpreted as the (hypothesized) overall timing misalignment of the received training sequence, comprising both the residual timing error $\tilde{\tau}_d$ plus the average delay $(L-1)/2$ introduced by an unknown CIR of order L .

A second simplification arises after substituting (3.34), (3.37) into (3.38) and letting $(\tilde{\eta}, \tilde{u}) = (\eta, u)$. After some manipulations, this yields

$$Z(\eta, u; n) = A^2 H(N_1 + m_u + n\delta) e^{-j2\pi\tau_d(N_1 + m_u + n\delta)} + \gamma(n) \quad (3.48)$$

where $H(n)$ is the channel frequency response given in (3.4) and $\gamma(n)$ is a disturbance term. Since the channel gains over subcarriers separated by $m\delta\Delta f$ in the frequency

domain become less and less correlated as m grows large, we expect that the correlation $R_m(\tilde{\eta}, \tilde{u})$ in (3.46) decreases with m when $(\tilde{\eta}, \tilde{u}) = (\eta, u)$. Accordingly, the summation index in (3.45) can be limited to some interval $1 \leq m \leq M$, with $M < N_p - 1$ being a design parameter that must be carefully chosen so as to achieve a desired trade-off between performance and system complexity. Furthermore, since the term $R_0(\tilde{\eta})$ collects the energy over the set of N_p hypothesized training subcarriers, its dependence on $\tilde{\eta}$ is expected to be negligible if $\tilde{\eta} - \eta$ is relatively small compared to N_p . This is easily seen by assuming a frequency-flat channel with $H(n) = 1$ and ignoring the noise and ICI contributions, which leads to $R_0(\tilde{\eta}) = A^4(N_p - |\tilde{\eta} - \eta|)$. Hence, neglecting the term $R_0(\tilde{\eta})$ and an irrelevant factor, the metric (3.45) reduces to

$$\Phi_3(\tilde{\eta}, \tilde{u}, \tilde{\tau}_T) = \Re \left\{ \sum_{m=1}^M f_L(m\mu) R_m(\tilde{\eta}, \tilde{u}) e^{j2\pi m \tilde{\tau}_T \delta / N} \right\}. \quad (3.49)$$

A further simplification of the objective function is obtained by removing its dependence on $\tilde{\tau}_T$ by means of the following heuristic arguments. Our idea relies on the observation that the channel gains at neighboring preamble subcarriers have approximately the same amplitude and only differ for a phase shift which is proportional to the channel delay spread $\tau_T - \tau_d$. Bearing this fact in mind, after substituting (3.48) into (3.46) we get

$$R_m(\eta, u) \simeq A^4 e^{-j2\pi m \tau_T \delta / N} \sum_{n=m}^{N_p-1} |H(N_1 + m_u + n\delta)|^2 \quad (3.50)$$

where we have neglected the disturbance term $\gamma(n)$ for the sake of simplicity. This equation indicates that, apart for noise and ICI, the argument of $R_m(\eta, u)$ is equal to $-2\pi m \tau_T \delta / N$ and an estimate of τ_T can thus be obtained for each candidate pair $(\tilde{\eta}, \tilde{u})$ as

$$\hat{\tau}_T(\tilde{\eta}, \tilde{u}) = -\frac{N}{2\pi\delta M} \sum_{m=1}^M \arg\{R_m(\tilde{\eta}, \tilde{u}) R_{m-1}^*(\tilde{\eta}, \tilde{u})\} \quad (3.51)$$

with $R_0(\tilde{\eta}, \tilde{u}) = 1$. Such an estimate is next used in (3.49) in place of $\tilde{\tau}_T$, yielding the final metric

$$\Phi_4(\tilde{\eta}, \tilde{u}) = \Re \left\{ \sum_{m=1}^M f_L(m\mu) R_m(\tilde{\eta}, \tilde{u}) e^{j2\pi m \hat{\tau}_T(\tilde{\eta}, \tilde{u}) \delta / N} \right\} \quad (3.52)$$

from which the approximate ML estimate (AMLE) of (η, u) is derived as

$$(\hat{\eta}, \hat{u})_{AMLE} = \arg \max_{(\tilde{\eta}, \tilde{u})} \{\Phi_4(\tilde{\eta}, \tilde{u})\}. \quad (3.53)$$

Inspection of (3.53) indicates that the AMLE requires a bidimensional grid search over all possible candidate pairs $(\tilde{\eta}, \tilde{u})$, where $\tilde{u} \in I_U$ and $\tilde{\eta}$ is an integer belonging to a set I_η which is specified by the maximum expected CFO value.

3.4.3 Remarks

The following remarks are of interest:

i) From (3.46) and (3.52), it follows that AMLE can be interpreted as a kind of differential detector in the frequency domain, where only a small number M of correlation values $\{R_m(\tilde{\eta}, \tilde{u}); m = 1, 2, \dots, M\}$ are employed in order to keep the computational load to a tolerable level. Since the correlation coefficient between $Z(\eta, u; n)$ and $Z(\eta, u; n-m)$ reduces with m as a consequence of the channel frequency selectivity, we expect that the amount of information conveyed by $R_m(\tilde{\eta}, \tilde{u})$ on the unknown parameters (η, u) decreases with m as well. This explains why the weighting coefficients $\{f_L(m\mu)\}$ in (3.52) become smaller and smaller as m grows large.

ii) Letting $M = 1$ in (3.52) and skipping the irrelevant factor $f_L(\mu)$, yields

$$\Phi_4(\tilde{\eta}, \tilde{u}) = |R_1(\tilde{\eta}, \tilde{u})| \quad (3.54)$$

which represents a modified version of the metric employed by the conventional estimator (CE) [39]- [41]

$$\Phi_{CE}(\tilde{\eta}, \tilde{u}) = \Re \{R_1(\tilde{\eta}, \tilde{u})\}. \quad (3.55)$$

Intuitively speaking, the use of the magnitude of $R_1(\tilde{\eta}, \tilde{u})$ in place of its real component makes AMLE more robust than CE in the presence of residual timing errors.

iii) Comparing (3.52) with (3.55), we see that AMLE represents an extension of CE in two directions. On one hand, the former exploits an increased number of correlations $R_m(\tilde{\eta}, \tilde{u})$ than the latter. On the other hand, the phase correction term $2\pi m\hat{\tau}_T(\tilde{\eta}, \tilde{u})\delta/N$ employed in (3.52) reduces the sensitivity of AMLE to timing errors.

iv) The processing load of AMLE can be assessed as follows. Neglecting the complexity involved with the N -point FFT of \mathbf{y} and denoting by N_η the cardinality of I_η , it turns out that $6M(N_p + N_\eta - 1) + 2MN_pN_\eta N_U$ flops are required to evaluate

the correlations $R_m(\tilde{\eta}, \tilde{u})$ for $m = 1, 2, \dots, M$ and $(\tilde{\eta}, \tilde{u}) \in I_\eta \times I_U$. Next, we observe that computing $\hat{\tau}_T(\tilde{\eta}, \tilde{u})$ in (3.51) needs $7M$ flops for each pair $(\tilde{\eta}, \tilde{u}) \in I_\eta \times I_U$, while $5M$ additional flops are involved in the evaluation of $\Phi_4(\tilde{\eta}, \tilde{u})$ in (3.52). This leads to the overall complexity of AMLE as summarized in the first row of Tab. 3.2. For comparison, in Tab. 3.2 we also report the number of flops required by CE.

Algorithm	Number of flops
AMLE	$2M(3N_p + 3N_\eta + 6N_UN_\eta + N_pN_UN_\eta)$
CE	$3(N_p + N_\eta) + N_pN_UN_\eta$

Table 3.2: Complexity of AMLE and CE for the joint recovery of IFO and preamble index.

$v)$ As mentioned, the cell segment m_u and cell ID ℓ_u are univocally determined by the preamble index u and are recovered from \hat{u} using the mapping rule $\hat{u} \rightarrow (m_{\hat{u}}, \ell_{\hat{u}})$ specified in [11]. Furthermore, recalling that $f_d = \nu - m_u$ with $\nu = \varepsilon + \eta\delta$, we can use the triplet $(\hat{\varepsilon}, \hat{\eta}, m_{\hat{u}})$ to get the CFO estimate in the form

$$\hat{f}_d = \hat{\varepsilon} + \hat{\eta}\delta - m_{\hat{u}}. \quad (3.56)$$

3.5 Simulation results

3.5.1 System parameters

The downlink synchronization algorithms developed in the previous sections are applied to a WiMAX system compliant with the IEEE 802.16e standard for wireless MANs [11]. The DFT size is $N = 1024$, with a CP composed by 128 samples. The sampling period is $T_s = 89.28$ ns, corresponding to a subcarrier spacing of 10.94 kHz. There are a total of 114 possible training sequences of length $N_p = 284$, which are specified by the preamble index u . At each simulation run, a new value of u is randomly chosen in the set $I_U = \{0, 1, \dots, 113\}$ with equal probability, and the associated preamble sequence is taken from Table 438 of [11]. The pilot symbols belong to a BPSK constellation with amplitude $A = 2\sqrt{2}$, which corresponds to a power boosting of 9 dB. The non-zero subcarriers in each preamble sequence are spaced three subcarriers apart. Their indices are given in (3.1), where $\delta = 3$, $N_1 = -426$ and $m_u \in \{0, 1, 2\}$. The discrete-time CIR is composed by $L = 40$ channel coefficients. The latter are modeled as independent circularly symmetric

Gaussian random variables with zero-mean (Rayleigh fading) and an exponentially decaying power delay profile

$$\mathbb{E}\{|h(\ell)|^2\} = \lambda \exp(-\ell/L) \quad 0 \leq \ell \leq L-1 \quad (3.57)$$

where the constant λ is chosen such that the average energy of the CIR is normalized to unity, i.e., $\mathbb{E}\{\|\mathbf{h}\|^2\} = 1$. A channel snapshot is generated at each simulation run and kept fixed over the training preamble. The range of CFO values is related to the oscillator instability, while it is only marginally affected by the Doppler shift induced by the MT speed. Hence, assuming a carrier frequency of 5 GHz and an oscillator instability of ± 10 parts-per-million (ppm) at both the transmitter and receiver ends, the CFO value f_d lies within ± 9 subcarrier spacing. Recalling that $\nu = f_d + m_u = \varepsilon + \eta\delta$ with $m_u \in \{0, 1, 2\}$, $\varepsilon \in [-\delta/2, \delta/2)$ and $\delta = 3$, it follows that the search range for the IFO is $I_\eta = \{0, \pm 1, \pm 2, \pm 3, 4\}$ and the bidimensional search in (3.53) is thus made over a total of 114×8 possible IFO-preamble index pairs. As mentioned, inter-cell interference and thermal noise are collectively treated as a white Gaussian process and the system performance is assessed at different SINR values.

3.5.2 Performance assessment

Figure 3.3 illustrates the accuracy of the FFO estimates provided by MLE and LCE in terms of their mean square error, which is defined as $MSE = \mathbb{E}\{(\hat{\varepsilon} - \varepsilon)^2\}$, vs. the SINR. Marks indicate simulation results, while solid lines are drawn to ease the reading of the graphs. The CFO is randomly generated at each simulation run with uniform distribution within the interval $[-\delta/2, \delta/2)$, which amounts to letting $\eta = 0$. The ACRB given in (3.21) is represented by the dashed line and used as a benchmark to the accuracy of the considered schemes. The MLE is implemented through a coarse search with pruning factor N_s followed by a cubic interpolation (fine search). Intuitively speaking, we expect that increasing N_s will reduce the interpolation error at the price of a corresponding increase of the computational burden. This intuition is confirmed by the numerical results shown in Fig. 3.3, where the MLE curves are plagued by an error floor which reduces as N_s grows large. The floor is particularly evident with $N_s = 4$, but it nearly disappears when $N_s = 16$. It is worth noting that the accuracy of the LCE keeps close to the ACRB at all SINR values of practical interest. The performance of the joint estimators of the IFO and preamble index is assessed in

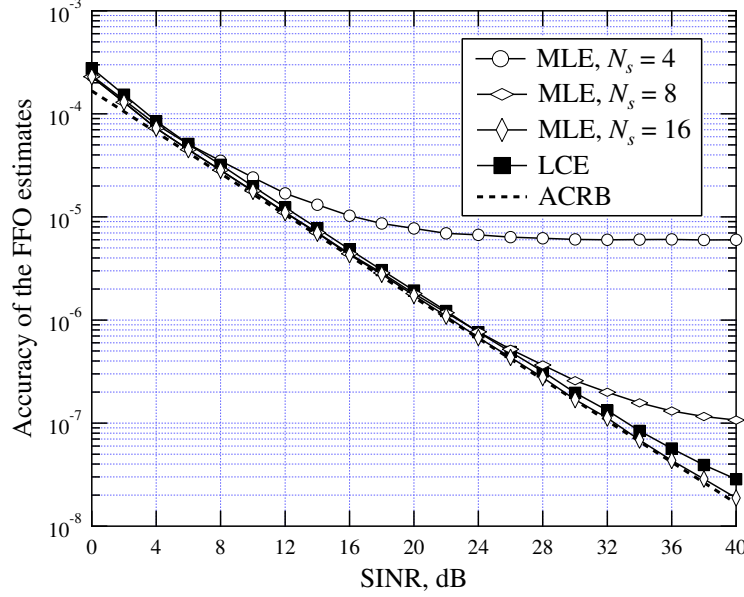


Figure 3.3: MSE of the FFO estimates provided by MLE and LCE versus SINR.

terms of their *failure* probability, which is defined as $P_f = \Pr\{(\hat{\eta}, \hat{u}) \neq (\eta, u)\}$. The latter is illustrated in Fig. 3.4 as a function of the SINR in the ideal case of perfect FFO compensation (i.e., $\hat{\varepsilon} = \varepsilon$) and in the absence of any residual timing error (i.e., $\tau_d = 0$). The best results are obtained with MLE, which provides a benchmark to the performance of both AMLE and CE. As expected, the detection capability of AMLE improves with M . Actually, the loss with respect to MLE is nearly 3 dB when $M = 1$ and reduces to 1 dB for $M = 3$. As for CE, it performs slightly better than the AMLE with $M = 1$. This fact can be explained by recalling that for $M = 1$ the AMLE employs the magnitude of $R_1(\tilde{\eta}, \tilde{u})$ for the estimation of (η, u) in order to reduce the impact of residual timing errors on the system performance. Such an advantage, however, is achieved at the price of some noise enhancement with respect to the CE metric shown in (3.55). Hence, in the absence of any timing error, taking the real part of $R_1(\tilde{\eta}, \tilde{u})$ as indicated in (3.55) results into an improved detection capability with respect to using the AMLE metric in (3.54). Figures 3.5 and 3.6 show P_f vs. SINR in case of perfect FFO compensation and for $\tau_d = 20$ and $\tau_d = 40$, respectively. Comparing these results with those in Fig. 3.4, we see that both MLE and AMLE are virtually insensitive to the timing error, while the performance of

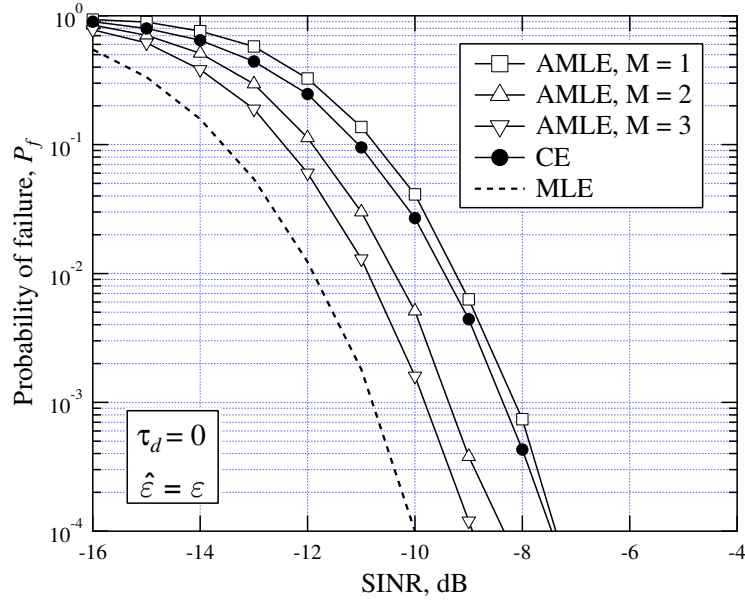


Figure 3.4: Probability of failure versus SINR for $\tau_d = 0$ and $\hat{\varepsilon} = \varepsilon$.

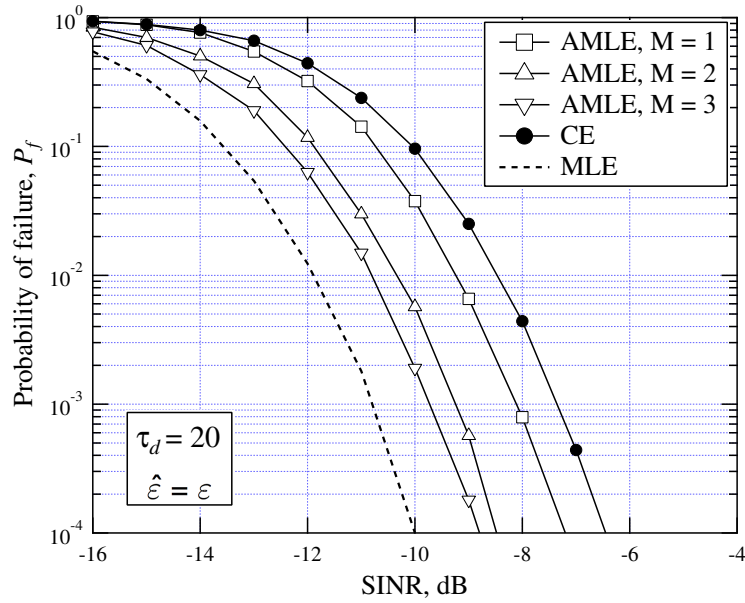


Figure 3.5: Probability of failure versus SINR for $\tau_d = 20$ and $\hat{\varepsilon} = \varepsilon$.

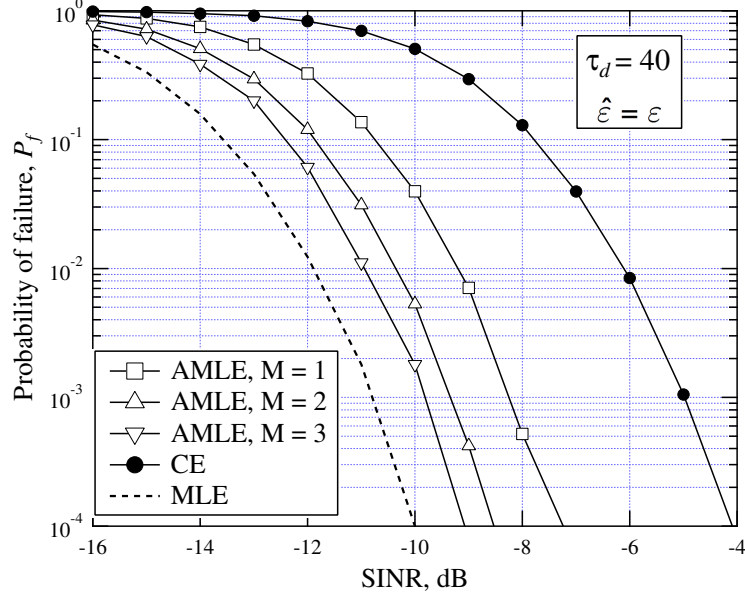


Figure 3.6: Probability of failure versus SINR for $\tau_d = 40$ and $\hat{\varepsilon} = \varepsilon$.

CE progressively degrades with τ_d . Indeed, the loss of CE with respect to MLE is 2.5 dB when $\tau_d = 0$ and becomes 6 dB when τ_d increases to 40. Such a remarkable sensitivity of CE to residual timing errors must be ascribed to the use of the real part in the metric $\Phi_{CE}(\tilde{\eta}, \tilde{u})$ shown in (3.55). In fact, letting $m = 1$ into (3.50) and substituting the result into (3.55) we see that, apart for noise and ICI, $\Phi_{CE}(\tilde{\eta}, \tilde{u})$ is proportional to $\cos(2\pi\tau_T\delta/N)$. The latter may be interpreted as an attenuation factor whose magnitude reduces with the timing error and leads to a corresponding SINR loss. This problem does not occur with the AMLE metric (3.54), where the real part of $R_1(\tilde{\eta}, \tilde{u})$ is replaced by the modulo operation. The impact of residual timing errors on the system performance is further investigated in Fig. 3.7, which illustrates P_f as a function of τ_d for an SINR of -10 dB. These results emphasize the remarkable insensitivity of AMLE to τ_d . In contrast, the detection capability of CE is significantly impaired by τ_d , which represents a major disadvantage of this scheme with respect to AMLE. So far, ideal FFO compensation has been assumed in assessing the performance of the joint estimators of the IFO and preamble index. At this stage, it is interesting to investigate how the accuracy of these schemes is affected by imperfect FFO compensation. Figure 3.8 shows P_f as a function of the residual FFO $\Delta\varepsilon = \hat{\varepsilon} - \varepsilon$ for both AMLE and CE. The SINR is fixed to -10 dB, while the

timing error is $\tau_d = 20$.

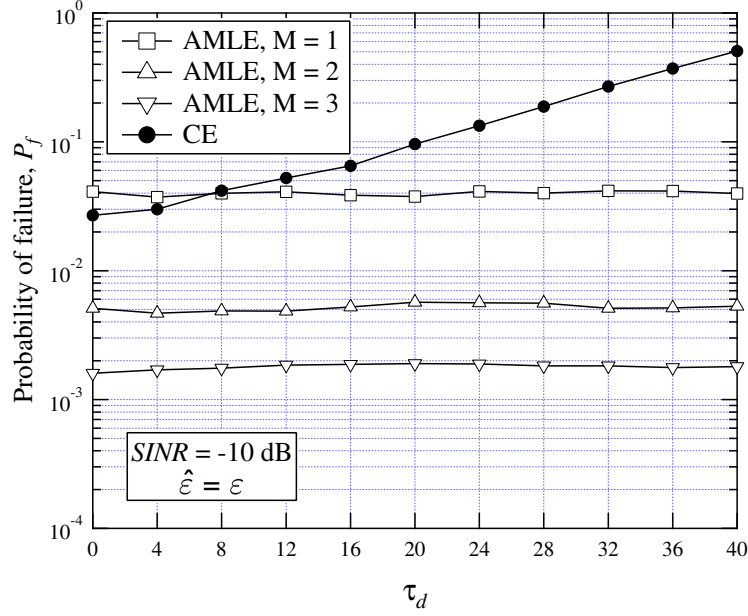


Figure 3.7: Probability of failure versus τ_d for $SINR=-10$ dB and $\hat{\epsilon} = \epsilon$.

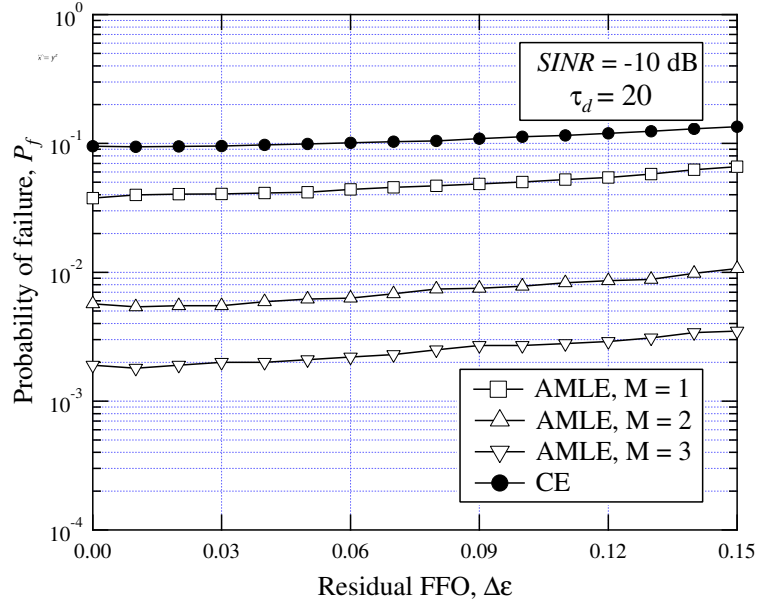


Figure 3.8: Probability of failure versus $\Delta\epsilon$ for $SINR=-10$ dB and $\tau_d = 20$.

As expected, P_f increases with $\Delta\varepsilon$ as a consequence of the interchannel interference arising from the presence of $\Delta\varepsilon$. However, such an increase is marginal even for values of $\Delta\varepsilon$ as large as 10% of the subcarrier spacing. Since the MSE of $\hat{\varepsilon}_{LCE}$ in Fig. 3.3 is approximately 10^{-4} at SINR = 3 dB, in practical applications the detection capability of AMLE and CE should not be significantly impaired by imperfect FFO compensation.

3.5.3 Complexity comparison

We conclude our study by comparing the investigated schemes in terms of their computational complexity. In the considered scenario with $N = 1024$, $N_p = 284$ and $\delta = 3$, from Tab. 3.1 it follows that FFO recovery by means of MLE approximately requires 249 kflops when $N_s = 4$, while 508 or 1027 kflops are needed with $N_s = 8$ or 16, respectively. On the other hand, LCE is implemented with only 69 kflops, thereby achieving the same accuracy of MLE with a significant computational saving. This feature makes LCE a promising candidate for FFO recovery in WiMAX systems. The complexity of AMLE and CE for the joint recovery of the IFO and preamble index is obtained by substituting $N_U = 114$ and $N_\eta = 8$ in Tab. 3.2. It turns out that application of AMLE needs $530M$ kflops, while only 260 kflops are required by CE. This means that the improved performance of AMLE with respect to CE is achieved at the price of an increase of the computational load by a factor of nearly $2M$. Hence, satisfactory performance can be achieved with affordable complexity only with a judicious design of M .

3.6 Concluding remarks

We have investigated the joint ML estimation of the CFO and preamble index in multicarrier systems that employ a training sequence composed by some correlated but non-identical parts. Our study applies to the OFDMA-mode of WiMAX networks compliant with the IEEE 802.16 family of standards. A novel expression of the CRB for CFO recovery is also derived as a benchmark to the accuracy of the frequency estimates. Although in principle the resulting ML metric is able to identify the CFO in one single step, it is convenient to decompose the frequency error into a fractional part (FFO) plus a remaining integer part (IFO). In order to avoid the huge complexity

of the exact ML solution, the FFO is recovered by resorting to an ad-hoc frequency estimation method which is shown to achieve the relevant CRB at all SINR values of practical interest. After FFO estimation and compensation, the IFO and preamble index are jointly retrieved using an approximated ML approach which is made robust against residual timing errors. Compared with existing alternatives suited for the WiMAX preamble, our scheme exhibits improved detection capability at the price of an increase of the computational burden. This offers the opportunity of achieving the desired trade-off between complexity and system performance.

3.7 Appendix

In this Appendix we highlight the major steps leading to the CRB in the estimation of (ξ_u, ν) . For this purpose, we call $\xi_{u,R}$ and $\xi_{u,I}$ the real and imaginary parts of ξ_u and let $\varphi = [\xi_{u,R}^T, \xi_{u,I}^T, \nu]^T$ be the set of unknown parameters. Then, the components of the Fisher information matrix \mathbf{F}_φ are given by [4]

$$[\mathbf{F}_\varphi]_{i,j} = -\mathbb{E} \left\{ \frac{\partial^2 \Lambda(\varphi)}{\partial \varphi(i) \partial \varphi(j)} \right\} \quad 1 \leq i, j \leq 2N_p + 1 \quad (3.58)$$

where $\Lambda(\varphi)$ is the LLF in (3.13), while $\varphi(k)$ denotes the k th entry of φ . Substituting (3.13) into (3.58), after standard computations we get

$$\mathbf{F}_\varphi = \frac{2}{\sigma_w^2} \begin{bmatrix} \mathbf{I}_{N_p} & \mathbf{0}_{N_p} & -\Im\{\mathbf{v}_u\} \\ \mathbf{0}_{N_p} & \mathbf{I}_{N_p} & \Re\{\mathbf{v}_u\} \\ -\Im\{\mathbf{v}_u^H\} & \Re\{\mathbf{v}_u^H\} & \|\mathbf{Q}\mathbf{F}\xi_u\|^2 \end{bmatrix} \quad (3.59)$$

where $\mathbf{v}_u = \mathbf{F}^H \mathbf{Q} \mathbf{F} \xi_u$ and

$$\mathbf{Q} = \text{diag} \left\{ \frac{2\pi k}{N}; k = 0, 1, \dots, N-1 \right\}. \quad (3.60)$$

The CRB for the estimation of ν is given by $[\mathbf{F}_\varphi^{-1}]_{2N_p+1, 2N_p+1}$. Hence, applying to (3.59) the formulas for the inverse of a partitioned matrix, we obtain

$$\text{CRB}\{\nu\} = \frac{\sigma_w^2}{2\xi_u^H \mathbf{F}^H \mathbf{Q} \mathbf{F} (\mathbf{I}_N - \mathbf{F} \mathbf{F}^H) \mathbf{Q} \mathbf{F} \xi_u} \quad (3.61)$$

which depends on the specific realization of ξ_u . A simpler bound independent of ξ_u is the asymptotic CRB (ACRB), which is evaluated by averaging the denominator of

(3.61) with respect to $\boldsymbol{\xi}_u$ [47]. For this purpose, we model the pilot symbols $p_u(n)$ as statistically independent random variables with zero mean and power A^2 . Hence, from (3.6) it follows that $\boldsymbol{\xi}_u$ has zero-mean and covariance matrix $\sigma_H^2 A^2 \mathbf{I}_{N_p}$. Using this result and bearing in mind (3.5), after some computations we obtain

$$\text{ACRB}\{\nu\} = \frac{N_p (\text{SINR})^{-1}}{2N \cdot \text{tr}\{\mathbf{Q}^2 \mathbf{F} \mathbf{F}^H - \mathbf{Q} \mathbf{F} \mathbf{F}^H \mathbf{Q} \mathbf{F} \mathbf{F}^H\}} \quad (3.62)$$

which can also be rewritten as indicated in (3.21) and (3.22).

Chapter 4

Frequency Estimation in OFDM Direct-Conversion Receivers

4.1 Introduction

Orthogonal frequency-division multiplexing (OFDM) is a popular multicarrier technology which offers remarkable resilience against multipath distortions, increased spectral efficiency and the possibility of performing adaptive modulation and coding. Due to such potential advantages, it has been adopted in several wideband commercial systems, including the IEEE 802.11a wireless local area network (WLAN) [48], the IEEE 802.16 wireless metropolitan area network (WMAN) [11] and the 3GPP long-term evolution (LTE) [9].

In recent years, the combination of OFDM with the direct-conversion receiver (DCR) concept has attracted considerable attention as an effective mean for the implementation of user terminals with reduced size and power consumption [49]. In contrast to the classical superheterodyne architecture, in a DCR device the radio-frequency (RF) signal is down-converted to baseband without passing through any intermediate-frequency (IF) stage. On one hand, this approach avoids the use of expensive image rejection filters and other off-chip components, with a remarkable advantage in terms

of cost and circuit board size. On the other hand, a DCR front-end introduces some RF/analog imbalances arising from the use of in-phase/quadrature (I/Q) low-pass filters (LPFs) with mismatched frequency responses and from local oscillator (LO) signals with unequal amplitudes and imperfect 90° phase difference. While the LO-induced imbalance can be considered as frequency-flat, filter mismatches can vary substantially over the signal bandwidth and are particularly critical in wideband communication systems [50]. Overall, I/Q non-idealities give rise to a conjugate mirror-image interference on the down-converted baseband signal which can seriously degrade the system performance if not properly compensated. An OFDM receiver also exhibits a remarkable sensitivity to the carrier frequency offset (CFO) between the received waveform and the LO signals, which originates inter-channel interference (ICI) at the output of the discrete Fourier transform (DFT) unit. It follows that accurate estimation and compensation for CFO and I/Q imbalance is mandatory in order to benefit all the potential advantages promised by the OFDM/DCR combination.

An intense research activity has been recently devoted to the problem of CFO recovery in OFDM systems plagued by frequency-selective I/Q imperfections. The methods presented in [51] and [52] exploit a dedicated training preamble (TP) composed of three repeated parts to retrieve the cosine of the normalized CFO. However, since the cosine is an even function of its argument, the corresponding frequency estimate is affected by a inherent sign ambiguity, which severely limits the accuracy in case of small CFO values. A similar problem occurs in [53], where a low-complexity scheme is suggested to jointly compensate for the CFO and I/Q imbalances. In [54]–[56] the original preamble proposed in [51] is extended by a second part which is intentionally rotated by an artificial frequency shift before transmission. The resulting TP allows one to recover both the cosine and the sine of the CFO, which are eventually combined to get unambiguous estimates of the frequency offset. A similar approach is adopted in [57] and [58], where the sign ambiguity problem is fixed by rotating the repeated parts of the TP by a specified phase pattern. Albeit effective, all the aforementioned solutions cannot be applied to practical OFDM systems since they rely on suitably designed TPs that cannot be found in any commercial standard.

The schemes presented in [59]–[63] exploit the conventional repeated TP specified by the IEEE 802.11a WLAN standard. Specifically, in [59] the authors present a suitable matrix formulation of the received signal samples to derive novel sine and cosine-based CFO estimators, while the frequency-domain correlations of the TP are used in [60].

An alternative cosine-based estimator is derived in [61] using a general relation among three arbitrary segments of the repeated TP, while the signal parameters via rotational invariance technique (ESPRIT) [64] is applied in [62] after interpreting the useful signal component and its mirror image as the contributions of two independent sinusoidal waveforms. Finally, an iterative interference-cancellation approach is presented in [63] by resorting to the space-alternating generalized expectation-maximization (SAGE) algorithm [65].

This chapter provides a theoretical investigation of the CFO recovery problem for an OFDM receiver affected by frequency-selective I/Q imbalance. In doing so, we adopt a maximum-likelihood (ML) oriented approach and consider a burst-mode transmission wherein each frame is preceded by the conventional repeated TP. One major outcome of our study originates from the common belief that conventional CFO estimators derived without taking RF imperfections into account cannot work properly when applied to a DCR architecture. However, so far only numerical measurements have been used to support such a prevailing idea and any solid theoretical analysis is still missing. In order to fill such a gap, in our study we first review the classical ML (CML) frequency estimator presented in [45] and analytically evaluate its accuracy in the presence of I/Q imbalance. This provides the system designer with useful guidelines about the possibility of using the CML in a practical OFDM direct-conversion receiver. Next, we assess the theoretical performance of the algorithm presented in [57] for the joint ML (JML) estimation of the CFO, the channel-distorted TP and its mirror image. Such an analysis was not provided in [57] and represents a second contribution of this chapter. As we shall see, JML is very sensitive to the magnitude of the CFO value and fails whenever the CFO becomes vanishingly small. Motivated by such a result, we also derive a novel ML-based estimator of all unknown parameters which exploits some side information about the average signal-to-image ratio (SIR). Interestingly, such an estimator serves as a joining link between CML and JML since the latter schemes are obtained from the former by simply adjusting a suitable design parameter. A last contribution of this study is the derivation of the Cramer-Rao bound (CRB) for CFO recovery in the presence of I/Q imbalance using the true noise statistics. This result is of paramount importance as it can be used to check whether the approximated bound derived under the traditional white Gaussian noise (WGN) assumption deviates substantially or not from the true CRB.

4.2 Signal model in the presence of I/Q imbalance

4.2.1 Direct conversion receiver

Fig. 4.1 illustrates the basic DCR architecture in the presence of I/Q imbalances. The latter originate from the use of I/Q filters with mismatched impulse responses $g_I(t)$ and $g_Q(t)$, as well as from LO signals with an amplitude imbalance α and a phase error ψ . While LO imperfections can be considered as frequency-independent [57], filter mismatches vary over the signal bandwidth, thereby resulting into a frequency-selective imbalance.

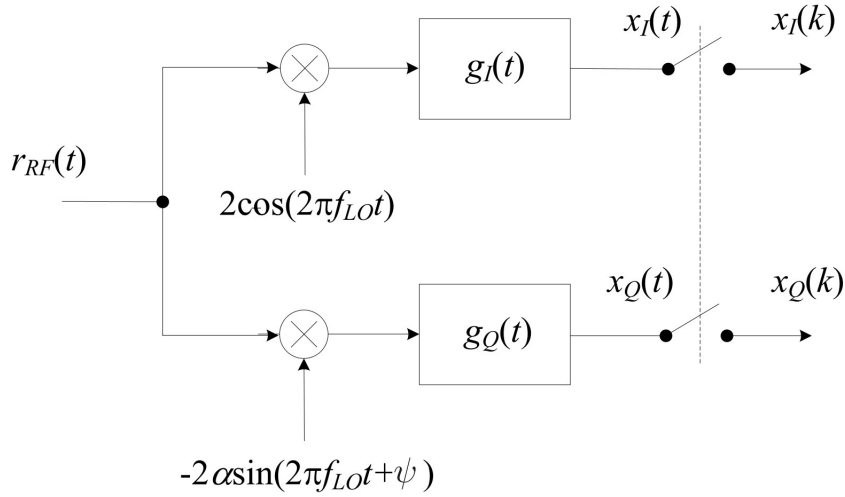


Figure 4.1: Basic architecture of a direct-conversion receiver.

The baseband equivalent of the receiver front-end is depicted in Fig. 4.2. Here, $r(t)$ is the complex envelope of the received waveform with respect to the carrier frequency f_0 , while $\Delta f = f_0 - f_{LO}$ is the offset between the carrier and the LO frequencies.

Denoting by $s(t)$ and $v(t)$ the baseband representations of the transmitted signal and propagation channel, respectively, we have $r(t) = s(t) \otimes v(t) + n(t)$, where $n(t)$ is circularly symmetric Additive WGN (AWGN) with two-sided power spectral density $2N_0$. From the analysis in [66], it follows that the down-converted baseband signal $x(t) = x_I(t) + jx_Q(t)$ can be written as

$$x(t) = e^{j2\pi\Delta f t} [s(t) \otimes h(t)] + e^{-j2\pi\Delta f t} [s^*(t) \otimes q(t)] + w(t) \quad (4.1)$$

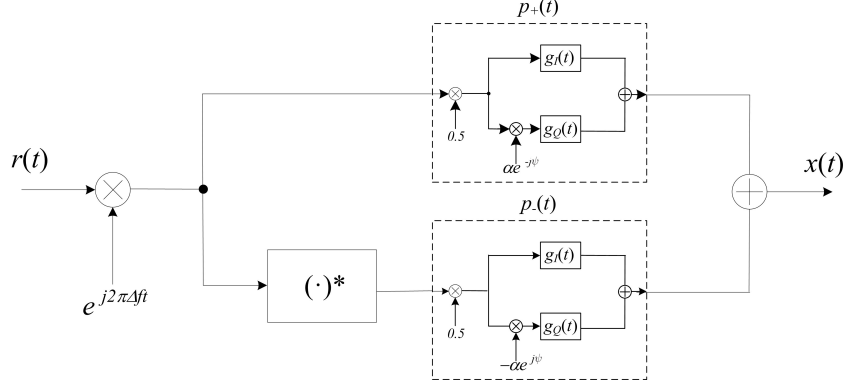


Figure 4.2: Baseband equivalent of the receiver front-end.

where the impulse responses $h(t)$ and $q(t)$ are defined as

$$\begin{aligned} h(t) &= v(t) \otimes p_+(t) e^{-j2\pi\Delta f t} \\ q(t) &= v^*(t) \otimes p_-(t) e^{j2\pi\Delta f t} \end{aligned} \quad (4.2)$$

with

$$\begin{aligned} p_+(t) &= \frac{1}{2} [g_I(t) + \alpha g_Q(t) e^{-j\psi}] \\ p_-(t) &= \frac{1}{2} [g_I(t) - \alpha g_Q(t) e^{j\psi}] \end{aligned} \quad (4.3)$$

while the noise term $w(t)$ is related to $n(t)$ by

$$w(t) = n(t) e^{j2\pi\Delta f t} \otimes p_+(t) + n^*(t) e^{-j2\pi\Delta f t} \otimes p_-(t). \quad (4.4)$$

Letting $w(t) = w_I(t) + jw_Q(t)$ and observing that $n(t) e^{j2\pi\Delta f t}$ is statistically equivalent to $n(t)$, from (4.3) and (4.4) it follows that $w_I(t)$ and $w_Q(t)$ are zero-mean Gaussian processes with auto- and cross-correlation functions

$$\begin{aligned} E\{w_I(t)w_I(t+\tau)\} &= N_0 [g_I(\tau) \otimes g_I(-\tau)] \\ E\{w_Q(t)w_Q(t+\tau)\} &= \alpha^2 N_0 [g_Q(\tau) \otimes g_Q(-\tau)] \\ E\{w_I(t)w_Q(t+\tau)\} &= -\alpha N_0 \sin \psi [g_I(\tau) \otimes g_Q(-\tau)]. \end{aligned} \quad (4.5)$$

Inspection of (4.1) reveals that a DCR architecture affected by I/Q imbalance introduces self-image interference in the down-converted signal. Also, from (4.5) it is seen that $w(t)$ is not circularly symmetric as its real and imaginary components are generally cross-correlated and exhibit different auto-correlation functions.

4.2.2 Signal model

We consider an OFDM burst-mode communication where each block has length T and is preceded by a cyclic prefix (CP) to avoid inter-block interference (IBI). The subcarrier spacing is $1/T$ and the number of available subcarriers is N . As specified in many standards for wireless communications [9], [11], [48] a TP is appended in front of each data frame to facilitate the synchronization and channel estimation tasks. In particular, we assume that the TP has a periodic structure in the time-domain and is composed by $M \geq 2$ identical segments [25], [27]. The basic segment comprises P time-domain samples (with P being a power of two) and is generated by feeding a sequence of pilot symbols $\mathbf{c} = [c(0), c(1), \dots, c(P-1)]^T$ into a P -point inverse discrete Fourier transform (IDFT) unit. Hence, denoting by $s(k)$ the k th sample of the TP, we have

$$s(k) = \frac{1}{\sqrt{P}} \sum_{n=0}^{P-1} c(n) e^{j2\pi nk/P} \quad -N_g \leq k \leq MP \quad (4.6)$$

where N_g is the CP length normalized by the signaling period $T_s = T/N$.

After propagating through the multipath channel, the received signal $r_{RF}(t)$ is down-converted to baseband and sampled with period T_s using the DCR architecture of Fig. 4.1. Assuming that a coarse timing estimate is available at the receiver, samples belonging to the TP are extracted from the incoming stream and arranged into M vectors $\mathbf{x}_m = [x_m(0), x_m(1), \dots, x_m(P-1)]^T$ ($m = 0, 1, \dots, M-1$), where each vector has length P and corresponds to a specific TP segment. According to the baseband equivalent of Fig. 4.2, the p th entry of \mathbf{x}_m can be written as

$$x_m(p) = e^{j[m-(M-1)/2]\varphi} a(p) + e^{-j[m-(M-1)/2]\varphi} b(p) + w_m(p) \quad (4.7)$$

where $w_m(p)$ is the noise contribution and we have defined

$$\varphi = \frac{2\pi\nu}{Q} \quad (4.8)$$

with $Q = N/P$ and $\nu \triangleq \Delta f \cdot T$ being the CFO normalized by the subcarrier spacing. Furthermore, $a(p)$ and $b(p)$ are given by

$$a(p) = e^{j(M-1)\varphi/2} e^{j2\pi\nu p/N} [s(t) \otimes h(t)]_{t=pT_s} \quad (4.9)$$

$$b(p) = e^{-j(M-1)\varphi/2} e^{-j2\pi\nu p/N} [s^*(t) \otimes q(t)]_{t=pT_s} \quad (4.10)$$

where

$$s(t) = \frac{1}{\sqrt{P}} \sum_{n=0}^{P-1} c(n) e^{j2\pi n Q t / T} \quad (4.11)$$

is the transmitted TP. In writing (4.9) and (4.10), we have borne in mind that $[s(t) \otimes h(t)]_{t=pT_s+mPT_s} = [s(t) \otimes h(t)]_{t=pT_s}$ and $[s^*(t) \otimes q(t)]_{t=pT_s+mPT_s} = [s^*(t) \otimes q(t)]_{t=pT_s}$ due to the repetitive TP structure.

To proceed further, we consider the following M -dimensional vectors

$$\mathbf{x}(p) = [x_0(p), x_1(p), \dots, x_{M-1}(p)]^T \quad p = 0, 1, \dots, P-1 \quad (4.12)$$

where $\mathbf{x}(p)$ is obtained by collecting the p th entry of vectors \mathbf{x}_m for $m = 0, 1, \dots, M-1$. Hence, taking (4.7) into account, we get

$$\mathbf{x}(p) = \mathbf{u}(\varphi)a(p) + \mathbf{u}(-\varphi)b(p) + \mathbf{w}(p) \quad p = 0, 1, \dots, P-1 \quad (4.13)$$

where $\mathbf{w}(p) = [w_0(p), w_1(p), \dots, w_{M-1}(p)]^T$ is a complex-valued zero-mean Gaussian vector, and

$$\mathbf{u}(\varphi) = e^{-j(M-1)\varphi/2} [1, e^{j\varphi}, e^{j2\varphi}, \dots, e^{j(M-1)\varphi}]^T. \quad (4.14)$$

Inspection of (4.13) and (4.14) reveals that $\mathbf{x}(p)$ consists of two spectral lines $\mathbf{u}(\varphi)$ and $\mathbf{u}(-\varphi)$, symmetrically positioned around the origin and accounting for the direct signal and its mirror image, respectively. In the ensuing discussion, we investigate the ML estimation of the normalized CFO φ in the presence of the nuisance vectors $\mathbf{a} = [a(0), a(1), \dots, a(P-1)]^T$ and $\mathbf{b} = [b(0), b(1), \dots, b(P-1)]^T$. In doing so, we first review the CML estimator presented in [45], which assumes $\mathbf{b} = \mathbf{0}$, and evaluate its performance in the presence of I/Q imbalance. Next, we assess the accuracy of the JML algorithm proposed in [57], which jointly estimates $(\varphi, \mathbf{a}, \mathbf{b})$ without exploiting any side information about \mathbf{b} . On the other hand, since the signal component is typically much stronger than its mirror image (i.e., $\|\mathbf{a}\| \gg \|\mathbf{b}\|$), a novel ML estimator of $(\varphi, \mathbf{a}, \mathbf{b})$ is eventually derived by imposing a constraint on the ratio $\|\mathbf{a}\|^2/\|\mathbf{b}\|^2$.

To make the analysis mathematically tractable, we model the noise term $w(t)$ as a zero-mean circularly-symmetric Gaussian (ZMCSG) complex random process. This amounts to saying that $\{\mathbf{w}(p); p = 0, 1, \dots, P-1\}$ are considered as statistically independent ZMCSG vectors with covariance matrix $\mathbf{K}_w = \sigma_w^2 \mathbf{I}_M$. Numerical simulation will be used later to validate the theoretical results in a more realistic scenario characterized by the true noise statistics.

4.3 CFO estimation in the absence of I/Q imbalance

4.3.1 Estimator's design

The CML is suggested in [45] for an OFDM receiver without any RF imperfections. This scheme performs the joint ML estimation of (φ, \mathbf{a}) based on the following signal model

$$\mathbf{x}(p) = \mathbf{u}(\varphi)a(p) + \mathbf{w}(p) \quad p = 0, 1, \dots, P-1 \quad (4.15)$$

which is obtained from (4.13) by setting $b(p) = 0$. The log-likelihood function (LLF) is expressed by [4]

$$\Lambda(\tilde{\varphi}, \tilde{\mathbf{a}}) = -N \ln(\pi\sigma_w^2) - \frac{1}{\sigma_w^2} \sum_{p=0}^{P-1} \|\mathbf{x}(p) - \mathbf{u}(\tilde{\varphi})\tilde{a}(p)\|^2 \quad (4.16)$$

and its maximization with respect to $(\tilde{\varphi}, \tilde{\mathbf{a}})$ leads to the following CFO estimate

$$\hat{\varphi}_{CML} = \arg \max_{\tilde{\varphi} \in [-\pi, \pi)} \{\Psi_{CML}(\tilde{\varphi})\} \quad (4.17)$$

where

$$\Psi_{CML}(\tilde{\varphi}) = \sum_{p=0}^{P-1} \|\mathbf{u}^H(\tilde{\varphi})\mathbf{x}(p)\|^2. \quad (4.18)$$

Taking (4.12) and (4.14) into account, we may put the metric $\Psi_{CML}(\tilde{\varphi})$ in the equivalent form

$$\Psi_{CML}(\tilde{\varphi}) = \sum_{m=0}^{M-1} \sum_{k=0}^{M-1} \Re \{ \chi_{CML,m,k}(\tilde{\varphi}) \mathbf{x}_m^H \mathbf{x}_k \} \quad (4.19)$$

with $\chi_{CML,m,k}(\tilde{\varphi}) = e^{j(m-k)\tilde{\varphi}}$.

4.3.2 Performance analysis

Since the CML is derived under the simplifying assumption $\mathbf{b} = \mathbf{0}$, it is interesting to assess its accuracy in the presence of I/Q imbalance. For this purpose, we define the estimation error as $\varepsilon_{CML} = \hat{\varphi}_{CML} - \varphi$ and assume that the system operates at sufficiently large signal-to-noise ratio (SNR) values. Hence, following the approach outlined in [67], we get

$$\mathbb{E}\{\varepsilon_{CML}\} \simeq -\frac{\mathbb{E}\{\Psi'_{CML}(\varphi)\}}{\mathbb{E}\{\Psi''_{CML}(\varphi)\}} \quad (4.20)$$

$$\mathbb{E}\{\varepsilon_{CML}^2\} \simeq \frac{\mathbb{E}\{[\Psi'_{CML}(\varphi)]^2\}}{[\mathbb{E}\{\Psi''_{CML}(\varphi)\}]^2} \quad (4.21)$$

where $\Psi'_{CML}(\varphi)$ e $\Psi''_{CML}(\varphi)$ are the first and second order derivatives of $\Psi_{CML}(\tilde{\varphi})$, respectively, evaluated at $\tilde{\varphi} = \varphi$. In Appendix A it is shown that

$$\mathbb{E}\{\varepsilon_{CML}\} = \frac{6}{M^2 - 1} \cdot \frac{[\Re\{\mathbf{a}^H \mathbf{b}\} + q_M(\varphi)\|\mathbf{b}\|^2]q'_M(\varphi)}{\Omega_M(\varphi)} \quad (4.22)$$

with

$$q_M(\varphi) = \frac{\sin(M\varphi)}{M \sin \varphi} \quad (4.23)$$

$$\Omega_M(\varphi) = \|\mathbf{a}\|^2 + [q_M(\varphi) - \gamma_M(\varphi)]\Re\{\mathbf{a}^H \mathbf{b}\} - [\beta_M(\varphi) + q_M(\varphi)\gamma_M(\varphi)]\|\mathbf{b}\|^2. \quad (4.24)$$

In the above equation, the quantities $\beta_M(\varphi)$ and $\gamma_M(\varphi)$ are expressed by

$$\beta_M(\varphi) = \frac{3}{M^2 - 1}[q'_M(\varphi)]^2 \quad \text{and} \quad \gamma_M(\varphi) = \frac{3}{M^2 - 1}q''_M(\varphi) \quad (4.25)$$

where $q'_M(\varphi)$ and $q''_M(\varphi)$ are the first and second order derivatives of $q_M(\varphi)$, respectively. Inspection of (4.22) and (4.24) indicates that, in general, $\hat{\varphi}_{CML}$ is a biased estimate of φ . The only exceptions occur in the absence of I/Q imbalance (i.e., $\mathbf{b} = \mathbf{0}$) or when $\varphi = 0$, since in the latter case we have $q'_M(\varphi) = 0$.

In Appendix A we also evaluate the mean square estimation error (MSEE) of $\hat{\varphi}_{CML}$, which is found to be

$$\mathbb{E}\{\varepsilon_{CML}^2\} = \mathbb{E}^2\{\varepsilon_{CML}\} + \frac{6\sigma_w^2}{M(M^2 - 1)} \cdot \frac{A_M(\varphi)}{\Omega_M^2(\varphi)} + \frac{6P\sigma_w^4}{M^2(M^2 - 1)} \cdot \frac{1}{\Omega_M^2(\varphi)} \quad (4.26)$$

with

$$A_M(\varphi) = \|\mathbf{a}\|^2 + 2q_M(\varphi)\Re\{\mathbf{a}^H \mathbf{b}\} + [\beta_M(\varphi) + q_M^2(\varphi)]\|\mathbf{b}\|^2. \quad (4.27)$$

4.3.3 Remarks

i) Observing that $q_M(0) = 1$, $\beta_M(0) = 0$ and $\gamma_M(0) = -1$, for $\varphi = 0$ we get $A_M(0) = \Omega_M(0) = \|\mathbf{a} + \mathbf{b}\|^2$ and (4.26) reduces to

$$\mathbb{E}\{\varepsilon_{CML}^2\}|_{\varphi=0} = \frac{6\sigma_w^2}{M(M^2 - 1)\|\mathbf{a} + \mathbf{b}\|^2} \left[1 + \frac{P\sigma_w^2}{M\|\mathbf{a} + \mathbf{b}\|^2} \right]. \quad (4.28)$$

ii) In the absence of I/Q imbalance we have $A_M(\varphi) = \Omega_M(\varphi) = \|\mathbf{a}\|^2$. In such a case, (4.26) becomes independent of φ and takes the form

$$\mathbb{E}\{\varepsilon_{CML}^2\}|_{\mathbf{b}=\mathbf{0}} = \frac{6\sigma_w^2}{M(M^2 - 1)\|\mathbf{a}\|^2} \left(1 + \frac{P\sigma_w^2}{M\|\mathbf{a}\|^2} \right) \quad (4.29)$$

which further simplifies to

$$\mathbb{E}\{\varepsilon_{CML}^2\} \big|_{\mathbf{b}=\mathbf{0}, \|\mathbf{a}\|^2/\sigma_w^2 \rightarrow \infty} = \frac{6\sigma_w^2}{M(M^2-1)\|\mathbf{a}\|^2} \quad (4.30)$$

at relatively high SNR values (i.e., $\|\mathbf{a}\|^2/\sigma_w^2 \rightarrow \infty$). It is worth noting that the right-hand side of (4.30) is the CRB for CFO estimation reported in [45]. This means that CML is asymptotically efficient when $\mathbf{b} = \mathbf{0}$, which can be justified by observing that $\hat{\varphi}_{CML}$ is the ML estimator of φ in the absence of any I/Q imbalance.

4.4 Joint ML estimation of the unknown parameters

4.4.1 Estimator's design

In this section we review the JML presented in [57], which aims at jointly estimating the unknown parameters $(\varphi, \mathbf{a}, \mathbf{b})$. After rewriting (4.13) as

$$\mathbf{x}(p) = \mathbf{A}_2(\varphi)\boldsymbol{\theta}(p) + \mathbf{w}(p) \quad p = 0, 1, \dots, P-1 \quad (4.31)$$

with $\mathbf{A}_2(\varphi) = [\mathbf{u}(\varphi) \ \mathbf{u}(-\varphi)]$ and $\boldsymbol{\theta}(p) = [a(p) \ b(p)]^T$, the LLF takes the form

$$\Lambda_2(\tilde{\varphi}, \tilde{\boldsymbol{\theta}}) = -N \ln(\pi\sigma_w^2) - \frac{1}{\sigma_w^2} \sum_{p=0}^{P-1} \left\| \mathbf{x}(p) - \mathbf{A}_2(\tilde{\varphi})\tilde{\boldsymbol{\theta}}(p) \right\|^2 \quad (4.32)$$

where $\tilde{\boldsymbol{\theta}}(p) \triangleq [\tilde{a}(p) \ \tilde{b}(p)]^T$ and $\tilde{\boldsymbol{\theta}} = \{\tilde{\boldsymbol{\theta}}(0), \tilde{\boldsymbol{\theta}}(1), \dots, \tilde{\boldsymbol{\theta}}(P-1)\}$. The maximum of the LLF with respect to $\tilde{\boldsymbol{\theta}}(p)$ is attained at

$$\hat{\boldsymbol{\theta}}(p; \tilde{\varphi}) = [\mathbf{A}_2^H(\tilde{\varphi})\mathbf{A}_2(\tilde{\varphi})]^{-1} \mathbf{A}_2^H(\tilde{\varphi})\mathbf{x}(p) \quad (4.33)$$

which is next substituted into (4.32) in place of $\tilde{\boldsymbol{\theta}}(p)$, yielding the concentrated likelihood function

$$\Lambda_2(\tilde{\varphi}) = -N \ln(\pi\sigma_w^2) - \frac{1}{\sigma_w^2} \sum_{p=0}^{P-1} \mathbf{x}^H(p) [\mathbf{I}_M - \mathbf{C}_2(\tilde{\varphi})] \mathbf{B}_2(\tilde{\varphi}) \mathbf{x}(p) \quad (4.34)$$

with $\mathbf{C}_2(\tilde{\varphi}) = \mathbf{A}_2(\tilde{\varphi})[\mathbf{A}_2^H(\tilde{\varphi})\mathbf{A}_2(\tilde{\varphi})]^{-1} \mathbf{A}_2^H(\tilde{\varphi})$. The ML estimate of φ is eventually given by

$$\hat{\varphi}_{JML} = \arg \max_{\tilde{\varphi} \in [-\pi, \pi)} \{\Psi_{JML}(\tilde{\varphi})\} \quad (4.35)$$

where

$$\Psi_{JML}(\tilde{\varphi}) = M \sum_{p=0}^{P-1} \mathbf{x}^H(p) \mathbf{C}_2(\tilde{\varphi}) \mathbf{x}(p). \quad (4.36)$$

After some manipulations, it is found that the metric $\Psi_{JML}(\tilde{\varphi})$ can also be written as

$$\Psi_{JML}(\tilde{\varphi}) = \sum_{m=0}^{M-1} \sum_{k=0}^{M-1} \Re \{ \chi_{JML,m,k}(\tilde{\varphi}) \mathbf{x}_m^H \mathbf{x}_k \} \quad (4.37)$$

where

$$\chi_{JML,m,k}(\tilde{\varphi}) = \frac{\cos[(m-k)\tilde{\varphi}] - q_M(\tilde{\varphi}) \cos[(m+k-M+1)\tilde{\varphi}]}{1 - q_M^2(\tilde{\varphi})} \quad (4.38)$$

and $q_M(\tilde{\varphi})$ has been defined in (4.23).

It is worth noting that letting $M = 2$ yields $\mathbf{C}_2(\tilde{\varphi}) = \mathbf{I}_2$, which makes $\Psi_{JML}(\tilde{\varphi})$ independent of $\tilde{\varphi}$. This amounts to saying that application of JML is possible only for $M \geq 3$. Furthermore, since $\Psi_{JML}(\tilde{\varphi})$ is an even function of $\tilde{\varphi}$, it exhibits two global maxima symmetrically positioned around $\tilde{\varphi} = 0$. This results into an ambiguity in the sign of $\hat{\varphi}_{JML}$ which cannot be removed unless additional information is available. One possible solution relies on the fact that the useful signal component is typically much stronger than its mirror image. In such a case, we suggest to consider the positive solution of (4.35), say $\hat{\varphi}_{JML}^+$, and compute the estimates $\hat{\mathbf{a}}$ and $\hat{\mathbf{b}}$ from (4.33) after replacing $\tilde{\varphi}$ with $\hat{\varphi}_{JML}^+$. Then, we set $\hat{\varphi}_{JML} = \hat{\varphi}_{JML}^+$ if $\|\hat{\mathbf{a}}\| > \|\hat{\mathbf{b}}\|$, otherwise we choose $\hat{\varphi}_{JML} = -\hat{\varphi}_{JML}^+$.

4.4.2 Performance analysis

The accuracy of $\hat{\varphi}_{JML}$ is assessed by applying the same methods used for the CML. Skipping the details, it is found that $E\{\hat{\varphi}_{JML}\} = \varphi$, thereby indicating that JML is unbiased. Furthermore, denoting by $\varepsilon_{JML} = \hat{\varphi}_{JML} - \varphi$ the estimation error, the MSEE turns out to be

$$\begin{aligned} E\{\varepsilon_{JML}^2\} &= \frac{6\sigma_w^2}{M(M^2-1)} \cdot \frac{1}{\left[\Gamma_{M,1}(\varphi) \left(\|\mathbf{a}\|^2 + \|\mathbf{b}\|^2 \right) + 2\Gamma_{M,2}(\varphi) \Re\{\mathbf{a}^H \mathbf{b}\} \right]} \\ &+ \frac{12P\sigma_w^4}{M^2(M^2-1)} \cdot \frac{\Gamma_{M,3}(\varphi)}{\left[\Gamma_{M,1}(\varphi) \left(\|\mathbf{a}\|^2 + \|\mathbf{b}\|^2 \right) + 2\Gamma_{M,2}(\varphi) \Re\{\mathbf{a}^H \mathbf{b}\} \right]^2} \end{aligned} \quad (4.39)$$

where

$$\Gamma_{M,1}(\varphi) = 1 - \frac{\beta_M(\varphi)}{1 - q_M^2(\varphi)} \quad (4.40)$$

$$\Gamma_{M,2}(\varphi) = \gamma_M(\varphi) + \frac{\beta_M(\varphi)q_M(\varphi)}{1 - q_M^2(\varphi)} \quad (4.41)$$

and

$$\Gamma_{M,3}(\varphi) = \frac{1}{1 - q_M^2(\varphi)} [\Gamma_{M,1}(\varphi) - q_M(\varphi)\Gamma_{M,2}(\varphi)] \quad (4.42)$$

with $\beta_M(\varphi)$ and $\gamma_M(\varphi)$ as defined in (4.25).

4.4.3 Remarks

i) For $M = 2$ we have $\Gamma_{M,1}(\varphi) = \Gamma_{M,2}(\varphi) = 0$ and the denominator in (4.39) vanishes. Such a result confirms the fact that φ cannot be estimated when $M < 3$.

ii) Using the fourth-order Maclaurin series of $q_M(\varphi)$

$$q_M(\varphi) \simeq 1 - \frac{M^2 - 1}{6}\varphi^2 + \frac{(M^2 - 1)(3M^2 - 7)}{360}\varphi^4 \quad (4.43)$$

it is found that, for small values of φ , functions $\Gamma_{M,i}(\varphi)$ ($i = 1, 2$) can be approximated as

$$\Gamma_{M,i}(\varphi) \simeq \frac{M^2 - 4}{15}\varphi^2 \quad i = 1, 2 \quad (4.44)$$

while $\Gamma_{M,3}(\varphi) \simeq \Gamma_{M,1}(\varphi)/2$. Substituting these results into (4.39) produces

$$\mathbb{E}\{\varepsilon_{JML}^2\}|_{\varphi \rightarrow 0} \simeq \frac{90\sigma_w^2}{M(M^2 - 1)(M^2 - 4)\|\mathbf{a} + \mathbf{b}\|^2} \left(1 + \frac{P\sigma_w^2}{M\|\mathbf{a} + \mathbf{b}\|^2}\right) \cdot \frac{1}{\varphi^2} \quad (4.45)$$

which indicates that the accuracy of JML rapidly degrades as φ approaches zero. The reason is that in such a case the two spectral lines in (4.13) tend to overlap in the frequency domain, until they collapse into a single dc component when $\varphi = 0$, thereby preventing the joint estimation of \mathbf{a} and \mathbf{b} .

iii) In the absence of any I/Q imbalance we have $\mathbf{b} = \mathbf{0}$ and (4.39) takes the form

$$\mathbb{E}\{\varepsilon_{JML}^2\}|_{\mathbf{b}=\mathbf{0}} = \frac{6\sigma_w^2}{M(M^2 - 1)\|\mathbf{a}\|^2} \cdot \frac{1}{\Gamma_{M,1}(\varphi)} + \frac{12P\sigma_w^4}{M^2(M^2 - 1)\|\mathbf{a}\|^4} \cdot \frac{\Gamma_{M,3}(\varphi)}{\Gamma_{M,1}^2(\varphi)} \quad (4.46)$$

which, at relatively large SNR values, reduces to

$$\mathbb{E}\{\varepsilon_{JML}^2\}|_{\mathbf{b}=\mathbf{0}, \|\mathbf{a}\|^2/\sigma_w^2 \rightarrow \infty} = \frac{6\sigma_w^2}{M(M^2 - 1)\|\mathbf{a}\|^2} \cdot \frac{1}{\Gamma_{M,1}(\varphi)}. \quad (4.47)$$

Comparing (4.30) with (4.47) and recalling that $0 \leq \Gamma_{M,1}(\varphi) \leq 1$, it turns out that in a perfectly balanced receiver the CML outperforms (at least asymptotically) the JML. This result is not surprising since, in the considered scenario, $\hat{\varphi}_{CML}$ is the ML estimate of φ .

4.5 Constrained joint ML estimation of the unknown parameters

4.5.1 Estimator's design

As mentioned previously, the JML is derived in [57] without considering the fact that in a practical situation we have $\|\mathbf{a}\| \gg \|\mathbf{b}\|$. We now illustrate how such a side information can be exploited to solve the sign ambiguity of $\hat{\varphi}_{JML}$. Our approach aims at maximizing (4.32) subject to a constraint on the SIR. The resulting scheme is referred to as the constrained JML (CJML) and solves the following problem

$$\begin{aligned} \min_{\tilde{\varphi}, \tilde{\boldsymbol{\theta}}} \quad & \sum_{p=0}^{P-1} \left\| \mathbf{x}(p) - \mathbf{A}_2(\tilde{\varphi}) \tilde{\boldsymbol{\theta}}(p) \right\|^2 \\ \text{s.t.} \quad & \|\tilde{\mathbf{b}}\|^2 \leq \delta \|\tilde{\mathbf{a}}\|^2 \end{aligned} \quad (4.48)$$

where $\delta > 0$ is a design parameter. In Appendix B it is shown that CJML takes the form

$$\hat{\varphi}_{CJML} = \arg \max_{\tilde{\varphi} \in [-\pi, \pi)} \{ \Psi_{CJML}(\tilde{\varphi}) \} \quad (4.49)$$

where the metric $\Psi_{CJML}(\tilde{\varphi})$ is found to be

$$\Psi_{CJML}(\tilde{\varphi}) = \sum_{m=0}^{M-1} \sum_{k=0}^{M-1} \chi_{CJML,m,k}(\tilde{\varphi}) \mathbf{x}_m^H \mathbf{x}_k \quad (4.50)$$

with

$$\begin{aligned} \chi_{CJML,m,k}(\tilde{\varphi}) = & \{ 2\zeta_1(\tilde{\varphi}) - M[\zeta_1^2(\tilde{\varphi}) - 2q_M(\tilde{\varphi})\zeta_1(\tilde{\varphi})\zeta_2(\tilde{\varphi}) + \zeta_2^2(\tilde{\varphi})] \} e^{j(m-k)\tilde{\varphi}} \\ & + \{ 2\zeta_3(\tilde{\varphi}) - M[\zeta_3^2(\tilde{\varphi}) - 2q_M(\tilde{\varphi})\zeta_2(\tilde{\varphi})\zeta_3(\tilde{\varphi}) + \zeta_2^2(\tilde{\varphi})] \} e^{-j(m-k)\tilde{\varphi}} \\ & + 2\{ M[\zeta_1(\tilde{\varphi}) + \zeta_3(\tilde{\varphi})]\zeta_2(\tilde{\varphi}) - Mq_M(\tilde{\varphi})[\zeta_1(\tilde{\varphi})\zeta_3(\tilde{\varphi}) + \zeta_2^2(\tilde{\varphi})] - \\ & \quad 2\zeta_2(\tilde{\varphi}) \} \cos[(m+k-M+1)\tilde{\varphi}]. \end{aligned} \quad (4.51)$$

In the above equation, functions $\zeta_1(\tilde{\varphi})$, $\zeta_2(\tilde{\varphi})$ and $\zeta_3(\tilde{\varphi})$ depend on δ and are expressed by

$$\zeta_1(\tilde{\varphi}) = [M + \lambda(\tilde{\varphi})]/D(\tilde{\varphi}) \quad (4.52)$$

$$\zeta_2(\tilde{\varphi}) = Mq_M(\tilde{\varphi})/D(\tilde{\varphi}) \quad (4.53)$$

$$\zeta_3(\tilde{\varphi}) = [M - \delta\lambda(\tilde{\varphi})]/D(\tilde{\varphi}) \quad (4.54)$$

with $D(\tilde{\varphi}) = [M + \lambda(\tilde{\varphi})][M - \delta\lambda(\tilde{\varphi})] - M^2q_M^2(\tilde{\varphi})$ and

$$\lambda(\tilde{\varphi}) = \max \left(0, \frac{\Upsilon_2(\tilde{\varphi}) - \sqrt{\Upsilon_2^2(\tilde{\varphi}) - \Upsilon_1(\tilde{\varphi})\Upsilon_3(\tilde{\varphi})}}{\Upsilon_1(\tilde{\varphi})} \right). \quad (4.55)$$

Furthermore, we have

$$\Upsilon_1(\tilde{\varphi}) = \delta (\delta \|\mathbf{t}_2(\tilde{\varphi})\|^2 - \|\mathbf{t}_1(\tilde{\varphi})\|^2) \quad (4.56)$$

$$\Upsilon_2(\tilde{\varphi}) = M\delta [\|\mathbf{t}_1(\tilde{\varphi})\|^2 + \|\mathbf{t}_2(\tilde{\varphi})\|^2 - 2q_M(\tilde{\varphi})\Re\{\mathbf{t}_1^H(\tilde{\varphi})\mathbf{t}_2(\tilde{\varphi})\}] \quad (4.57)$$

$$\begin{aligned} \Upsilon_3(\tilde{\varphi}) = \\ M^2 \{ [q_M^2(\tilde{\varphi}) - \delta] \|\mathbf{t}_1(\tilde{\varphi})\|^2 - 2q_M(\tilde{\varphi})(1 - \delta)\Re\{\mathbf{t}_1^H(\tilde{\varphi})\mathbf{t}_2(\tilde{\varphi})\} + [1 - \delta q_M^2(\tilde{\varphi})] \|\mathbf{t}_2(\tilde{\varphi})\|^2 \} \end{aligned} \quad (4.58)$$

where \mathbf{t}_1 and \mathbf{t}_2 are P -dimensional vectors with entries $[\mathbf{t}_1(\tilde{\varphi})]_p = \mathbf{u}^H(\tilde{\varphi})\mathbf{x}(p)$ and $[\mathbf{t}_2(\tilde{\varphi})]_p = \mathbf{u}^H(-\tilde{\varphi})\mathbf{x}(p)$ for $p = 0, 1, \dots, P-1$.

Unfortunately, evaluating the theoretical performance of CJML is extremely challenging and all our attempts to accomplish this task encountered impassable barriers. For this reason, the accuracy of CJML will be assessed by only resorting to numerical simulations.

4.5.2 Remarks

i) When δ approaches zero, we have $\lim_{\delta \rightarrow 0} \lambda(\tilde{\varphi}) = +\infty$ and $\lim_{\delta \rightarrow 0} \delta\lambda(\tilde{\varphi}) = 0$. Hence, from (4.52)–(4.54) it is found that $\zeta_1(\tilde{\varphi})$ approaches $1/M$, while $\zeta_2(\tilde{\varphi})$ and $\zeta_3(\tilde{\varphi})$ become vanishingly small. These results lead to

$$\lim_{\delta \rightarrow 0} \chi_{CJML,m,k}(\tilde{\varphi}) = \frac{1}{M} e^{j(m-k)\tilde{\varphi}} = \frac{1}{M} \chi_{CML,m,k}(\tilde{\varphi}) \quad (4.59)$$

which indicates that CJML reduces to CML. The reason is that letting $\delta = 0$ in the constraint $\|\mathbf{b}\|^2 \leq \delta \|\mathbf{a}\|^2$ amounts to putting $\mathbf{b} = \mathbf{0}$, which is just the main assumption behind the CML.

i) When δ goes to infinity, we have $\lim_{\delta \rightarrow +\infty} \lambda(\tilde{\varphi}) = \lim_{\delta \rightarrow +\infty} \delta \lambda(\tilde{\varphi}) = 0$ leading to

$$\lim_{\delta \rightarrow +\infty} \zeta_1(\tilde{\varphi}) = \lim_{\delta \rightarrow +\infty} \zeta_3(\tilde{\varphi}) = \frac{1}{M[1 - q_M^2(\tilde{\varphi})]} \quad \lim_{\delta \rightarrow +\infty} \zeta_2(\tilde{\varphi}) = \frac{q_M(\tilde{\varphi})}{M[1 - q_M^2(\tilde{\varphi})]}. \quad (4.60)$$

In such a case it is found that

$$\lim_{\delta \rightarrow +\infty} \chi_{CJML,m,k}(\tilde{\varphi}) = \frac{2}{M} \cdot \frac{\cos[(m-k)\tilde{\varphi}] - q_M(\tilde{\varphi}) \cos[(m+k-M+1)\tilde{\varphi}]}{1 - q_M^2(\tilde{\varphi})} \quad (4.61)$$

which, compared with (4.38), reveals that CJML reduces to JML. This fact can be explained by observing that letting $\delta \rightarrow +\infty$ amounts to removing any constraint on the magnitude of \mathbf{b} .

The above remarks indicate that CJML is a quite general ML-based estimator which incorporates both CML and JML as special cases when $\delta \rightarrow 0$ and $\delta \rightarrow +\infty$, respectively.

4.6 CRB analysis

It is interesting to compare the performance of the ML-based estimation algorithms illustrated in the previous section with the relevant CRB. The latter is computed from the signal model (4.31) using the *true* statistical distribution of $w_I(t)$ and $w_Q(t)$, whose auto- and cross-correlation functions are given in (4.5). For this purpose, we arrange the samples $x_m(p) = x_m^I(p) + jx_m^Q(p)$ into a real-valued vector $\mathbf{x} = [x_0^I(0), x_0^Q(0), x_0^I(1), x_0^Q(1) \cdots x_{M-1}^I(P-1), x_{M-1}^Q(P-1)]^T$ with $2PM$ entries. Then, bearing in mind (4.7), we can write

$$\mathbf{x} = \boldsymbol{\eta} + \mathbf{w} \quad (4.62)$$

where $\mathbf{w} = [w_0^I(0), w_0^Q(0), w_0^I(1), w_0^Q(1) \cdots w_{M-1}^I(P-1), w_{M-1}^Q(P-1)]^T$ is the noise contribution, with $w_m^I(p)$ and $w_m^Q(p)$ being the real and imaginary parts of $w_m(p)$, respectively. Furthermore, letting $a(p) = a^I(p) + ja^Q(p)$ and $b(p) = b^I(p) + jb^Q(p)$, we have

$$\boldsymbol{\eta} = \mathbf{Q}\mathbf{z} \quad (4.63)$$

with $\mathbf{z} = [\mathbf{z}^T(0) \mathbf{z}^T(1) \cdots \mathbf{z}^T(P-1)]^T$ and $\mathbf{z}(p) = [a^I(p), a^Q(p), b^I(p), b^Q(p)]^T$, while \mathbf{Q} is a matrix of dimension $2PM \times 4P$ with the following structure

$$\mathbf{Q} = \begin{bmatrix} \mathbf{Q}_0^T & \mathbf{Q}_1^T & \cdots & \mathbf{Q}_{M-1}^T \end{bmatrix}^T. \quad (4.64)$$

In the above equation, \mathbf{Q}_m ($m = 0, 1, \dots, M-1$) is a $2P \times 4P$ matrix

$$\mathbf{Q}_m = \text{diag}\{\underbrace{\mathbf{R}_m, \mathbf{R}_m, \dots, \mathbf{R}_m}_P\} \quad (4.65)$$

where \mathbf{R}_m is defined as

$$\mathbf{R}_m = \begin{bmatrix} c_m(\varphi) & -s_m(\varphi) & c_m(\varphi) & s_m(\varphi) \\ s_m(\varphi) & c_m(\varphi) & -s_m(\varphi) & c_m(\varphi) \end{bmatrix} \quad (4.66)$$

with $c_m(\varphi)$ and $s_m(\varphi)$ being a shorthand notation for $\cos[(m - \frac{M-1}{2})\varphi]$ and $\sin[(m - \frac{M-1}{2})\varphi]$, respectively. For notational simplicity, in (4.64) we have omitted the dependence of \mathbf{Q} on φ .

In Appendix C it is shown that

$$\text{CRB}(\varphi) = \frac{1}{\mathbf{z}^T \dot{\mathbf{Q}}^T [\mathbf{C}_w^{-1} - \mathbf{C}_w^{-1} \mathbf{Q} (\mathbf{Q}^T \mathbf{C}_w^{-1} \mathbf{Q})^{-1} \mathbf{Q}^T \mathbf{C}_w^{-1}] \dot{\mathbf{Q}} \mathbf{z}} \quad (4.67)$$

where \mathbf{C}_w is the correlation matrix of \mathbf{w} and $\dot{\mathbf{Q}}$ is the derivative of \mathbf{Q} with respect to φ . Unfortunately, such expression does not provide any indication about the impact of the various design parameters on the estimation accuracy. A more useful expression is obtained by assuming a white-noise scenario wherein $\mathbf{C}_w = (\sigma_w^2/2)\mathbf{I}_{2PM}$. In such a case, after lengthy computations it is found that (4.67) takes the form

$$\text{CRB}(\varphi) = \frac{6\sigma_w^2}{M(M^2 - 1)} \cdot \frac{1}{\left[\Gamma_{M,1}(\varphi) (\|\mathbf{a}\|^2 + \|\mathbf{b}\|^2) + 2\Gamma_{M,2}(\varphi) \Re\{\mathbf{a}^H \mathbf{b}\} \right]} \quad (4.68)$$

with $\Gamma_{M,1}(\varphi)$ and $\Gamma_{M,2}(\varphi)$ defined as in (4.40)-(4.41). It is worth noting that, at relatively high SNR values, the accuracy of $\hat{\varphi}_{JML}$ given in (4.39) approaches the CRB in (4.68), meaning that JML is asymptotically efficient in the presence of AWGN. This is a consequence of the fact that in such scenario $\hat{\varphi}_{JML}$ is the ML estimator of $(\varphi, \mathbf{a}, \mathbf{b})$.

4.7 Simulation results

4.7.1 Simulation model

The investigated OFDM system is compliant with the IEEE 802.11a standard for WLANs [48]. Specifically, the DFT size is $N = 64$ with a signaling interval $T_s = 50$ ns, which corresponds to a subcarrier distance of $1/T = 312.5$ kHz during the frame payload. The TP is composed by ten repeated segments, each carrying $P = 16$ samples. By considering the first two segments as the CP of the TP, the remaining $M = 8$ segments are exploited for CFO recovery. We adopt a discrete-time channel model and collect the T_s -spaced samples of $v(t)$ into a vector $\mathbf{v} = [v(0), v(1), \dots, v(L_v - 1)]^T$ of dimension L_v . The entries of \mathbf{v} are modeled as independent and circularly symmetric Gaussian random variables with zero-mean and an exponentially decaying power delay profile

$$\mathbb{E}\{|v(k)|^2\} = \sigma_v^2 \exp(-k/L_v) \quad k = 0, 1, \dots, L_v - 1 \quad (4.69)$$

where σ_v^2 is chosen such that $\mathbb{E}\{\|\mathbf{v}\|^2\} = 1$. As in [57], we consider the following two scenarios.

Case A) *Severe I/Q imbalance*: in this case both frequency independent and frequency selective RF imperfections are present. The analog I/Q filters have discrete-time impulse responses $\mathbf{g}_I = [0, 1, \mu]^T$ and $\mathbf{g}_Q = [\mu, 1, 0]^T$ with $\mu = 0.1$, while the LO-induced imbalance is characterized by $\alpha = 1$ dB and $\psi = 5^\circ$. From (4.2), it follows that $h(k)$ and $q(k)$ have support $k = 0, 1, \dots, L - 1$, with $L = L_v + 2$.

Case B) *Moderate I/Q imbalance*: in this case only frequency independent imbalance is considered with $\alpha = 1$ dB and $\psi = 5^\circ$, while the I/Q filters have ideal responses $\mathbf{g}_I = \mathbf{g}_Q = [0, 1, 0]^T$.

In both scenarios, the average SIR is defined as σ_a^2/σ_b^2 and is found to be [57]

$$\text{SIR} = \frac{\sum_{p=0}^{L-1} \mathbb{E}\{|h(p)|^2\}}{\sum_{p=0}^{L-1} \mathbb{E}\{|q(p)|^2\}}. \quad (4.70)$$

Since the entries of \mathbf{v} are statistically independent with zero mean and average power (4.69), from (4.2) and (4.3) we can express the SIR as a function of the imbalance parameters as

$$\text{SIR} = \frac{1 + \alpha^2 + 2\alpha \cos \psi + \mu^2 + \mu^2 \alpha^2}{1 + \alpha^2 - 2\alpha \cos \psi + \mu^2 + \mu^2 \alpha^2} \quad (4.71)$$

yielding the values of 19.9 dB and 22.8 dB for Case A and Case B, respectively.

The accuracy of the investigated schemes is assessed in terms of their MSEE. Assuming a carrier frequency of 5 GHz and an oscillator instability of ± 30 parts-per-million (ppm), the maximum value of the normalized CFO is approximately given by $\nu_{\max} = 0.5$. Hence, recalling that $Q = N/P = 4$, from (4.8) it follows that $\varphi \in (-\pi/4, \pi/4)$. The global maximum of the CFO metrics shown in (4.19), (4.37) and (4.50) is sought in two steps. The first one (coarse search) evaluates the metric over a grid of K uniformly-spaced values $\mathcal{F} = \{\tilde{\varphi}_k = -\pi/4 + k\pi/(2K); k = 0, 1, \dots, K\}$ and determines the location $\tilde{\varphi}_M$ of the maximum. The second step (fine search) makes a parabolic interpolation between the metric values and computes the local maximum nearest to $\tilde{\varphi}_M$. Parameter K has been selected by means of numerical simulations and it was found that $K = 128$ provides nearly optimal performance.

4.7.2 Performance assessment for FO estimation

An important design parameter for the implementation of CJML is the coefficient δ , which specifies the constraint on the SIR level $\|\mathbf{a}\|^2/\|\mathbf{b}\|^2$. Figure 4.3 shows the accuracy of CJML as a function of δ (expressed in dB) for different SNR values. These results are obtained in the severe I/Q imbalance scenario, and are qualitatively similar to those pertaining to the moderate I/Q scenario. As is seen, at intermediate and low SNR values the MSEE monotonically increases with δ , while at large SNR values a global minimum is achieved around $\delta = -22$ dB. From these measurements it turns out that setting $\delta = -24$ dB provides satisfactory performance in all practical situations. For this reason, such a value is used for CJML in all subsequent simulations. Figures 4.4 and 4.5 illustrate the MSEE of the CFO estimators as a function of φ measured at SNR = 15 dB. More precisely, we investigate the severe I/Q scenario in Fig. 4.4, while the moderate I/Q case is assumed in Fig. 4.5. For all the considered schemes, marks indicate simulation results. The solid line illustrates theoretical analysis for CML and JML, while for CJML it is only used to facilitate the reading of the plot. The CRB reported in (4.68) is also shown for comparison. As expected, JML performs poorly for small CFO values since in this case the useful signal component and its mirror image collapse into a single dc line and cannot be easily resolved. This is also reflected by the CRB curve, which goes to infinity as φ approaches zero. In contrast, the accuracy of both CML and JCML depends weakly

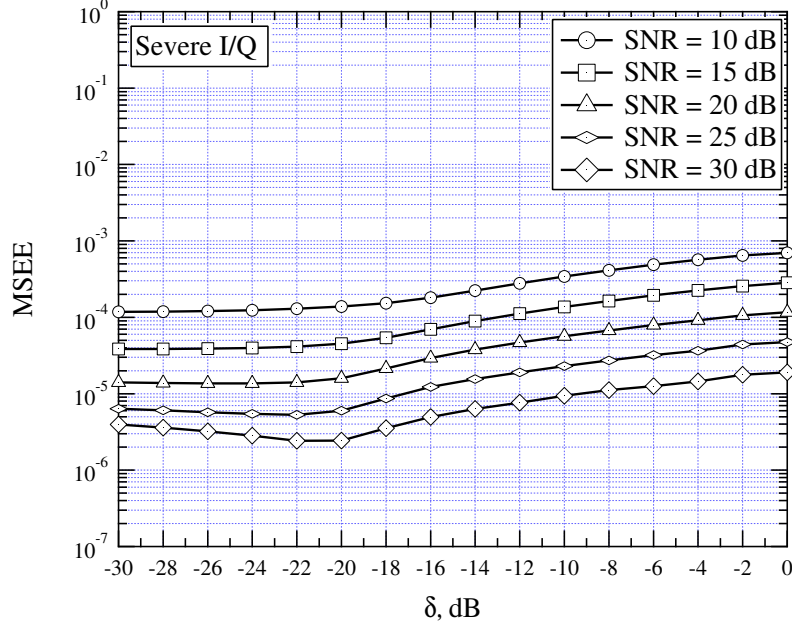


Figure 4.3: Accuracy of CJML vs δ for different SNR values in the severe I/Q imbalance scenario.

on the CFO value and is remarkably better than that of JML for $|\varphi| < 0.1\pi$. Although CML and CJML perform similarly at all considered CFO values, the former scheme is marginally better than the latter for $\varphi = 0$. The reason is that in this specific situation the received signal in (4.13) reduces to a dc line embedded in (approximately) white Gaussian noise and, due to the absence of any mirror interference, CML provides nearly optimum performance. It is worth noting that the theoretical analysis of CML and JML (derived under the white noise assumption) is in good agreement with simulation results (obtained using the true noise statistics) except when we consider JML at small CFO values. The discrepancy observed in the latter case is essentially due to the fact that the MSEE shown in (4.39) is derived using the approach outlined in [67], which is valid only for relatively small estimation errors. Surprisingly, at low CFO values the MSEE of JML is smaller than the relevant CRB. The reason is that in these circumstances JML provides biased estimates and the CRB theory cannot be applied anymore.

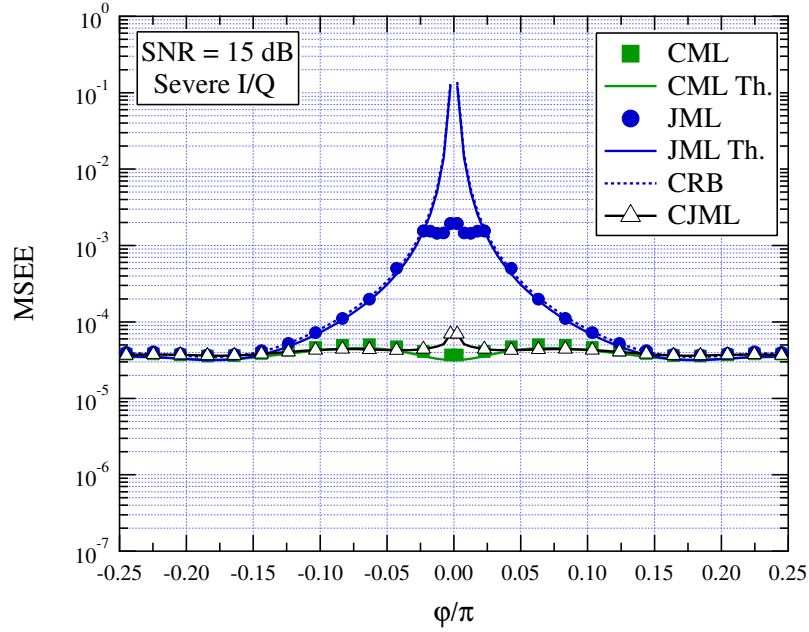


Figure 4.4: Accuracy of the CFO estimators vs ϕ in the severe I/Q imbalance scenario with SNR = 15 dB.

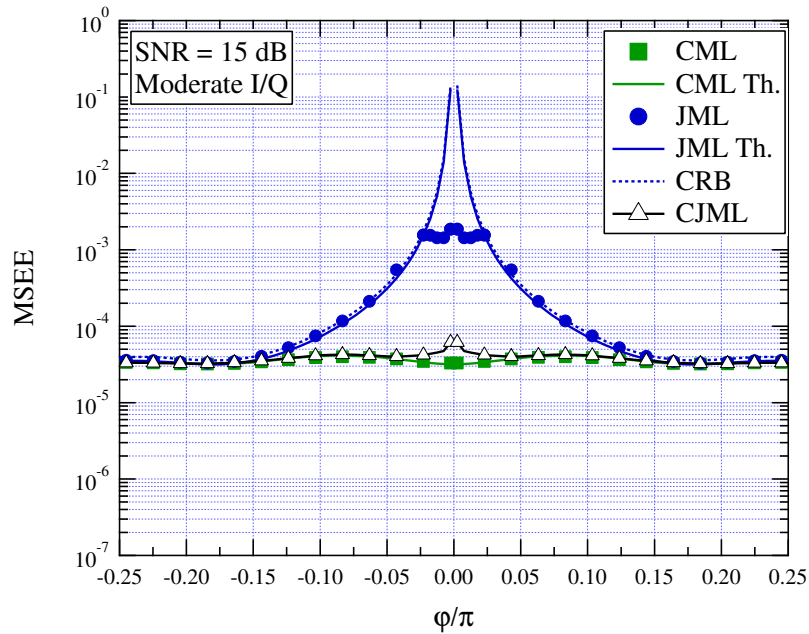


Figure 4.5: Accuracy of the CFO estimators vs ϕ in the moderate I/Q imbalance scenario with SNR = 15 dB.

For higher CFO values, JML becomes unbiased and its accuracy approaches the CRB, meaning that it is an efficient estimator. It is also worth recalling that in both the severe and moderate imbalance cases, no tangible difference is observed between the true CRB (4.67) and its approximation (4.68), thereby justifying the adoption of the white noise assumption in all practical scenarios. The results shown in Figs. 4.6 and 4.7 are obtained under the same operating conditions of Figs. 4.4 and 4.5, respectively, except that the SNR is now set to 30 dB. In this case, we see that CML outperforms JML only when $|\varphi|$ is approximately smaller than 0.05π . Such behavior is justified by the fact that at large SNR values the MSEE of JML becomes proportional to $(\text{SNR})^{-1}$, while the accuracy of CML is essentially determined by the bias term $E^2\{\varepsilon_{CML}\}$ present in (4.26), which vanishes only for specific values of φ . As for CJML, it provides better estimates than CML except in the proximity of $\varphi = 0$. Compared to JML, it performs similarly or slightly worsen when $|\varphi| > 0.05\pi$, while a significant improvement is observed at smaller CFO values.

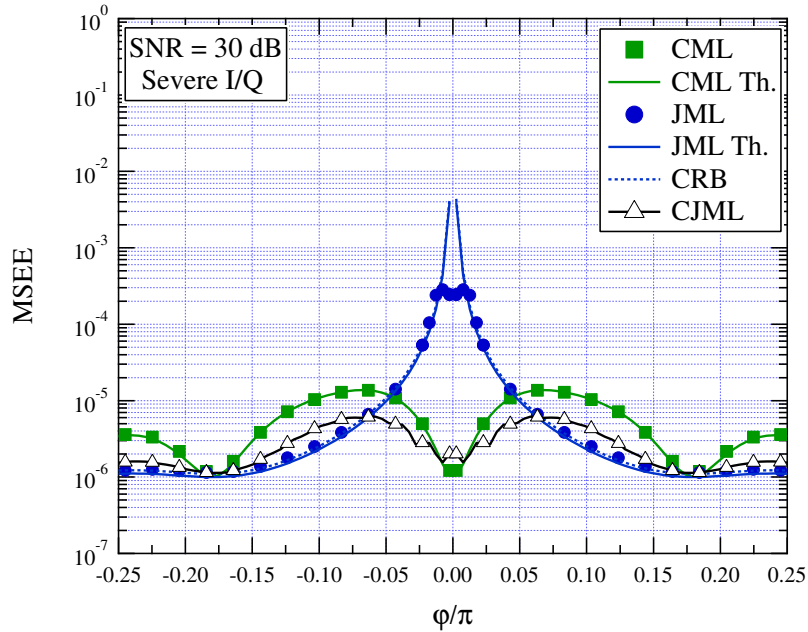


Figure 4.6: Accuracy of the CFO estimators vs φ in the severe I/Q imbalance scenario with $\text{SNR} = 30$ dB.

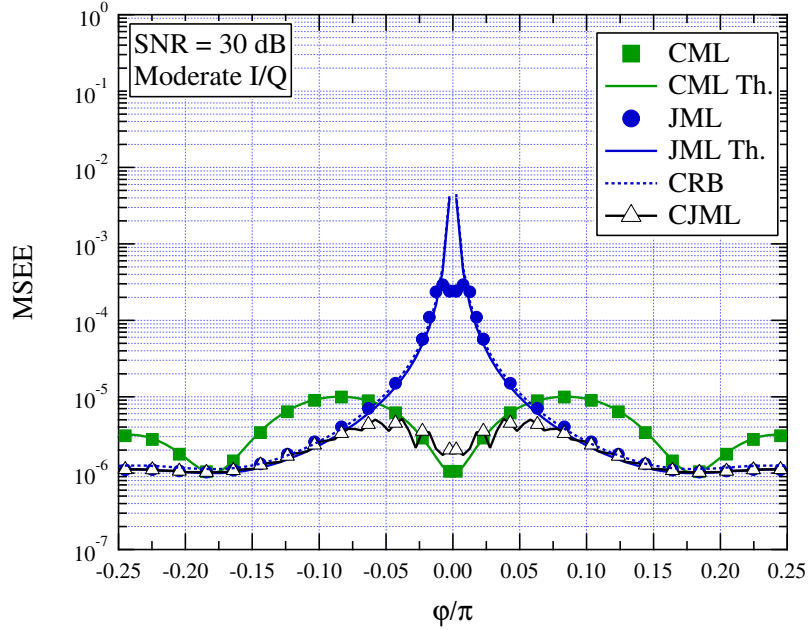


Figure 4.7: Accuracy of the CFO estimators vs φ in the moderate I/Q imbalance scenario with $\text{SNR} = 30$ dB.

Figures 4.8 and 4.9 illustrate the MSEE of the investigated schemes as a function of the SNR for the severe and moderate I/Q scenarios, respectively. The curves are obtained by varying the offset φ at each new simulation run according to a uniform distribution over the range $(-\pi/4, \pi/4)$. Marks indicate simulation results, while solid lines are drawn to facilitate the reading of the graphs. Comparisons are made with some CFO recovery methods available in the open literature, which can cope with I/Q imbalances by exploiting a repeated TP. Specifically, we consider the ESPRIT-based estimator illustrated in [62] and other heuristic algorithms proposed by Pan and Phoong (PP) in [59], by Kume, Lin and Yamashita (KLY) in [61], and by Wang, Xue, Liu, Ye and Ren (WXLRY) in [60]. At SNR values smaller than 24 dB, both CML and CJML exhibit a similar accuracy and outperform all the other methods. As the SNR increases, however, CJML takes the lead due to its improved resilience against mirror interference. Compared to CML and CJML, the ESPRIT-based scheme entails a loss of approximately 5 dB, which increases to 10 dB when considering the JML. Such a remarkable loss can be explained by recalling the poor accuracy of JML in case of small CFO values.

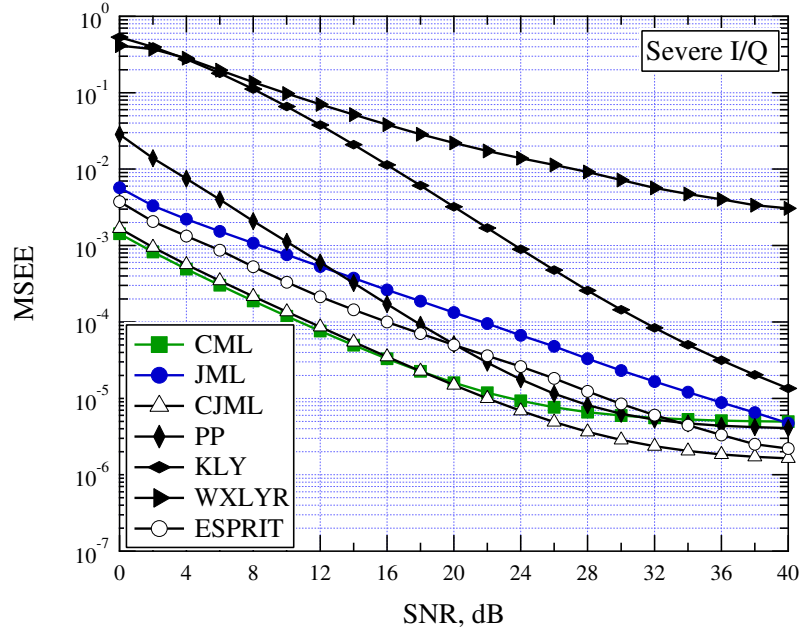


Figure 4.8: Accuracy of the CFO estimators vs SNR in the severe I/Q imbalance scenario.

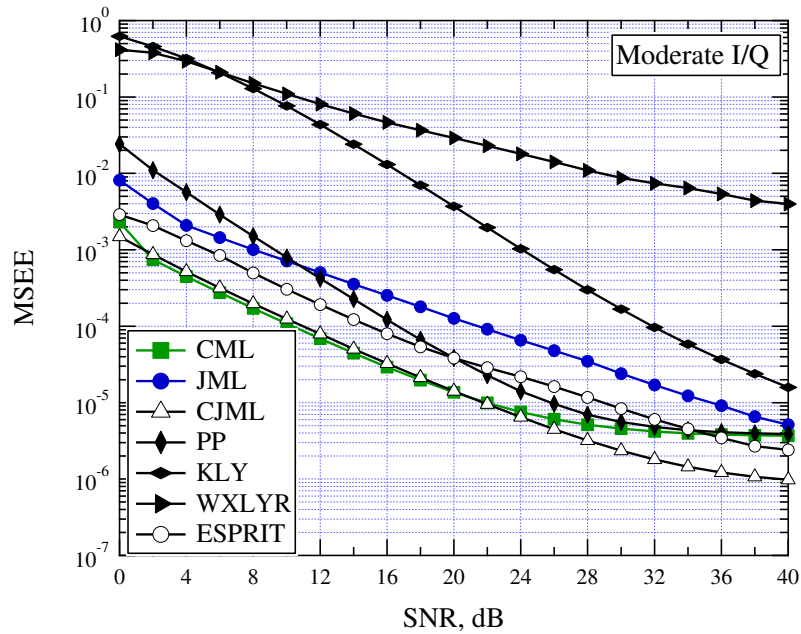


Figure 4.9: Accuracy of the CFO estimators vs SNR in the moderate I/Q imbalance scenario.

The PP algorithm operates satisfactorily at medium-to-high SNR values, while a significant degradation is observed when the SNR decreases. As for KLY and WXLRY, they perform quite poorly. This is particularly true for the latter scheme, which is plagued by a considerable floor in its MSEE curve.

4.8 Concluding remarks

We have presented an analytical investigation of the frequency recovery problem in a direct-conversion receiver affected by frequency selective I/Q imbalance. The considered communication system is an OFDM burst-mode transmission, wherein each frame is preceded by a conventional TP composed of several repeated parts. The first objective of our study was to check whether traditional CFO estimators derived without considering any I/Q impairment can be applied or not to a DCR architecture. For this purpose, we have analytically assessed the performance of the conventional ML (CML) scheme in two different scenarios characterized by either moderate or severe imbalance. Next, we have reviewed and analyzed the JML method, which provides joint estimates of the CFO, the useful signal component and its mirror image. Finally, we have derived a novel scheme (CJML), which aims to improve the estimation accuracy by exploiting some side-information about the signal-to-interference ratio. It was shown that both CML and JML can be obtained from CJML by properly adjusting the value of a design parameter.

Computer simulations have been run to validate the theoretical results and to compare various CFO recovery schemes in a realistic WLAN scenario. The main conclusions that can be drawn from this study are as follows:

- i) CJML is characterized by an excellent accuracy independently of the CFO value and the operating SNR;
- ii) although CML is a biased estimator, it performs similarly to CJML at SNR values of practical interest, while some degradation is observed in the high SNR region;
- iii) JML performs poorly for small CFO values and exhibits a loss of approximately 10 dB with respect to CML and CJML;
- iv) alternative schemes based on the ESPRIT algorithm or other heuristic approaches perform worse than CML and CJML;

- v) CML is a practical and powerful estimator, even when applied to a commercial direct-conversion receiver. This result is in contrast with the prevailing idea that conventional frequency recovery schemes for OFDM systems perform poorly in the presence of I/Q imbalance. Actually, our analysis reveals that the gain achievable when using more sophisticated schemes like CJML is quite marginal and can barely justify the required extra complexity.

Appendix A

In this Appendix we evaluate the mean and the MSEE of the CML estimate given in (4.17) under the simplifying assumption that the noise term $w(t)$ in (4.1) is a ZMCSG complex random process. We begin by taking the derivatives of $\Psi_{CML}(\varphi)$ in (4.19), yielding

$$\Psi'_{CML}(\varphi) = \sum_{m=0}^{M-1} \sum_{k=0}^{M-1} (k-m) \Im \left\{ \mathbf{x}_m^H \mathbf{x}_k e^{j(m-k)\varphi} \right\} \quad (4.72)$$

$$\Psi''_{CML}(\varphi) = - \sum_{m=0}^{M-1} \sum_{k=0}^{M-1} (k-m)^2 \Re \left\{ \mathbf{x}_m^H \mathbf{x}_k e^{j(m-k)\varphi} \right\} \quad (4.73)$$

and rewrite (4.7) in vector form as

$$\mathbf{x}_m = \boldsymbol{\eta}_m + \mathbf{w}_m \quad (4.74)$$

where $\boldsymbol{\eta}_m$ is defined as

$$\boldsymbol{\eta}_m = \mathbf{a} e^{j[m-(M-1)/2]\varphi} + \mathbf{b} e^{-j[m-(M-1)/2]\varphi} \quad (4.75)$$

and $\{\mathbf{w}_m; m = 0, 1, \dots, M-1\}$ are statistically independent ZMCSG random vectors with covariance matrix $\sigma_w^2 \mathbf{I}_P$. Denoting by $\delta(n)$ the Kronecker delta function, from (4.74) we get

$$\mathbb{E} \left\{ \mathbf{x}_m^H \mathbf{x}_k e^{j(m-k)\varphi} \right\} = \boldsymbol{\eta}_m^H \boldsymbol{\eta}_k e^{j(m-k)\varphi} + \sigma_w^2 P \delta(m-k) e^{j(m-k)\varphi} \quad (4.76)$$

which, after substitution into (4.72) and (4.73), produces

$$\mathbb{E} \{ \Psi'_{CML}(\varphi) \} = M^2 q'_M(\varphi) [q_M(\varphi) \|\mathbf{b}\|^2 + \Re \{ \mathbf{a}^H \mathbf{b} \}] \quad (4.77)$$

and

$$\begin{aligned} & \mathbb{E}\{\Psi''_{CML}(\varphi)\} = \\ & -\frac{M^2(M^2-1)}{6} \left\{ \|\mathbf{a}\|^2 + [q_M(\varphi) - \gamma_M(\varphi)] \Re\{\mathbf{a}^H \mathbf{b}\} - [\beta_M(\varphi) + q_M(\varphi)\gamma_M(\varphi)] \|\mathbf{b}\|^2 \right\} \end{aligned} \quad (4.78)$$

where $q_M(\varphi)$, $\beta_M(\varphi)$ and $\gamma_M(\varphi)$ are defined in (4.23) and (4.25). Finally, inserting these results into (4.20) yields $\mathbb{E}\{\varepsilon_{CML}\}$ as given in (4.22).

Now, we concentrate on the computation of the MSEE. From (4.21), it turns out that we need the expectation of the quantity $[\Psi'_{CML}(\varphi)]^2$ which, using (4.72), can be rewritten as

$$[\Psi'_{CML}(\varphi)]^2 = - \sum_{m=0}^{M-1} \sum_{k=0}^{M-1} \sum_{n=0}^{M-1} \sum_{\ell=0}^{M-1} (m-k)(n-\ell) e^{j(m-k)\varphi} e^{j(n-\ell)\varphi} \mathbf{x}_m^H \mathbf{x}_k \mathbf{x}_n^H \mathbf{x}_\ell. \quad (4.79)$$

The expectation with respect to the ZMCSG vectors $\{\mathbf{w}_m; m = 0, 1, \dots, M-1\}$ is computed from (4.79) using the identity

$$\mathbb{E}\{\mathbf{w}_m^H \mathbf{w}_k \mathbf{w}_n^H \mathbf{w}_\ell\} = P^2 \sigma_w^4 \delta(m-k) \delta(n-\ell) + P \sigma_w^4 \delta(m-\ell) \delta(k-n) \quad (4.80)$$

and is found to be

$$\mathbb{E}\{[\Psi'_{CML}(\varphi)]^2\} = [\mathbb{E}\{\Psi'_{CML}(\varphi)\}]^2 + \frac{M^3(M^2-1)}{6} A_M(\varphi) \sigma_w^2 + P \frac{M^2(M^2-1)}{6} \sigma_w^4 \quad (4.81)$$

where $A_M(\varphi)$ is defined in (4.27). Finally, taking (4.78) and (4.81) into account, yields the MSEE of $\hat{\varphi}_{CML}$ as expressed in (4.26).

Appendix B

In this Appendix we provide the solution to the optimization problem (4.48). For this purpose, we rewrite (4.48) as

$$\begin{aligned} \min_{\tilde{\varphi}} \quad & \left\{ \min_{\tilde{\boldsymbol{\theta}}} \sum_{p=0}^{P-1} \left\| \mathbf{x}(p) - \mathbf{A}_2(\tilde{\varphi}) \tilde{\boldsymbol{\theta}}(p) \right\|^2 \right\} \\ \text{s.t.} \quad & \|\tilde{\mathbf{b}}\|^2 \leq \delta \|\tilde{\mathbf{a}}\|^2 \end{aligned} \quad (4.82)$$

and start by solving the inner optimization problem with respect to $\tilde{\boldsymbol{\theta}}$ and for a fixed $\tilde{\varphi}$. Applying the Karush-Kuhn-Tucker (KKT) conditions to the Lagrangian function

$$\mathcal{L}(\tilde{\mathbf{a}}, \tilde{\mathbf{b}}, \lambda) = \sum_{p=0}^{P-1} \left\| \mathbf{x}(p) - \tilde{a}(p)\mathbf{u}(\tilde{\varphi}) - \tilde{b}(p)\mathbf{u}(-\tilde{\varphi}) \right\|^2 + \lambda(\|\tilde{\mathbf{b}}\|^2 - \delta\|\tilde{\mathbf{a}}\|^2) \quad (4.83)$$

we obtain

$$\frac{\partial}{\partial \tilde{a}^*(p)} \mathcal{L}(\tilde{\mathbf{a}}, \tilde{\mathbf{b}}, \lambda) = \left[\|\mathbf{u}(\tilde{\varphi})\|^2 - \lambda\delta \right] \tilde{a}(p) + \mathbf{u}^H(\tilde{\varphi})\mathbf{u}(-\tilde{\varphi})\tilde{b}(p) - \mathbf{u}^H(\tilde{\varphi})\mathbf{x}(p) = 0 \quad (4.84a)$$

$$\frac{\partial}{\partial \tilde{b}^*(p)} \mathcal{L}(\tilde{\mathbf{a}}, \tilde{\mathbf{b}}, \lambda) = \mathbf{u}^H(-\tilde{\varphi})\mathbf{u}(\tilde{\varphi})\tilde{a}(p) + \left[\|\mathbf{u}(-\tilde{\varphi})\|^2 + \lambda \right] \tilde{b}(p) - \mathbf{u}^H(-\tilde{\varphi})\mathbf{x}(p) = 0 \quad (4.84b)$$

for $p = 0, 1, \dots, P-1$, with

$$\lambda \geq 0 \quad \|\tilde{\mathbf{b}}\|^2 - \delta\|\tilde{\mathbf{a}}\|^2 \leq 0 \quad \lambda(\|\tilde{\mathbf{b}}\|^2 - \delta\|\tilde{\mathbf{a}}\|^2) = 0. \quad (4.84c)$$

After some algebraic computations, the solution of the KKT equations is found to be

$$\hat{a}(p) = \frac{[M + \lambda(\tilde{\varphi})]\mathbf{u}^H(\tilde{\varphi})\mathbf{x}(p) - \mathbf{u}^H(\tilde{\varphi})\mathbf{u}(-\tilde{\varphi})\mathbf{u}^H(-\tilde{\varphi})\mathbf{x}(p)}{[M - \delta\lambda(\tilde{\varphi})][M + \lambda(\tilde{\varphi})] - |\mathbf{u}^H(\tilde{\varphi})\mathbf{u}(-\tilde{\varphi})|^2} \quad (4.85a)$$

$$\hat{b}(p) = \frac{[M - \delta\lambda(\tilde{\varphi})]\mathbf{u}^H(-\tilde{\varphi})\mathbf{x}(p) - \mathbf{u}^H(-\tilde{\varphi})\mathbf{u}(\tilde{\varphi})\mathbf{u}^H(\tilde{\varphi})\mathbf{x}(p)}{[M - \delta\lambda(\tilde{\varphi})][M + \lambda(\tilde{\varphi})] - |\mathbf{u}^H(\tilde{\varphi})\mathbf{u}(-\tilde{\varphi})|^2} \quad (4.85b)$$

$$\lambda(\tilde{\varphi}) = \max \left(0, \frac{\Upsilon_2(\tilde{\varphi}) - \sqrt{\Upsilon_2^2(\tilde{\varphi}) - \Upsilon_1(\tilde{\varphi})\Upsilon_3(\tilde{\varphi})}}{\Upsilon_1(\tilde{\varphi})} \right) \quad (4.85c)$$

where $\Upsilon_1(\tilde{\varphi})$, $\Upsilon_2(\tilde{\varphi})$ and $\Upsilon_3(\tilde{\varphi})$ are defined in (4.56)–(4.58), and the dependence of $\hat{a}(p)$ and $\hat{b}(p)$ on $\tilde{\varphi}$ has been omitted in (4.85a) and (4.85b) to ease the notation. The optimal value of $\tilde{\varphi}$ that solves (4.82) is eventually obtained by searching for the global minimum of the concentrated likelihood function, i.e.,

$$\hat{\varphi}_c = \arg \min_{\tilde{\varphi} \in [-\pi, \pi)} \sum_{p=0}^{P-1} \left\| \mathbf{x}(p) - \hat{a}(p)\mathbf{u}(\tilde{\varphi}) - \hat{b}(p)\mathbf{u}(-\tilde{\varphi}) \right\|^2 \quad (4.86)$$

Taking (4.85a) and (4.85b) into account leads to the CJML estimator shown in (4.49)–(4.51).

Appendix C

In this Appendix we compute the CRB for the estimation of φ based on the signal model shown in (4.62) and (4.63). For this purpose, we collect the unknown parameters into a $(4P + 1)$ -dimensional vector $\boldsymbol{\varsigma} = [\varphi \mathbf{z}^T]^T$ and let \mathbf{C}_w be the correlation matrix of \mathbf{w} in (4.62). Then, the entries of the Fisher information matrix (FIM) $\mathbf{F}_{\boldsymbol{\varsigma}}$ are given by [4]

$$[\mathbf{F}_{\boldsymbol{\varsigma}}]_{k_1, k_2} = \left(\frac{\partial \boldsymbol{\eta}}{\partial \varsigma_{k_1}} \right)^T \mathbf{C}_w^{-1} \left(\frac{\partial \boldsymbol{\eta}}{\partial \varsigma_{k_2}} \right) \quad 1 \leq k_1, k_2 \leq 4P + 1. \quad (4.87)$$

Taking (4.64)–(4.66) into account, after lengthy computations we get

$$\mathbf{F}_{\boldsymbol{\varsigma}} = \begin{bmatrix} \gamma & \mathbf{m}^T \\ \mathbf{m} & \mathbf{M} \end{bmatrix} \quad (4.88)$$

where $\gamma = \mathbf{z}^T \dot{\mathbf{Q}}^T \mathbf{C}_w^{-1} \dot{\mathbf{Q}} \mathbf{z}$, $\mathbf{m} = \mathbf{Q}^T \mathbf{C}_w^{-1} \dot{\mathbf{Q}} \mathbf{z}$ and $\mathbf{M} = \mathbf{Q}^T \mathbf{C}_w^{-1} \mathbf{Q}$. In the latter expressions, $\dot{\mathbf{Q}}$ is defined as

$$\dot{\mathbf{Q}} = \frac{\partial \mathbf{Q}}{\partial \varphi} = \begin{bmatrix} \dot{\mathbf{Q}}_0^T & \dot{\mathbf{Q}}_1^T & \cdots & \dot{\mathbf{Q}}_{M-1}^T \end{bmatrix}^T. \quad (4.89)$$

with $\dot{\mathbf{Q}}_m = \text{diag}\{\underbrace{\dot{\mathbf{R}}_m, \dot{\mathbf{R}}_m, \dots, \dot{\mathbf{R}}_m}_P\}$ and

$$\dot{\mathbf{R}}_m = \left(m - \frac{M-1}{2} \right) \begin{bmatrix} -s_m(\varphi) & -c_m(\varphi) & -s_m(\varphi) & c_m(\varphi) \\ c_m(\varphi) & -s_m(\varphi) & -c_m(\varphi) & -s_m(\varphi) \end{bmatrix}. \quad (4.90)$$

The CRB for the estimation of φ corresponds to $[\mathbf{F}_{\boldsymbol{\varsigma}}^{-1}]_{1,1}$. Using well-known results for the inverse of a partitioned matrix [4], we obtain

$$\text{CRB}(\varphi) = \frac{1}{\gamma - \mathbf{m}^T \mathbf{M}^{-1} \mathbf{m}} \quad (4.91)$$

which reduces to (4.67) after using the expressions of γ , \mathbf{m} and \mathbf{M} .

Chapter 5

Carrier Frequency Recovery for Filtered Multitone Modulations

5.1 Introduction

Multicarrier modulations, such as orthogonal frequency-division multiplexing (OFDM) and filtered multitone (FMT), are regarded as key technologies to achieve high data rates in time-frequency selective propagation scenarios. Here we focus on the FMT signal format, firstly proposed for digital subscriber lines [68] and soon after adopted in a variety of wireless standards such as the DVB-RCT [69] and the recent TETRA Release 2 Enhanced Data Service (TEDS) [70]. Sparse pilot symbols are inserted in the data stream according to a given pilot pattern (PP), so as to permit channel estimation at the receiver at all time-frequency symbol positions. For instance, TEDS envisages a rectangular-grid PP, with pilots sent periodically over a fixed set of subcarriers (SCs) [70], while DVB-RCT employs a staggered pattern with cyclic transmission of pilots on different groups of SCs [69]. Additional known symbols are usually included for recovery/cancellation of carrier frequency offset (CFO), a task to be accomplished prior to channel estimation/equalization. To this aim the cited standards recommend the use of a synchronization preamble/postamble at each data

frame, permitting joint acquisition/tracking of frame/symbol timing and CFO. While the latter approach achieves a wide acquisition range (AR) thanks to these dedicated symbols being closely spaced in time, it is not equally satisfactory in terms of mean square estimation error (MSEE), whose minimization conversely requires that pilots are arranged as far as possible from each other. To relieve this drawback, in [71] a maximum-likelihood (ML) technique is proposed whereby the CFO is estimated from the sparse pilot symbols intended for channel recovery rather than from packed synchronization symbols. The focus therein is limited to a TEDS-like signal format with a rectangular-grid PP. Actually the above approach is shown to improve the MSEE, but this advantage is paid in terms of a narrower AR, as this occurs to be roughly as wide as the inverse of the time-domain pilot separation. In [72] a method is discussed overcoming the issue by jointly exploiting the sparse pilot symbols along with tentative differential decisions on data symbols, thus succeeding in broadening the AR by a factor 2-3 while retaining the same or slightly improved MSEE. However this technique is computationally more demanding than the pilot-only based CFO estimator in [71] and its suitability with modulation formats more complex than 4-QAM is doubtful. We make a step ahead providing further results that integrate those in [71]- [72]. We show that a viable sparse-pilot-only based technique capable of widening the AR is the adoption of a non-rectangular PP with pilots simply shifted in time over the SCs with respect to the rectangular pattern. With reference to a TEDS-like signal format, we take up the ML Pilot Aided (PA) frequency synchronizer in [71] and analyze its performance when used in conjunction with two specific non-rectangular PPs, demonstrating their capability to significantly widen the AR, with little or no effect on estimation accuracy, nor on algorithm complexity. We finally assess the impact of all cited PPs on a notional FMT receiver over doubly selective channels by presenting curves of frame error rate (FER) vs. signal-to-noise ratio (SNR). It is also shown how over fast fading channels the AR can be traded off against FER performance.

5.2 Signal and channel models

The analog baseband FMT signal for a burst composed of L blocks and N SCs can be written as [68]

$$s(t) = \sum_{l=0}^{L-1} \sum_{n=0}^{N-1} c_l^{(n)} g(t - lT) e^{j2\pi nMt/NT} \quad (5.1)$$

where $c_l^{(n)}$ denotes the QAM symbol transmitted on block l and SC n , $g(t)$ is the impulse response of a square-root-raised-cosine filter with roll-off factor ξ , shaping the signal spectrum on each SC, T is the SC symbol spacing and the parameter $M \triangleq (1 + \xi)N$ is constrained to be an integer for ease of system implementation. The signal in (5.1) is transmitted over a U -path time-varying channel, whose Gaussian independent circular path gains and delays, all assumed approximately constant over the time span of $g(t)$, are denoted as $\rho_u(t)$ and τ_u , respectively, and whose impulse response is $h(t) = \sum_{u=0}^{U-1} \rho_u(t) \delta(t - \tau_u)$. It can be shown [71], under some mild assumptions, that at the receiver site, after proper processing, the matched filter output from the n -th SC at the instant $t = kT$ can be written as follows:

$$z_k^{(n)} \simeq \phi_k^{(n)} c_k^{(n)} e^{j2\pi\nu k} + w_k^{(n)} \quad (5.2)$$

where

$$\phi_k^{(n)} \triangleq e^{j\Theta} \sum_{u=0}^{U-1} \rho_u(kT) e^{j2\pi nM\tau_u/NT} \quad (5.3)$$

is a multiplicative (fading) factor affecting the k -th symbol over the n -th SC, accounting for channel double selectivity, ν is the CFO normalized to the rate $1/T$, Θ is the phase offset, and finally $w_k^{(n)}$ is a zero-mean uncorrelated circular Gaussian noise sequence with variance $\sigma^2 = 2N_0$.

5.3 CFO estimation algorithm

We borrow here the ML PA CFO estimator analyzed in [71], limiting ourselves to review the basic steps leading to the estimator formulation. Let $S \leq N$ denote the number of SCs utilized to host pilot symbols, each bearing a fixed number $P \leq L$ of unit-energy pilots. The overall number of pilots in the burst is then $N_P = SP$. Let the pair of indices (a_j, b_{i,a_j}) , $j = 0, \dots, S-1$, $i = 0, \dots, P-1$, identify the position of

the generic pilot symbol $p_{b_{i,a_j}}^{(a_j)}$, where $a_j \in \mathcal{A}$ and $b_{i,a_j} \in \mathcal{B}^{(a_j)}$ denote the SC and time indices, respectively, and where the sets \mathcal{A} and $\mathcal{B}^{(a_j)}$ define the PP. After modulation removal, the sample associated to the above pilot position is

$$y_{b_{i,a_j}}^{(a_j)} = z_{b_{i,a_j}}^{(a_j)} / p_{b_{i,a_j}}^{(a_j)} = \phi_{b_{i,a_j}}^{(a_j)} e^{j2\pi\nu b_{i,a_j}} + \zeta_{b_{i,a_j}}^{(a_j)}, \quad (5.4)$$

where the noise term $\zeta_{b_{i,a_j}}^{(a_j)}$ is statistically equivalent to $w_{b_{i,a_j}}^{(a_j)}$ in (5.2). Then, after defining

$$\mathbf{y}^{(a_j)} \triangleq [y_{b_{0,a_j}}^{(a_j)}, y_{b_{1,a_j}}^{(a_j)}, \dots, y_{b_{P-1,a_j}}^{(a_j)}]^T \quad (5.5)$$

$$\boldsymbol{\phi}^{(a_j)} \triangleq [\phi_{b_{0,a_j}}^{(a_j)}, \phi_{b_{1,a_j}}^{(a_j)}, \dots, \phi_{b_{P-1,a_j}}^{(a_j)}]^T \quad (5.6)$$

$$\boldsymbol{\zeta}^{(a_j)} \triangleq [\zeta_{b_{0,a_j}}^{(a_j)}, \zeta_{b_{1,a_j}}^{(a_j)}, \dots, \zeta_{b_{P-1,a_j}}^{(a_j)}]^T \quad (5.7)$$

$$\mathbf{A}^{(a_j)}(\nu) \triangleq \text{diag}\{e^{j2\pi\nu b_{0,a_j}}, \dots, e^{j2\pi\nu b_{P-1,a_j}}\}, \quad (5.8)$$

the set of samples (5.4) relevant to the a_j -th SC can be written in matrix notation as

$$\mathbf{y}^{(a_j)} = \mathbf{A}^{(a_j)}(\nu) \boldsymbol{\phi}^{(a_j)} + \boldsymbol{\zeta}^{(a_j)}. \quad (5.9)$$

Next, stacking (5.5)-(5.7) so as to form the vectors

$$\mathbf{y} \triangleq [\mathbf{y}^{(a_0)T}, \mathbf{y}^{(a_1)T}, \dots, \mathbf{y}^{(a_{S-1})T}]^T \quad (5.10)$$

$$\boldsymbol{\phi} \triangleq [\boldsymbol{\phi}^{(a_0)T}, \boldsymbol{\phi}^{(a_1)T}, \dots, \boldsymbol{\phi}^{(a_{S-1})T}]^T \quad (5.11)$$

$$\boldsymbol{\zeta} \triangleq [\boldsymbol{\zeta}^{(a_0)T}, \boldsymbol{\zeta}^{(a_1)T}, \dots, \boldsymbol{\zeta}^{(a_{S-1})T}]^T, \quad (5.12)$$

the observed sequence corresponding to the pilot locations of the whole FMT burst can be expressed as

$$\mathbf{y} \triangleq \boldsymbol{\Gamma}(\nu) \boldsymbol{\phi} + \boldsymbol{\zeta} \quad (5.13)$$

where $\boldsymbol{\Gamma}(\nu)$ is a $N_P \times N_P$ diagonal matrix defined as

$$\boldsymbol{\Gamma}(\nu) \triangleq \text{diag}\{\mathbf{A}^{(a_0)}(\nu), \mathbf{A}^{(a_1)}(\nu), \dots, \mathbf{A}^{(a_{S-1})}(\nu)\} \quad (5.14)$$

and $\boldsymbol{\phi}$ and $\boldsymbol{\zeta}$ are zero-mean Gaussian vectors having (Hermitian) covariance matrices $\mathbf{C}_\phi = E\{\boldsymbol{\phi}\boldsymbol{\phi}^H\}$ and $\mathbf{C}_\zeta = E\{\boldsymbol{\zeta}\boldsymbol{\zeta}^H\} = \sigma^2 \mathbf{I}_{N_P}$, respectively. Following a standard

derivation [71], we observe that for fixed $\nu = \tilde{\nu}$ the vector (5.13) is Gaussian, leading to the log-likelihood function (LLF)

$$\Lambda(\mathbf{y}|\tilde{\nu}) \triangleq -\Psi(\mathbf{y}|\tilde{\nu}) = -\mathbf{y}^H \mathbf{\Gamma}(\tilde{\nu})(\mathbf{C}_\phi + \sigma^2 \mathbf{I}_{N_P})^{-1} \mathbf{\Gamma}^H(\tilde{\nu}) \mathbf{y}. \quad (5.15)$$

5.3.1 Exact ML estimator

From (5.15) we obtain the ML CFO estimator (MLE)

$$\hat{\nu} = \arg \min_{\tilde{\nu} \in \mathcal{I}} \{\Psi(\mathbf{y}|\tilde{\nu})\} \quad (5.16)$$

where \mathcal{I} is the search interval for $\tilde{\nu}$, whose width clearly reflects the amount of uncertainty in the *a priori* knowledge of ν . For the algorithm to be useful, this uncertainty interval must not exceed the AR of the estimator.

5.3.2 Approximate ML estimator

Use of (5.16) requires knowledge of the actual noise power σ^2 which is not always available. To circumvent the issue it might be useful to let $\sigma^2 \rightarrow 0$ (i.e., $\text{SNR} \rightarrow \infty$), leading to the alternative metric

$$\hat{\nu} = \arg \min_{\tilde{\nu} \in \mathcal{I}} \{\Theta(\mathbf{y}|\tilde{\nu})\} \quad (5.17)$$

where

$$\Theta(\mathbf{y}|\tilde{\nu}) \triangleq \mathbf{y}^H \mathbf{\Gamma}(\tilde{\nu}) \mathbf{C}_\phi^{-1} \mathbf{\Gamma}^H(\tilde{\nu}) \mathbf{y}. \quad (5.18)$$

Unfortunately the matrix \mathbf{C}_ϕ is almost singular and its inversion may suffer from numerical instability. A way out from this impasse is to slightly modify the metric in (5.18) so as to prevent the above instability. This can be done by simply replacing the noise variance required in (5.16) with a constant value σ_0^2 , set equal to the noise variance relevant to a given reference SNR, e.g. the maximum envisaged SNR or the SNR at the nominal receiver sensitivity. Accordingly, the modified LLF is

$$\Psi_0(\mathbf{y}|\tilde{\nu}) \triangleq \mathbf{y}^H \mathbf{\Gamma}(\tilde{\nu})(\mathbf{C}_\phi + \sigma_0^2 \mathbf{I})^{-1} \mathbf{\Gamma}^H(\tilde{\nu}) \mathbf{y} \quad (5.19)$$

and the related estimation strategy (referred to as fixed-MLE, or FMLE, in the sequel) is

$$\hat{\nu} = \arg \min_{\tilde{\nu} \in \mathcal{I}} \{\Psi_0(\mathbf{y}|\tilde{\nu})\}. \quad (5.20)$$

It is worth observing that the complexity of the above algorithms depends on N_P , but not on the actual PP.

5.4 System definition and simulation results

5.4.1 Signal format

For the sake of concreteness, the signal format and the set of simulation parameters are taken to be compatible with those adopted in the TEDS standard [70]. The number of SCs is fixed at $N = 16$, while the burst length is $L = 50$. The modulation format used throughout the burst is 4-QAM, with symbol spacing $T = 1/2400$ s and roll-off factor $\xi = 0.25$. The information bits are protected by a rate-1/2 PCCC turbo encoder, with feedforward and feedback generators in both RSC blocks given by 15 and 13 (in octal), respectively. The coded bits are next passed through a linear-congruence interleaver of the type described in [73]. The 6-path channel model presents an exponentially decaying power-delay profile¹ with normalized delay spread $\sigma_\tau/T = 0.02$. As for time selectivity, we consider two scenarios, namely, slow fading (SF) and fast fading (FF), simulated by setting $f_D T = 0.0075$ and $f_D T = 0.03$, respectively, where f_D denotes the Doppler spread. Assuming carrier frequency $f_0 = 400$ MHz (one of the options in TEDS), the above choice implies a terminal speed around 60 km/h and 260 km/h, for the SF and FF scenarios, respectively. Furthermore for the FMLE scheme the noise variance is set at the value yielding $E_s/N_0 = 5$ dB.

5.4.2 Pilot pattern

In this section we define the three PPs adopted in the simulations, with the following common properties:

1. the number of pilot-bearing SCs is $S = N/2$ and the relevant index set is taken as $\mathcal{A} = \{a_0 = 0, a_1 = 2, \dots, a_{\frac{S}{2}-1} = \frac{N}{2} - 2, a_{\frac{S}{2}} = \frac{N}{2} + 1, a_{\frac{S}{2}+1} = \frac{N}{2} + 3, \dots, a_{S-1} = N - 1\}$;
2. on all pilot-bearing SCs, there are P pilot symbols evenly spaced δ_T symbols apart;
3. the ratio $\chi = \frac{PS}{LN}$ between the total number of pilot symbols and the total number of burst symbols is fixed. Specifically, in the simulations we let $\chi = 0.05$, implying time-domain symbol spacing $\delta_T = 10$ and $P = \lfloor \frac{L}{\delta_T} \rfloor = 5$.

¹In the simulations we let $\tau_u = 5u \mu\text{s}$, for $u = 0, \dots, 5$.

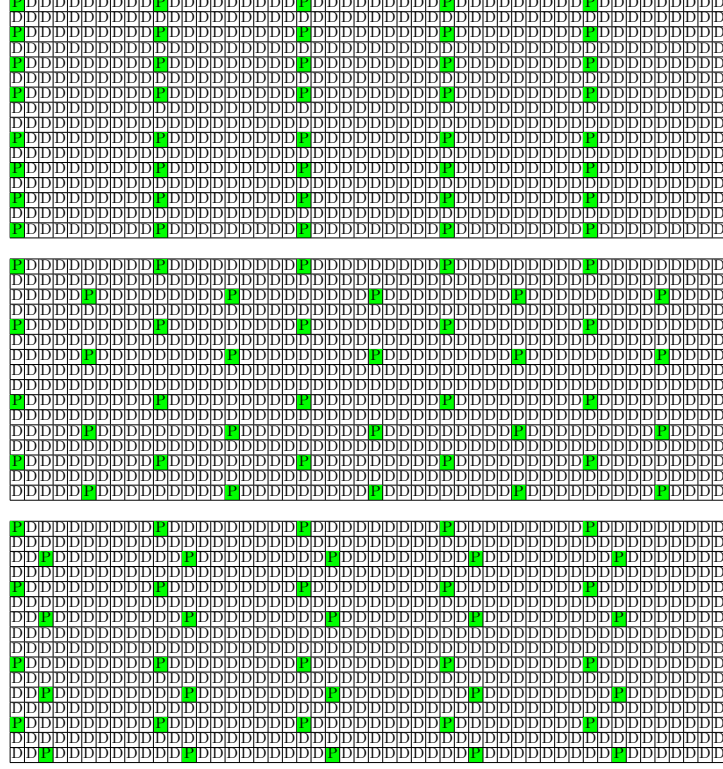


Figure 5.1: From top to bottom: PP1, PP2, PP3. P = pilot, D = data.

The first pilot pattern (PP1), used as benchmark, is rectangular and very similar to that standardized in the TEDS normal downlink burst [70], [74]. In PP1, the time-domain pilot arrangement is identical for each pilot-bearing SC, i.e.,

$$\mathcal{B}^{(a_j)} = \{0, \delta_T, \dots, (P-1)\delta_T\} \quad \text{for } a_j \in \mathcal{A}.$$

The second pattern (PP2) has staggered pilots, as follows

$$\mathcal{B}^{(a_j)} = \begin{cases} \{0, \delta_T, \dots, (P-1)\delta_T\} & \text{for } a_j \in \mathcal{A}^{(I)} \\ \{\frac{\delta_T}{2}, \frac{3\delta_T}{2}, \dots, \frac{(2P-1)\delta_T}{2}\} & \text{for } a_j \in \mathcal{A}^{(II)} \end{cases}$$

while the third PP (PP3) is somewhat midway between the former two

$$\mathcal{B}^{(a_j)} = \begin{cases} \{0, \delta_T, \dots, (P-1)\delta_T\} & \text{for } a_j \in \mathcal{A}^{(I)} \\ \{2, 2 + \delta_T, \dots, 2 + (P-1)\delta_T\} & \text{for } a_j \in \mathcal{A}^{(II)} \end{cases}$$

$\mathcal{A}^{(I)}$ and $\mathcal{A}^{(II)}$ being the elements of \mathcal{A} with even and odd indices, respectively. The three above PPs are shown in Fig. 5.1 for $N = 16$. The previous arrangement rules can be applied to a burst of arbitrary length composed of an arbitrary even number of SCs.

5.4.3 Impact of PP on acquisition range

The AR can be defined as the interval of values of CFO that can be unambiguously estimated by the synchronizer. Clearly, the AR achieved by PP1 cannot exceed the interval $(-\frac{1}{2\delta_T}, \frac{1}{2\delta_T})$ and may turn out to be very narrow if the pilots are spaced far apart: for instance, the absolute value of ν cannot exceed 0.05 for PP1 in Fig. 5.1. This limit can be considered too restrictive in some applications [72]. However, we found that a wider AR can be achieved without changing the number of pilots, by simply resorting to a staggered PP such as PP2 or PP3 in Fig. 5.1 (other configurations are possible). This can be explained observing [72, eqs. (20)-(23)] that the correlation between two arbitrary samples of the fading process can be written as the product of two terms depending separately on their distance in time and frequency. Therefore, provided the channel is sufficiently correlated in frequency², the ML CFO estimator (5.16) or (5.20) can exploit, among other statistics, phase rotations between pairs of samples of type (5.4) belonging to *different* SCs. Indeed, as far as the AR is concerned, what actually matters is the minimum spacing of pilots in time regardless of the SCs they belong to. This observation permits to predict for PP2 and PP3 values of (one-sided) AR around 0.1 and 0.25, i.e., twice and five times larger, respectively, than the AR of PP1.

5.4.4 Channel estimator

Channel is estimated via the two-step approach suggested in [74], here briefly reviewed. As first step, we use a MMSE Bayesian smoother-interpolator on each

²The above choice of channel parameters leads to a channel correlation coefficient along the frequency axis between consecutive pilot-bearing SCs around 0.87.

pilot-bearing SC, so as to get an estimate of the fading process at all (pilot and data) symbol locations. This requires *a priori* knowledge (or measurement) of the fading covariance matrix over all symbols in a SC, and of noise power as well. The latter could be estimated or replaced by a fixed value, as with the FMLE. Let $\boldsymbol{\Phi}^{(a_j)} \triangleq [\phi_0^{(a_j)}, \dots, \phi_{L-1}^{(a_j)}]^T$ denote the (Gaussian) vector of actual fading samples at the L symbol positions on the j -th pilot-bearing SC, and $\mathbf{C}_{\boldsymbol{\Phi}}$ its covariance matrix

$$\mathbf{C}_{\boldsymbol{\Phi}} \triangleq E\{\boldsymbol{\Phi}^{(a_j)} \boldsymbol{\Phi}^{(a_j)H}\}, \quad (5.21)$$

where the index a_j was dropped on the left side in view of the stationarity properties of the fading process. After modulation removal and (error-free) CFO compensation, an appropriate representation of the noisy samples of the fading process observed at the P pilot positions is, from (5.4)-(5.5)

$$\mathbf{y}^{(a_j)} = \mathbf{H}^{(a_j)} \boldsymbol{\Phi}^{(a_j)} + \mathbf{n}^{(a_j)}, \quad (5.22)$$

where the noise vector $\mathbf{n}^{(a_j)}$ is statistically equivalent to $\boldsymbol{\zeta}^{(a_j)}$ in (5.7), and $\mathbf{H}^{(a_j)}$ is an “observation” matrix of size $P \times L$, whose entries on the i -th row, $i = 0, \dots, P-1$, are all zeros except a single unitary element at position b_{i,a_j} . The Bayesian MMSE linear estimator for $\boldsymbol{\Phi}^{(a_j)}$ is [4]

$$\hat{\boldsymbol{\Phi}}^{(a_j)} = (\mathbf{C}_{\boldsymbol{\Phi}}^{-1} + \mathbf{H}^{(a_j)T} \mathbf{C}_n^{-1} \mathbf{H}^{(a_j)})^{-1} \mathbf{H}^{(a_j)T} \mathbf{C}_n^{-1} \mathbf{y}^{(a_j)}$$

$\mathbf{C}_n \triangleq \sigma^2 \mathbf{I}_P$ denoting the $P \times P$ noise covariance matrix. As next step, simple linear interpolation is applied in the frequency domain (i.e., across the SCs), so as to estimate the fading process at all symbol positions over the remaining SCs.

5.4.5 Simulation results

Figures 5.2 and 5.3 show plots of the MSEE incurred by the MLE and FMLE vs. the actual normalized CFO, for all PPs presented in a previous section for the SF and FF scenarios, respectively.

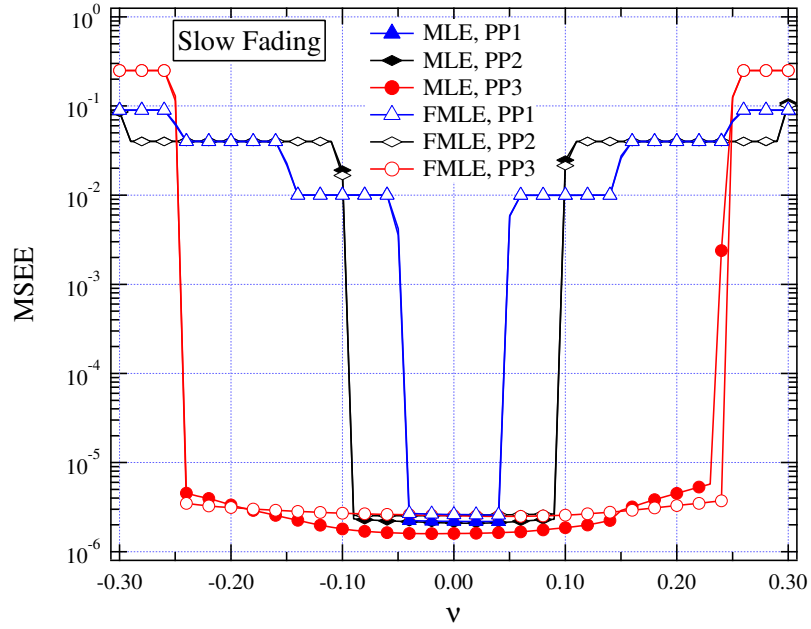


Figure 5.2: $MSEE$ vs. ν for the SF scenario; $E_s/N_0 = 15$ dB.

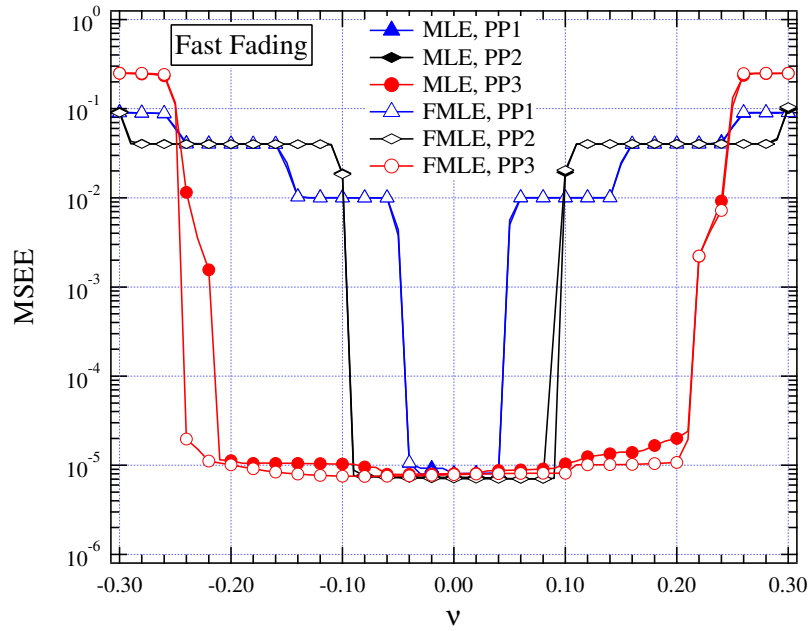


Figure 5.3: $MSEE$ vs. ν for the FF scenario; $E_s/N_0 = 15$ dB.

The SNR is fixed at $E_s/N_0 = 15$ dB while the FMLE assumes $E_s/N_0 = 5$ dB. Inspection of the figures reveals that in the region of correct operation of the estimators (the flat low part of the plots), the MLE and FMLE exhibit substantially the same MSEE, thus confirming that the FMLE is hardly degraded even with rather large SNR mismatches. It is also seen that the MSEE is substantially independent of the PP while, conversely, the choice of PP has a strong impact on the CFO AR, i.e., on the width of the flat region of the MSEE curves. Specifically, it is found that for both SF and FF scenarios, the predictions are substantially confirmed: PP1 has the narrowest AR (around ± 0.04 in the normalized scale), while PP2 does around twice better (± 0.09) and finally PP3 attains a noteworthy ± 0.24 (slightly less in the FF scenario). To assess the impact of the CFO estimator and the PP on the receiver performance, in Figs. 5.4 and 5.5 we also provide plots of FER as a function of E_b/N_0 for both fading scenarios and all considered PPs. It can be seen that the receiver is not affected at

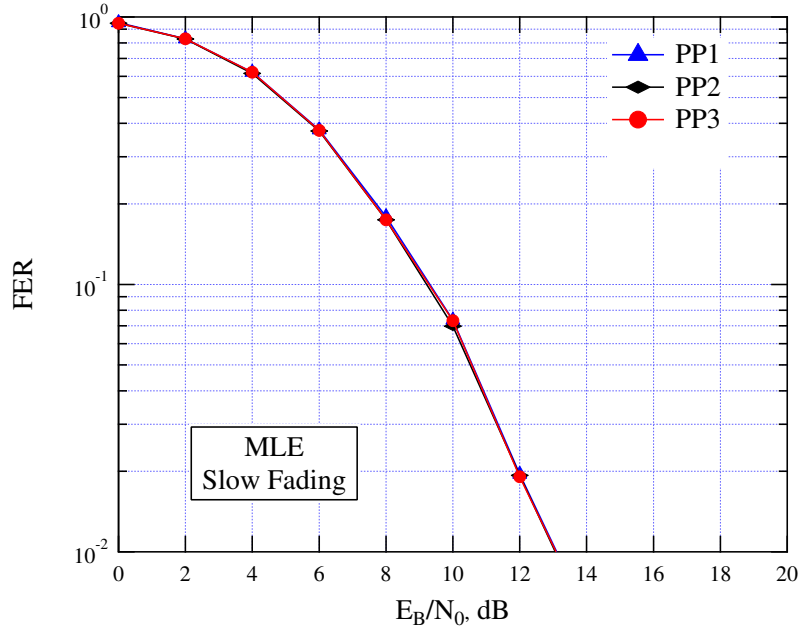


Figure 5.4: FER vs. E_b/N_0 for the SF scenario.

all by the specific PP over the SF scenario, while in the presence of FF use of PP2 and PP3 proves somewhat advantageous with respect to PP1 (a 2-dB gain is observed at $\text{FER} = 10^{-2}$). The reason is, switching from SF to FF tends to decorrelate the fading

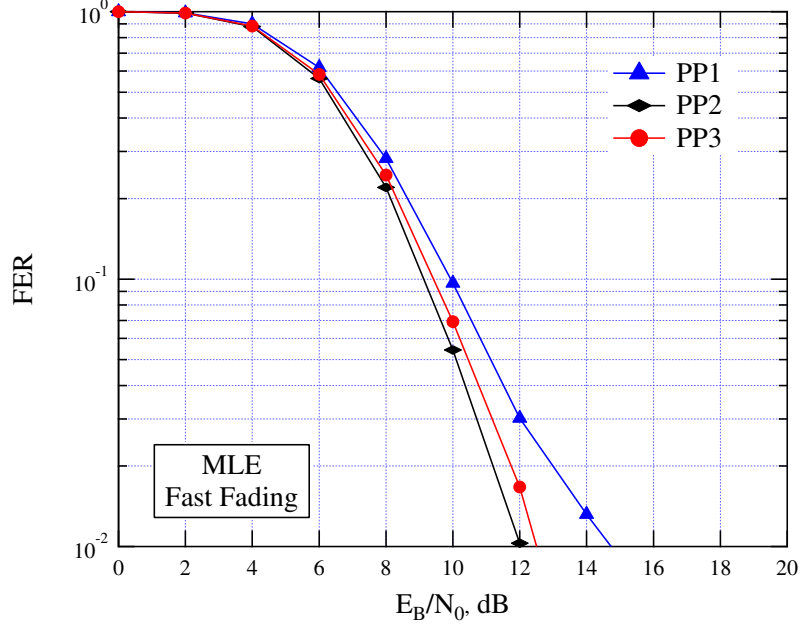


Figure 5.5: *FER vs. E_b/N_0 for the FF scenario.*

process on the time axis, while the frequency-domain correlation is not affected. In consequence, when the fading correlation between consecutive pilot-bearing SCs is sufficiently large, use of PP2 or PP3 is equivalent to a tighter sampling of the fading process in the time domain, thereby improving both channel estimation and decoder performance. This also indicates that the AR can be somewhat traded off against the FER performance, as PP3 entails a larger AR but a slightly worse FER than PP2, and viceversa.

5.5 Concluding remarks

In this chapter we discussed the impact of the PP on the AR of a ML PA CFO estimator for a TEDS-like filtered multitone system. We showed that use of a staggered pilot distribution over the SCs may considerably widen the AR in comparison with the rectangular PP (adopted in the TEDS standard), with no substantial impact on estimation accuracy nor on complexity.

Chapter 6

Distributed Power Control over Interference Channels

6.1 Introduction

The power consumption of the communication technology industry is becoming a major societal and economical concern [75], which has stimulated academia and industry to an intense activity in the new research area of green cellular networks [76]– [78]. The ultimate goal is to design new innovative network architectures and technologies needed to meet the explosive growth in cellular data demand without increasing the power consumption. Along this line of research, in this chapter we focus on a network composed of several single-antenna transmitter-receiver pairs operating over the same frequency band (or time slot) in which each pair aims at selfishly minimizing the power required to achieve a given signal-to-interference-plus-noise ratio (SINR). The mutual interference due to the simultaneous transmissions gives rise to a sort of competition for the common resource. The natural framework to study the solution of such interactions is non-cooperative game theory [6], [79] in which the transmitter-receiver pairs are modeled as players that engage in a game using their own local information while fulfilling the given requirements. The existence and uniqueness properties of the equilibrium points of the underlying game have been widely studied in the literature and a large number of works already exist on this topic [80]– [82]. Particular attention

has also been devoted to derive schemes based on best response dynamics that allow each player to achieve the equilibrium in an iterative and distributed manner. All these schemes rely on the assumption that the transmitter has perfect knowledge of the SINR measured at the receiver. This assumption does not hold true in practical applications and the only way for the transmitter to acquire this knowledge is through a return control channel. Although possible, however, this solution is not compliant with most of the current wireless communication standards in which the receiver only sends back a link-layer acknowledgement (ACK) whenever it is able to correctly decode the message and a negative ACK (NACK) otherwise. Most of the existing works dealing with resource allocation schemes using a 1-bit feedback are for centralized networks (see [83], [84], and references therein), while only a few examples exist in decentralized scenarios. A first attempt in this direction is represented by [85] where the authors propose a distributed power control algorithm maximizing the sum rate in a secondary network, under a given outage probability at the primary user. The latter is evaluated by the secondary user by means of the 1-bit ACK/NACK feedback sent on the reverse link between the primary receiver and transmitter. In [86], a distributed power allocation scheme for outage probability minimization in multiple-input multiple-output (MIMO) interference channels is proposed. The optimization problem is modeled as a non-cooperative game with mixed strategies, where the probability of playing a certain strategy is updated with a reinforcement learning rule based on the ACK/NACK feedback. The major contribution of this chapter is a novel iterative and distributed algorithm that allows the transmitters to converge to the equilibrium point using only the limited feedback in the form of ACK or NACK over packet-oriented transmission links. The proposed solution relies on a learning algorithm that is reminiscent of the scheme proposed in [83] and allows each transmitter to locally update an estimate of the received SINR while converging towards the equilibrium. This is achieved applying a simple updating rule completely unaware of the structure of the underlying game and requiring knowledge of local information only. Numerical results are used to assess the convergence and performance (in terms of number of iterations required) of the proposed solution in the uplink of a small-cell network.

6.2 System model and problem formulation

We consider a K -user Gaussian interference channel, in which there are K transmitter-receiver pairs sharing the same Gaussian channel, that might represent a time or frequency bin. The transmission is organized in frames with each frame counting a certain number of packets, each one composed of M data symbols of unity-energy. We call $x_k(m)$ the m th data symbol of transmitter k within a generic packet and denote $\mathbf{x}_k = [x_k(1), x_k(2), \dots, x_k(M)]^T$. Each \mathbf{x}_k is encoded at a rate $r_k \in \mathcal{R}_k$ with \mathcal{R}_k being the set of feasible rates and is transmitted with an amount of power $p_k \in \mathbb{R}_+$. The channel is assumed to be constant over a frame and to change independently from one frame to another (block-fading channel). We assume that the transmitters do not have any a-priori knowledge of the channel.

Letting $h_{k,i}$ denote the channel coefficient between transmitter i and receiver k over a generic packet, the vector $\mathbf{y}_k \in \mathbb{C}^{M \times 1}$ received at the k th receiver within the generic packet can be written as

$$\mathbf{y}_k = \sum_{i=1}^K h_{k,i} \sqrt{p_i} \mathbf{x}_i + \mathbf{w}_k \quad (6.1)$$

where $\mathbf{w}_k \sim \mathcal{CN}(0, \sigma^2 \mathbf{I}_M)$ accounts for the additive white Gaussian noise. The corresponding SINR is given by

$$\gamma_k = \frac{p_k |h_{k,k}|^2}{\sum_{i=1, i \neq k}^K |h_{k,i}|^2 p_i + \sigma^2}. \quad (6.2)$$

For later convenience, we call

$$\mu_k = \frac{|h_{k,k}|^2}{\sum_{i=1, i \neq k}^K |h_{k,i}|^2 p_i + \sigma^2} \quad (6.3)$$

the channel-to-interference-plus-noise ratio (CINR) and denote $\mathbf{p}_{-k} = [p_1, \dots, p_{k-1}, p_{k+1}, \dots, p_K]^T$ the vector collecting all the transmit power except that of transmitter k .

The aim of this study is to solve the following power minimization problem for any $k = 1, 2, \dots, K$

$$\begin{aligned} \min_{p_k \in \mathbb{R}_+} \quad & p_k \\ \text{subject to} \quad & \gamma_k \geq \bar{\gamma}_k \end{aligned} \quad (6.4)$$

where $\bar{\gamma}_k > 0$ are given quality-of-service (QoS) requirements. The interplay among the pairs through (6.2) makes (6.4) a multidimensional optimization problem in which each transmitter-receiver pair aims at unilaterally choosing the minimum transmit power p_k so as to full fill its own requirement. In doing this, each pair affects the choice of all other pairs as well.

6.3 Game formulation

The natural framework to study the solution of problems in the form of (6.4) is non-cooperative game theory [6]. Interpreting (6.4) as a game \mathcal{G} leads to the definition of the tuple $\mathcal{G} = (\mathcal{K}, \{\mathcal{A}_k\}, \{u_k\})$, where $\mathcal{K} = \{1, 2, \dots, K\}$ is the set of players, \mathcal{A}_k is the k th player's strategy set such that the constraints in (6.4) are satisfied, and $u_k = p_k$ is the utility function of player k . Note that player k 's action set depends on the actions of the other players, i.e., $\mathcal{A}_k = \mathcal{A}_k(\mathbf{p}_{-k})$ due to the presence of coupling constraints. In this case, the solution concept to be used is the generalized Nash equilibrium (GNE) that is defined as the point collecting all the system states stable to unilateral deviations [87]. The GNE of the power allocation problem in (6.4) has been extensively studied in the literature. The main results are summarized in the following theorem.

Theorem 1 *If the problem (6.4) is feasible, then there exists a unique power allocation vector $\mathbf{p}^* = [p_1^*, p_2^*, \dots, p_K^*]^T$ that is the GNE of the game \mathcal{G} . The elements of \mathbf{p}^* are the solutions to the following fixed-point system of equations:*

$$p_k^* = \text{BR}(\mathbf{p}_{-k}^*) = \frac{\bar{\gamma}_k}{\mu_k(\mathbf{p}_{-k}^*)} \quad \forall k \in \mathcal{K} \quad (6.5)$$

where the operator BR stands for the best-response of user k to given other users' strategy \mathbf{p}_{-k}^* and μ_k is defined in (6.3).

As shown in [88], a necessary and sufficient condition for which problem (6.4) is feasible is that $\rho_{\mathbf{G}} < 1$ where $\rho_{\mathbf{G}}$ is the spectral radius of matrix $\mathbf{G} \in \mathbb{R}^{K \times K}$, whose (k, i) th element is computed as

$$[\mathbf{G}]_{k,i} = \begin{cases} 0 & k = i \\ \frac{\bar{\gamma}_k |h_{k,i}|^2}{|h_{k,k}|^2} & k \neq i. \end{cases} \quad (6.6)$$

The existence and the uniqueness follows observing that the best-response is a standard function [89], [90].

In addition to this, using the results of [89] it follows that the optimal point \mathbf{p}^* can be reached via a distributed iterative power control policy based on best response dynamics according to which every player k updates its power (strategy) $p_k^{(n+1)}$ at time $n + 1$ as

$$p_k^{(n+1)} = \frac{\bar{\gamma}_k}{\mu_k(\mathbf{p}_{-k}^{(n)})} \quad (6.7)$$

with $\mu_k(\mathbf{p}_{-k}^{(n)})$ being the CINR within the transmission time n .

6.4 Distributed algorithm

Using (6.2), we may rewrite (6.7) as

$$p_k^{(n+1)} = p_k^{(n)} \frac{\bar{\gamma}_k}{\gamma_k(\mathbf{p}^{(n)})} \quad (6.8)$$

from which it follows that the computation of $p_k^{(n+1)}$ for a given $\mathbf{p}_{-k}^{(n)}$ requires knowledge of $\gamma_k(\mathbf{p}^{(n)})$. Most of the existing works rely on the assumption that each transmitter has perfect knowledge of it. Unfortunately, this assumption does not hold true in practical applications and the only way for the transmitter to acquire this knowledge is through a return control channel. Although possible, however, this solution is not compliant with current cellular standards in which the receiver only sends back an ACK ($f_k = 0$) whenever is able to correctly decode the packet and a NACK ($f_k = 1$) otherwise. Assume that a maximum likelihood (ML) decoder is used at the receiver and denote by $\hat{\mathbf{x}}_k \in \mathbb{C}^{M \times 1}$ the ML estimate of \mathbf{x}_k obtained from \mathbf{y}_k . Therefore, an ACK or NACK is sent to transmitter k with probability

$$\Pr \{f_k = \bar{f}\} = \begin{cases} \varepsilon_k(\mu_k, r_k, p_k) & \bar{f} = 1 \\ 1 - \varepsilon_k(\mu_k, r_k, p_k) & \bar{f} = 0 \end{cases} \quad (6.9)$$

where $\varepsilon_k(\mu_k, r_k, p_k)$ stands for the ML decoding error probability, which is clearly a function of the CINR μ_k , the transmit power p_k and the encoding rate r_k . In particular, assuming Gaussian random codes a generic $\varepsilon_k(\mu_k, r_k, p_k)$ can be approximated as follows [91]

$$\varepsilon_k(\mu_k, r_k, p_k) \approx \exp \left(M \rho \left[r_k \log 2 - \frac{1}{2} \log \left(1 + \frac{\gamma_k}{1 + \rho} \right) \right] \right)$$

where $\rho \in [0, 1]$ is the union bound parameter and M is the number of data symbols per packet encoded at a rate of r_k bits/symbol.

Algorithm 1 Distributed resource allocation algorithm

1. At $n = 1$ for any $k \in \mathcal{K}$, choose a feasible $r_k^{(1)} \in \mathcal{R}_k$ and an arbitrary estimate $\hat{\mu}_k^{(1)}$. Then, set $\hat{p}_k^{(1)} = \bar{\gamma}_k / \hat{\mu}_k^{(1)}$;
2. At $n = 2, 3, \dots$ for any $k \in \mathcal{K}$

(a) compute

$$\hat{\mu}_k^{(n)} = \hat{\mu}_k^{(n-1)} + \frac{f_k^{(n-1)} - \varepsilon(\hat{\mu}_k^{(n-1)}, p_k^{(n-1)}, r_k^{(n-1)})}{(n-1)^\beta \varepsilon'(\hat{\mu}_k^{(n-1)}, p_k^{(n-1)}, r_k^{(n-1)})}$$

and set

$$r_k^{(n)} = \arg \max_{r \in \mathcal{R}_k} \Phi(\hat{\mu}_k^{(n)}, p_k^{(n-1)}, r)$$

(b) update

$$p_k^{(n)} = \frac{\bar{\gamma}_k}{\hat{\mu}_k^{(n)}}$$

Based on the above considerations, we propose an iterative and distributed two-step algorithm that allows each transmitter-receiver pair to reach the GNE of the game only exploiting the knowledge of $\{p_k^{(n-1)}, r_k^{(n-1)}, f_k^{(n-1)}\}$. The first step is reminiscent of the iterative solution proposed in [83] and aims at locally computing a reliable estimate $\hat{\mu}_k^{(n)}$ of $\mu_k^{(n)}$. Mathematically, $\hat{\mu}_k^{(n)}$ is obtained as follows

$$\hat{\mu}_k^{(n)} = \hat{\mu}_k^{(n-1)} + \frac{f_k^{(n-1)} - \varepsilon(\hat{\mu}_k^{(n-1)}, p_k^{(n-1)}, r_k^{(n-1)})}{(n-1)^\beta \varepsilon'(\hat{\mu}_k^{(n-1)}, p_k^{(n-1)}, r_k^{(n-1)})} \quad (6.10)$$

where β is a design parameter that regulates the convergence speed of the iterative procedure. The larger β , the smaller the convergence time. In addition, ε' denotes

the derivative of ε with respect to μ and is given by

$$\varepsilon' = \frac{-M\rho p_k}{2(1 + \rho + \mu_k p_k)} \varepsilon_k$$

where we have dropped the functional dependence from (μ_k, r_k, p_k) for notational simplicity. The value of $\hat{\mu}_k^{(n)}$ is then used to update $r_k^{(n)}$ according to:

$$r_k^{(n)} = \arg \max_{r \in \mathcal{R}_k} \Phi(\hat{\mu}_k^{(n)}, p_k^{(n-1)}, r) \quad (6.11)$$

where

$$\Phi(\hat{\mu}_k^{(n)}, p_k^{(n-1)}, r) = \frac{[\varepsilon'(\hat{\mu}_k^{(n)}, p_k^{(n-1)}, r)]^2}{\varepsilon(\hat{\mu}_k^{(n)}, p_k^{(n-1)}, r)[1 - \varepsilon(\hat{\mu}_k^{(n)}, p_k^{(n-1)}, r)]}$$

is the Fisher information associated to the random variable f_k . Following the same arguments of [83], it can be proven that for any unbiased estimator based on n ACK/NACK, the estimation error variance of $\mu_k^{(n)}$ is lower bounded by the reciprocal of the cumulative Fisher information given by $\sum_{i=1}^n \Phi(\mu_k^{(i)}, p_k^{(i-1)}, r_k^{(i)})$. The estimate $\hat{\mu}_k^{(n)}$ is eventually used in the last step for updating the transmit power as specified in (6.7). The main steps of the proposed solution are summarized in **Algorithm 1** where $f_k^{(1)}$ is the ACK/NACK received after the first packet transmission.

Remark 1. *Observe that similarly to a reinforcement learning approach in which at each step the probability function is updated according to a certain rule and then a strategy is randomly played according to this probability, in the proposed solution the estimate of μ_k is updated through (6.10), but then, the strategy is deterministically played, exploiting the knowledge of the optimal solution of the game with complete information.*

Remark 2. *The analytical study of the convergence of the proposed algorithm is still much open. In the next section, we limit to assess the convergence of **Algorithm 1** by means of Monte Carlo simulations. Interestingly, it turns out that the proposed solution converges (within the required accuracy) whenever the game with complete information is feasible and thus the existence of the unique GNE point is guaranteed. Moreover, the convergence point is the same meaning that the same performance can be achieved despite the amount of required information is much lower. The only price to pay is a greater convergence time.*

6.5 Simulation results

The performance of the distributed algorithm is now assessed by means of an extensive simulation campaign. To this end, we consider the uplink of a small-cell network [92] consisting of up to $K = 6$ single-antenna small cells, each serving a single UE. We set $\bar{\gamma} = [0.5, 1, 1.5, 2, 2.5, 3]^T$ dB and assume that the coverage area of each small cell is circular with radius $R = 50$ m and minimum distance $R_{\min} = 5$ m. The small cells are randomly distributed over a $200 \times 50K$ area. Moreover, we consider a system in which the large-scale fading is dominated by the path-loss. This amounts to saying that the channel coefficients $h_{k,i}$ can be modeled as

$$h_{k,i} = \frac{\bar{d}}{d^\alpha} \bar{h}_{k,i} \quad \text{for } d \geq R_{\min} \quad (6.12)$$

where $\bar{h}_{k,i} \sim \mathcal{CN}(0, 1)$ accounts for the small-scale fading, d is the distance between transmitter k and receiver i , $\alpha \geq 2$ is the path-loss exponent and $\bar{d} > 0$ is a constant that regulates the channel attenuation at distance R_{\min} [93]. We set $\bar{d} = 10^{-3.53}$ and $\alpha = 3.76$. We assume that the channel coefficients maintain constant in time. Moreover, the noise power level is set to $\sigma^2 = -100$ dBm and each packet is assumed to contain $M = 500$ symbols. The proposed algorithm is initialized for any $k \in \mathcal{K}$ as follows: $r_k^{(1)} = 1$ bit/s/Hz, $\hat{\mu}_k^{(1)} = |h_{k,k}|^2/\sigma^2$ and $p_k^{(1)} = \bar{\gamma}_k/\hat{\mu}_k^{(1)}$. Figure 6.1 illustrates the values of $\gamma_k^{(n)}$ (dashed lines) measured at the BS as a function of the number n of transmitted packets in a scenario of $K = 4$ small cells when $\beta = 0.9$. The target SINRs $\bar{\gamma}_k$ for $k = 1, 2, \dots, K$ (continuous lines) are also reported for comparison. Figure 6.2 reports also the variations of $p_k^{(n)}$ (dashed lines) as n increases together with the power (continuous lines) required at the GNE point. The results of Fig. 6.5 illustrates the behavior of $\gamma_k^{(n)}$ when $K = 4$ and β is set to 0.5. As expected, reducing β allows terminals to achieve convergence in a smaller number of packets. However, this is achieved at the price of larger variations around the target values $\{\bar{\gamma}_k\}$. Figure 6.6 shows $\gamma_k^{(n)}$ when K changes during the execution of the algorithm. We start with $K = 4$ at $n = 1$ and assume that two new small cells become active at $n = 300$ and inactive again at $n = 600$ and $n = 800$. As seen, the algorithm is very robust to network perturbations and guarantees fast convergence in a dynamic scenario.

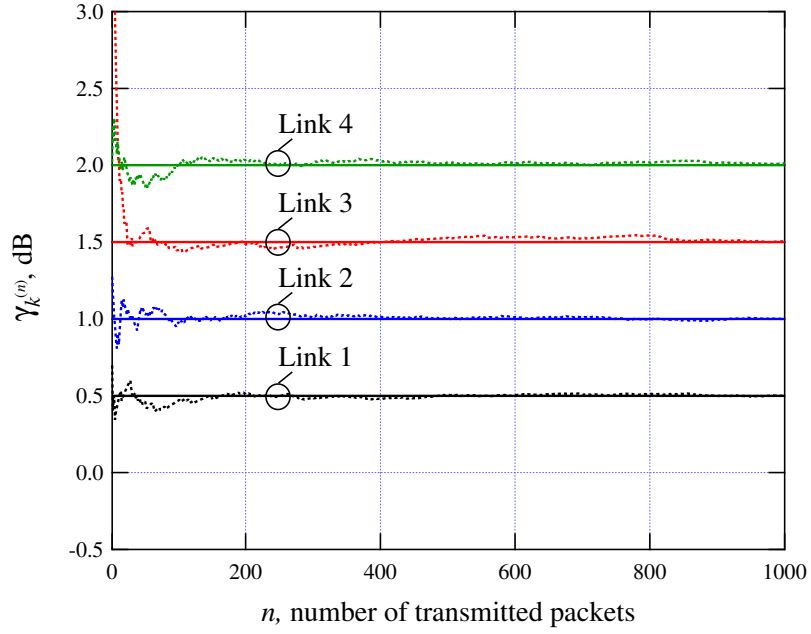


Figure 6.1: SINR vs. number of packets when $K = 4$ and $\beta = 0.9$.

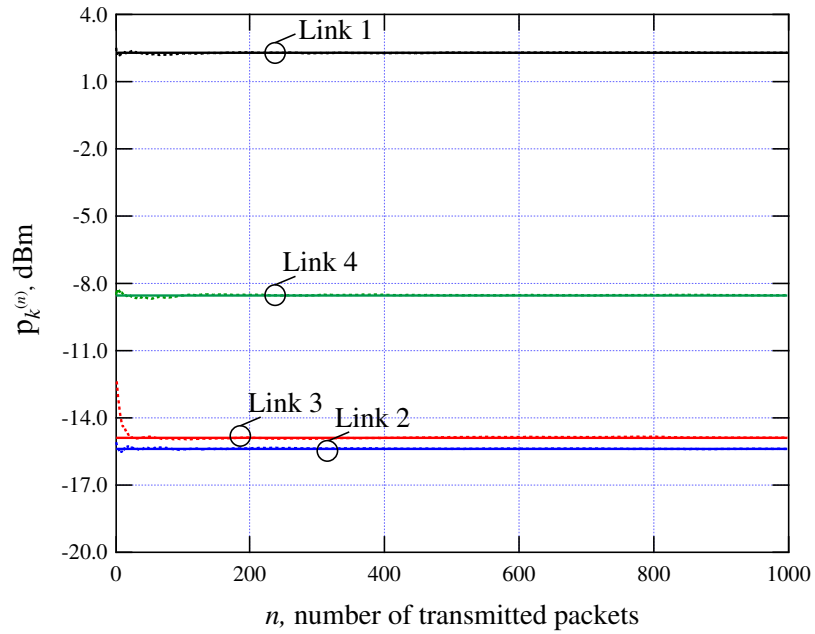


Figure 6.2: Transmit power vs. number of packets when $K = 4$ and $\beta = 0.9$.

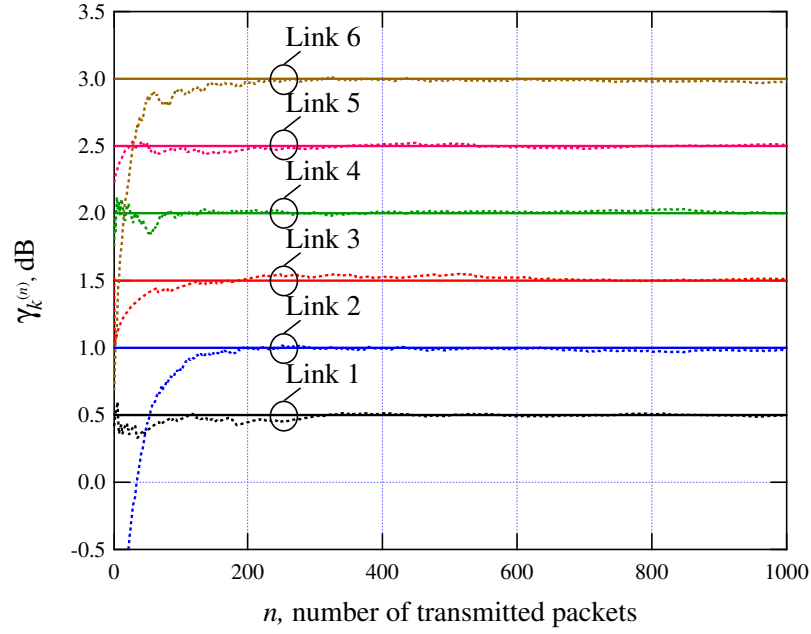


Figure 6.3: SINR vs. number of packets when $K = 6$ and $\beta = 0.9$.

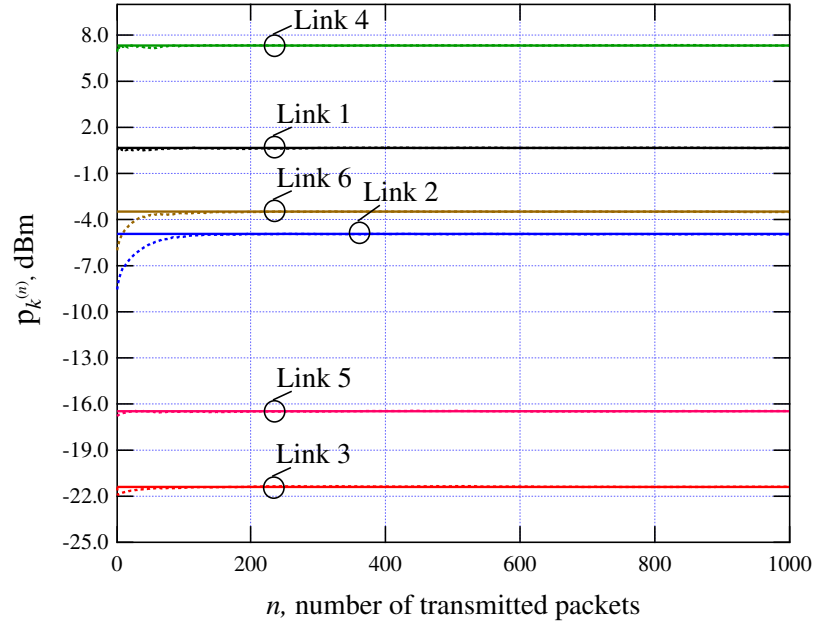


Figure 6.4: Transmit power vs. number of packets when $K = 6$ and $\beta = 0.9$.

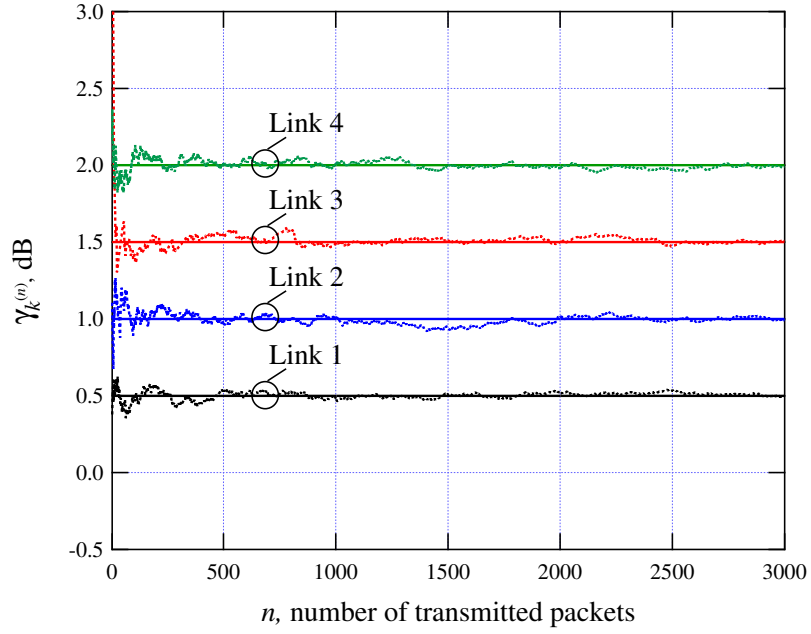


Figure 6.5: SINR vs. number of packets when $K = 4$ and $\beta = 0.5$.

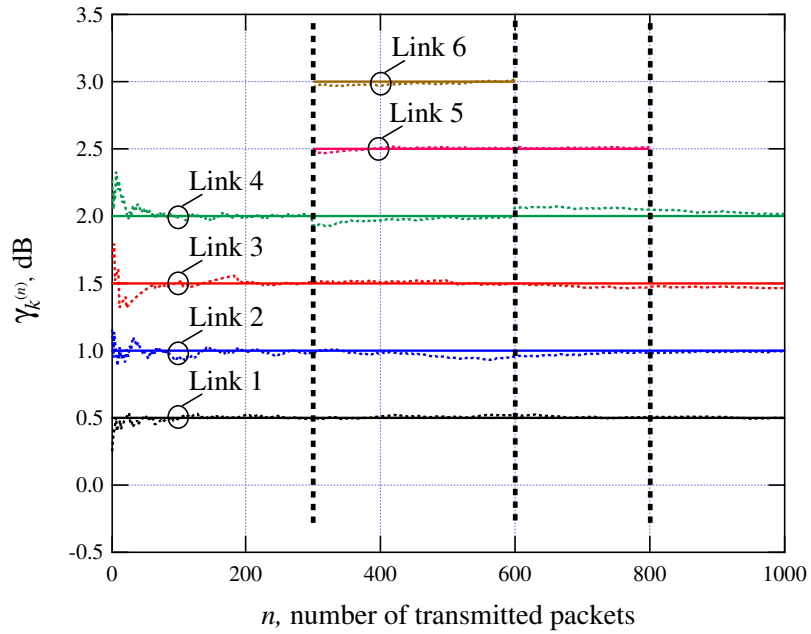


Figure 6.6: SINR vs. number of packets with $\beta = 0.9$.

6.6 Concluding remarks

In this chapter, we have focused on the problem of selfishly minimizing the power consumption while satisfying target SINR constraints in interference channels characterized by single-antenna transmitter-receiver pairs operating over the same frequency band or time slot. In particular, we have first modeled the problem as a non-cooperative game with perfect CSI and then we have solved it assuming that each transmitter has no knowledge about the propagation channel but could only exploit the ACK or NACK feedbacks generated at the link layer from the receiver. This choice has been motivated by the fact that it is compliant with many wireless communication standards and avoids the need of introducing a suitably designed return control channel. Accordingly, we have proposed an iterative and distributed algorithm inspired by best response dynamics in which (at each step) every transmitter updates its power exploiting a local estimate of its current SINR at the receiver. The latter is learned step by step via an updating rule based on the 1-bit feedback information given by ACK or NACK. The performance of the proposed solution have been evaluated by means of numerical results in the uplink of a small cell network. It turns out that the algorithm converges reasonably fast to the GNE point of the underlying game with perfect CSI.

Chapter 7

An Efficient Receiver Structure for Underwater Acoustic Communications

7.1 Introduction

Underwater acoustic (UWA) communication systems have attracted considerable attention in recent years due to the growing interest for issues related to exploration, surveillance and exploitation of the submarine environment (e.g. [94]– [99]). Most of these applications require some form of wireless communication capability between submerged terminals such as autonomous underwater vehicles (AUVs), platform/-mother ships, nodes of underwater networks etc. As is well known, the UWA multi-path channel is plagued by several impairments, notably: *i*) severe time dispersion due to the low sound propagation speed with consequent possible distortion of the received waveform, *ii*) for the same reason, amplification of Doppler shifts/rates associated to relative movements of terminals, *iii*) large propagation delays, *iv*) low-pass behavior of the propagation channel caused by sound absorption, leading to strong limitation of bandwidth usage. These factors considerably limit transmission rates and coverage of UWA links in comparison with their electromagnetic radio counterparts and call for the search of more specific and robust signaling schemes. Comprehensive accounts

of the above issues along with presentation and discussion of specific transmission schemes can be found e.g. in [96] - [99] and references therein.

Recently, a novel interesting spread-spectrum transmission technique was proposed in [100] and applied to the UWA channel. The basic idea is to employ a sawtooth-frequency-modulated waveform as signal carrier (termed S2C, sweep-spread carrier), with linear frequency ramps, such to facilitate separation at the receiver of the signal replicas collected from the various channel paths. Actually, since these replicas undergo different propagation delays, they are mapped to different positions on the frequency axis when the received signal is down-converted to baseband using a locally-generated copy of the S2C synchronized to the strongest path. A proper design of the signal parameters permits to space the spectral replicas associated with the various paths far enough from one another so as to avoid their overlap. It is therefore possible to single out the strongest path with no interference from the others, thus canceling multipath-induced distortion.

Field trials have shown that this technique offers performance margins with respect to other conventional modulation formats employed on UWA channels. However the cited basic scheme is still amenable to significant improvements. In the following we propose and discuss an advanced receiver structure capable of enhancing the power efficiency of the scheme in [100] through exploitation of the energy received from *all* non-negligible acoustic paths rather than only from the strongest path. This goal can be achieved by first identifying the strongest paths, then performing parallel elaboration for each path and finally combining the decision metrics from each processing branch. This approach is similar to that used for the reception of direct-sequence spread-spectrum (DS-SS) signals over time-dispersive wireless links, known as “rake receiver” [5], but the context considered here is quite different and more demanding as we have now to face the peculiar problems relating to both the non-conventional format of the S2C signal and the rather adverse UWA propagation environment. In particular, one of the critical issues to be addressed here is related to the joint recovery of carrier and clock references for each of the signal replicas involved.

A real-time hardware version of the modem, complete of synchronization functions, was implemented in laboratory and its behavior was assessed over standard UWA channel emulators and compared to that exhibited by the traditional strongest-path-based scheme in terms of bit error rate (BER) vs. signal-to-noise ratio.

7.2 Signal and channel models

Now we briefly review the S2C signal format referring the reader to [100] for further details. We assume information is transmitted in the form of data packets, each starting with a preamble of P known pilot symbols, to be employed for carrier and symbol synchronization/tracking, followed by a payload of D symbols. Letting T denote the symbol spacing, the packet length is $T_B = (P + D)T$. The number of packets and the instants for their transmission depend on both the amount of information to be transferred and the specific link protocols.

Focusing then on a generic packet, the signal at baseband, prior to spectral expansion and frequency up-conversion, is a conventional linearly-modulated waveform

$$s(t) = \sum_{i=0}^{P+D-1} a_i g(t - iT) \quad (7.1)$$

where $\mathbf{a} \triangleq [a_0, \dots, a_{P+D-1}]^T = [p_0, \dots, p_{P-1}, d_0, \dots, d_{D-1}]^T$ denotes the vector of (differentially-encoded) QPSK symbols in the packet, and $g(t)$ is a root-raised-cosine pulse with roll-off factor α . In particular, the pseudo-random sequence $\mathbf{p} \triangleq [p_0, \dots, p_{P-1}]^T$ of pilot symbols is common to all packets, while the sequence $\mathbf{d} \triangleq [d_0, \dots, d_{D-1}]^T$ represents a specific data segment.

After spectral spreading and frequency up-conversion, the bandpass signal to be fed to the acoustic projector can be written as

$$x(t) = \Re\{s(t)c(t)\} \quad (7.2)$$

$c(t)$ denoting a frequency-modulated carrier achieving both frequency conversion and bandwidth expansion, as follows

$$c(t) = \exp\{j2\pi[f_L\tau(t) + m\tau^2(t)]\} \quad (7.3)$$

where $\tau(t)$ is a sawtooth-shaped periodic sweep function, with period T_{sw}

$$\tau(t) = t - \left\lfloor \frac{t}{T_{sw}} \right\rfloor T_{sw} \quad (7.4)$$

$\lfloor z \rfloor$ being the largest integer not exceeding z . In (7.3), f_L represents the lower limit of the frequency ramps, while $2m$ is the ramp slope. The instantaneous carrier frequency

during a ramp is proportional to the derivative of the argument of the exponential in (7.3)

$$f_i(t) = f_L + 2m \left(t - \left\lfloor \frac{t}{T_{sw}} \right\rfloor T_{sw} \right). \quad (7.5)$$

It follows that the upper frequency limit is $f_H = f_L + 2mT_{sw}$. The limits f_L and f_H , along with the sweep interval T_{sw} , usually taken an integer multiple of the symbol spacing, are key design parameters as they define the slope $2m = \frac{f_H - f_L}{T_{sw}}$ of the ramps and characterize the ability of the receiver to resolve the multipath channel structure (i.e., to separate the signal replicas arriving from the various paths).

After spreading and frequency up-conversion, the signal bandwidth amounts to approximately $B \approx f_H - f_L$, i.e., it is expanded by a factor (*spreading factor*)

$$\mathcal{M} \triangleq \frac{f_H - f_L}{\frac{1+\alpha}{T}} \quad (7.6)$$

with respect to a conventional narrowband signal, \mathcal{M} usually being much greater than unity.

A general expression of the multipath time-varying UWA channel impulse response is as follows

$$r_c(t, t_0) = \sum_{k=0}^{K(t_0)-1} h_k(t_0) \delta[t - t_0 - \tau_k(t_0)] \quad (7.7)$$

where $K(t_0)$ is the number of (non-negligible level) paths and $h_k(t_0)$, $\tau_k(t_0)$ are the (complex-valued) gain and delay of the k -th path, respectively, all evaluated at the instant of application of the impulse $t = t_0$. In the following we assume that the channel variations are negligible in a time span comparable to the packet length, so that the information about the channel parameters in (7.7), estimated from the packet preamble, can be considered reliable throughout the whole payload segment. This is not a severe constraint since transmission on the UWA link is normally preceded by a procedure of adjustment of the transmission parameters to the channel conditions. Accordingly, the dependence of the model in (7.7) on t_0 can be dropped and all channel parameters can be regarded as random variables instead of random processes. Therefore the received waveform can be written as

$$y(t) = \sum_{k=0}^{K-1} y_k(t) + w(t) \quad (7.8)$$

where $w(t)$ is AWGN of double-sided spectral density $N_0/2$, accounting for both external and internal disturbance sources affecting the receiver, and $y_k(t)$ is the waveform received through the k -th path, i.e., scaled by the coefficient h_k and delayed by τ_k

$$y_k(t) = \Re\{h_k s(t - \tau_k)c(t - \tau_k)\}. \quad (7.9)$$

7.3 Modem architecture

A functional block diagram of the S2C modem is depicted in Fig. 7.1. The transmitter section consists of a standard S2C modulator similar to that discussed in [100]. The information bits are fed to a BCH encoder followed by a DQPSK symbol mapper. The resulting symbol sequence is used to build the data packet (function not detailed in the figure) that is passed through the shaping filter and finally applied to the S2C frequency upconverter.

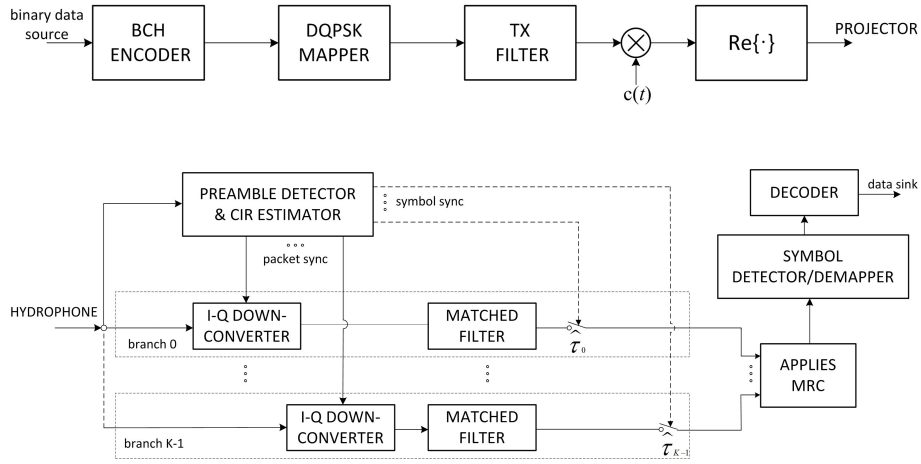


Figure 7.1: *Modem architecture.*

The receiving section includes a block for preamble detection and channel impulse response (CIR) estimation, whose task is to identify, for each packet, the times of arrival of the preamble from the K strongest paths and also to estimate the (complex-valued) gains of these paths. This leads to the receiver architecture indicated in Fig. 7.1, wherein each of the K parallel branches is used to process the signal received from a single path. Specifically, with regard to the k -th branch, the input is applied

to a in-phase and quadrature converter which multiplies it by a replica of the S2C waveform synchronized with that received from the k -th path. In this way the signal spectrum relative to that path is despread and exactly converted to baseband, while subsequent matched filtering removes interference from the other paths provided that their spectra do not overlap the “good” spectrum at baseband, i.e., their differential propagation delays with respect to the k -th path are sufficiently large. As next step, the matched filter output is sampled at symbol rate at the instants $iT + \hat{\tau}_k$, where $\hat{\tau}_k$ is an estimate of τ_k provided by the CIR estimator and, assuming exact ISI cancellation, from (7.1) and (7.8)-(7.9) the generic sample takes on the form

$$v_{k,i} = h_k a_i + w_{k,i} , \quad (7.10)$$

the last term denoting the noise sample generated from $w(t)$ in (7.8) after the above processing steps through the k -th branch.

Finally, the K samples relevant to the symbol a_i are combined according to the maximal ratio combining (MRC) criterion [5] prior to being fed to the symbol detector and the decoder. With regard to the MRC block, for the moment we observe that a sufficient condition for the noise terms $\{w_{k,i}\}_{k=0}^{K-1}$ to be mutually uncorrelated is that the differential delays between the various paths obeys the same conditions allowing separation of the respective signal replicas.

It is noted that when $K = 1$ the receiver structure reduces to that discussed in [100] where only the strongest path is processed.

7.4 Timing and channel estimation

As mentioned earlier, the first operation to be accomplished at the receiver site is estimation of the timing of arrival of the signal replicas propagating along the channel paths. This permits to synchronize locally generated copies of the S2C waveform with those associated with the K strongest paths and then proceed to separate the signal replicas received from these paths. Another important related task is estimation of the complex-valued channel gains so as to identify the strongest paths and correctly apply the MRC technique.

Both the above operations are carried out by means of a correlator, as is now briefly outlined. Let $s_P(t)$ denote the baseband continuous-time version of the preamble

separated from the payload, as follows

$$s_P(t) = \sum_{i=0}^{P-1} p_i g(t - iT) \quad (7.11)$$

and also let

$$x_T(t) = s_P(t)c(t) \quad (7.12)$$

denote the complex-valued bandpass version of the preamble incorporating both frequency up-conversion and bandwidth expansion. It is noted from (7.2) that the real part of (7.12) represents the transmitted preamble.

Using for simplicity continuous-time notation, the task of the correlator is to calculate the inner product between the template function (7.12) and a newly received segment of the input waveform, and then take its squared modulus, as follows

$$z(t) = |r(t)|^2, \quad t \in \mathcal{T} \quad (7.13)$$

where

$$r(t) = \int_0^{T_P} y(t + \tau - T_P) x_T^*(\tau) d\tau, \quad (7.14)$$

\mathcal{T} is a time interval in which the preamble is expected to be received and $T_P = PT$ is the preamble length. The receiver stores the functions (7.13)-(7.14) in memory along with the raw received waveform $y(t)$ for subsequent processing.

As can be easily verified, if path delays are sufficiently spaced from one another and the signal-to-noise-plus-interference ratio on the paths is high, the squared correlation $z(t)$ exhibits a definite peak in correspondence of each of the delays $\{\tau_k\}$. Figure 7.2 shows an example of such a function.

Specifically, assuming for a moment that the receiver is driven by a single noiseless signal replica received from the k -th path (see (7.9)), it is found that (7.13) peaks at the instant $T_P + \tau_k$, and the corresponding value for the inner product (7.14) is

$$r(T_P + \tau_k) = \frac{E_{S_P}}{2} h_k, \quad (7.15)$$

where $E_{S_P} = \int_0^{T_P} |s_P(\tau)|^2 d\tau$ is the energy of $s_P(t)$. From (7.15) it is seen that at the instant where the squared correlation peaks the inner product yields a value proportional to the path gain h_k , while the squared peak level is proportional to $|h_k|^2$. Therefore (7.14) provides all information necessary for path sorting, ramp synchronization and implementation of the MRC detector.

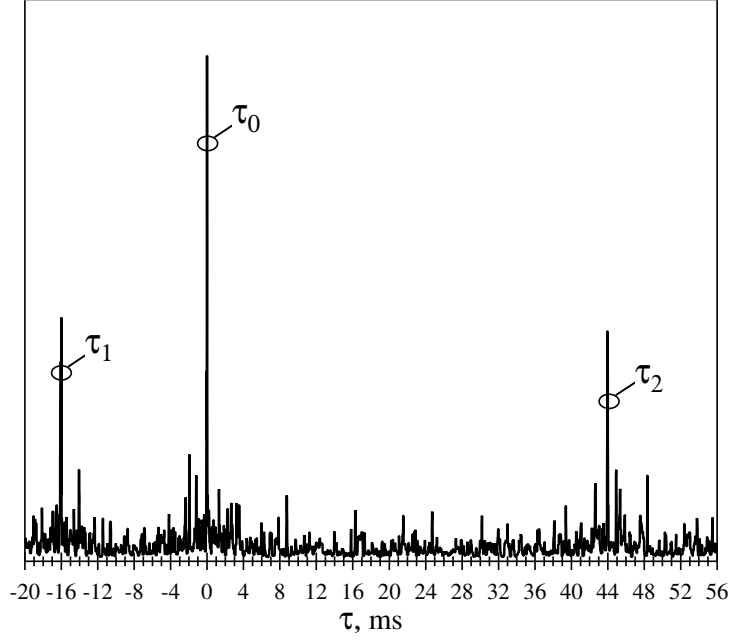


Figure 7.2: A sample correlation function (square modulus). The vertical scale is arbitrary.

Collecting the above, once correlation (7.13) has been calculated, a maximum search procedure must be initiated to obtain an estimate of the delay associated to each preamble replica arriving at the receiver. In particular, the time shift associated to the strongest replica (assumed relevant to the path of index zero) is obtained as

$$\hat{\tau}_0 = \arg \max_{\substack{z(t) > \lambda \\ t \in \mathcal{T}}} z(t) \quad (7.16)$$

where λ is a proper threshold affecting the detector performance. The time shifts associated to other paths of significant gain are identified by looking for the other local maxima of $z(t)$, using for instance the following iterative approach

$$\hat{\tau}_i = \arg \max_{\substack{z(t) > \lambda \\ t \in \mathcal{T} \\ t \notin \mathcal{I}_i}} z(t), \quad i = 1, 2, \dots, K - 1 \quad (7.17)$$

where \mathcal{I}_i denotes a set of subintervals of \mathcal{T} centred around the values of delay already identified through step $i - 1$, that must be excluded from the search at the current

step i , i.e.

$$\mathcal{I}_i = \{(\hat{\tau}_0 - T_{cor}, \hat{\tau}_0 + T_{cor}) \cup \dots \cup (\hat{\tau}_{i-1} - T_{cor}, \hat{\tau}_{i-1} + T_{cor})\}. \quad (7.18)$$

In this way the K strongest paths are orderly identified along with their delays. As for the width $2T_{cor}$ of the subintervals in \mathcal{I}_i , it has to be adjusted keeping into account the values selected for the main transmission parameters, notably T_{sw} and the frequency limits of the ramps in $c(t)$. Accordingly, $2T_{cor}$ should not be too large to avoid missing useful multipath components, nor too small to prevent secondary lobes of strong correlation peaks in (7.13) from being misdetected as independent peaks.

Furthermore, the value of λ should be set by trading off false against missed detection probabilities, with reference to limit conditions characterized by the least operating signal-to-noise ratios, e.g. when the distance between terminals is at the limit of coverage.

In addition to estimating the delay of the main paths of the UWA channel, the receiver must proceed to evaluate the relevant complex-valued path gains in view of their usage within the MRC block (see Fig. 7.1). As noted earlier, these gains are provided by (7.15) as a by-product of the same correlation algorithm employed for path delay estimation.

7.5 Design issues and hardware implementation

7.5.1 Conditions for path resolvability

Recalling the previous discussions, for the multi-branch receiver of Fig. 7.1 to work properly it is required that, for each branch, the signal spectrum converted to baseband does not collide with the spectra of the signal replicas being processed by the other branches. This allows the signal at baseband to be extracted by means of a simple (lowpass) matched filter. For these conditions to be met, it is necessary that the differential delays between all pairs of paths do not drop below a certain threshold. A further constraint is that the dispersion of delays must not exceed T_{sw} to avoid ambiguities in delay estimation.

More specifically, with no loss of generality we can treat $\{\tau_k\}_{k=0}^{K-1}$ as differential delays with respect to τ_0 , arranged in nondecreasing order, i.e., we set $\tau_0 = 0 \leq \tau_1 \leq \dots \leq \tau_{K-1}$. Then the constraints to be put on these differential delays are as follows

(see also [100])

$$\begin{cases} 2m\delta\tau_{min} \geq \frac{1+\alpha}{T} \\ -2m\delta\tau_{max} + f_H - f_L \geq \frac{1+\alpha}{T} \end{cases} \quad (7.19)$$

where $\delta\tau_{min} = \min_{0 \leq i, j \leq K-1} |\tau_i - \tau_j|$, $i \neq j$, is the minimum (absolute) differential path delay and $\delta\tau_{max} = \max_{0 \leq i, j \leq K-1} |\tau_i - \tau_j| = \tau_{K-1}$, $i \neq j$, is the maximum differential path delay, or channel time dispersion. Using (7.6) in (7.19) yields

$$\begin{cases} T_{sw} \leq \mathcal{M}\delta\tau_{min} \\ T_{sw} \geq \frac{\mathcal{M}}{\mathcal{M}-1}\delta\tau_{max} \end{cases} \quad (7.20)$$

For the existence of values of T_{sw} satisfying both the above conditions it is required that

$$1 \leq \frac{\delta\tau_{max}}{\delta\tau_{min}} \leq \mathcal{M} - 1. \quad (7.21)$$

The first inequality in (7.20) sets a lower limit to the absolute difference between the arrival times of any two signal replicas. When the difference exceeds this limit, the receiver is able to accurately resolve the channel multipath structure. Otherwise, when two received replicas are spaced too closely, after despreading they will overlap in the frequency domain, thus preventing their exact separation. On the other hand, the second inequality in (7.20) puts an upper limit to the differential path delays, approximately equal to T_{sw} when \mathcal{M} is large. Actually, a signal replica delayed more than T_{sw} with respect to the one traveling on the shortest path would generate a timing estimate affected by an ambiguity equal to an integer multiple of T_{sw} that could not be detected and recovered, with a negative impact on the MRC algorithm.

Figure 7.3 shows an example of power spectral density of the received signal after downconversion/despreading for a three-ray scenario, assuming that downconversion is carried out for the strongest path. Transmission parameters are the same as in the example of Fig. 7.2. Inspection of the figure reveals that in this case all paths are resolvable, and in particular the useful signal (whose spectrum lies around the origin) can be recovered by means of a lowpass filter, without (or with negligible) interference from the other replicas. The latter signal components, carrying useful power as well, can in turn be extracted by multiplication of the received waveform by properly delayed replicas of $c(t)$ followed by lowpass filtering. More specifically, from Fig. 7.3 it is seen that, in addition to the signal spectrum centered on the origin,

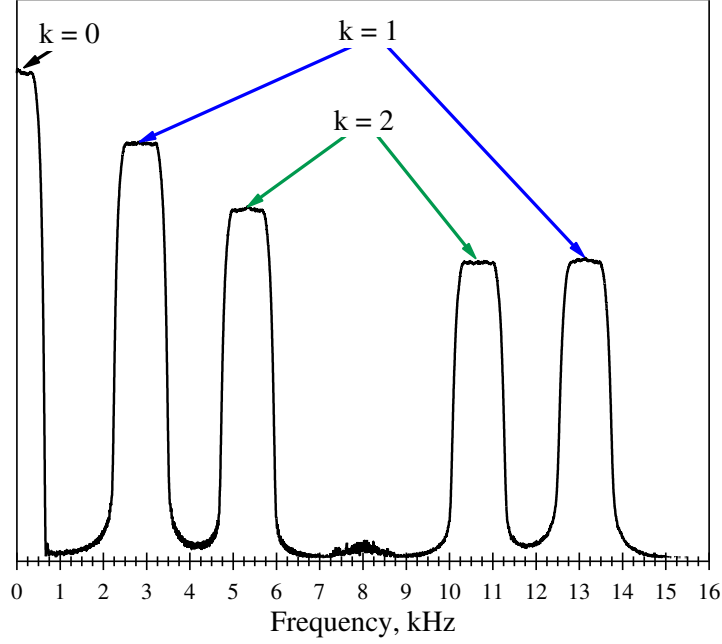


Figure 7.3: Power spectral density of the received signal after downconversion/despreading of the strongest path ($k = 0$). The vertical scale is arbitrary. The system parameters are the same as in Fig. 7.1 and are specified in Tabs. 7.1–7.3.

there are four other spectral replicas generated by the paths with delays τ_1 and τ_2 . Indeed, recalling (7.19), the k -th path gives rise to two spectral components, centered around the frequencies $2m\tau_k$ and $f_H - f_L - 2m\tau_k$, $k = 1, 2$. The actual values of these frequencies are specified in Tab. 7.2.

7.5.2 Merging branch outputs

As mentioned earlier, the receiver is made up of K parallel branches, designed to jointly extract and elaborate up to K replicas of the signal received from the multipath UWA channel. The k -th branch proceeds to downconvert/despread the received signal through its multiplication by $c(t - \hat{\tau}_k)$, where $\hat{\tau}_k$ is an estimate of the propagation delay on the k -th path. Assuming error-free delay estimates and exact resolvability of the signal on all branches, the sampled output of the k -th branch takes on the form (7.10). All branch outputs are then combined according to the MRC criterion,

as follows

$$q_i = \sum_{k=0}^{K-1} \hat{h}_k^* v_{k,i} \quad (7.22)$$

where \hat{h}_k is the estimate of the k -th path gain. The sequence of samples (7.22) is then fed to the decoder/data detector for further processing.

As mentioned in the Introduction, the above approach is reminiscent of that employed in the so-called “rake receiver” proposed for conventional DS-SS modulations [5], even though the context here is quite different from that envisaged in typical electromagnetic wireless links. However, if the K paths can be resolved, we can borrow from the rake receiver the expression of the asymptotic gain in power efficiency

$$G_R = \frac{\sum_{k=0}^{K-1} |h_k|^2}{|h_0|^2}, \quad (7.23)$$

that can be achieved with respect to the receiver operating on the single path of gain h_0 . This result has been confirmed experimentally.

7.5.3 Hardware implementation

Now we briefly present our real-time implementation of the modem architecture discussed in the foregoing sections. The testbed is based on *National Instruments* (NI) hardware [101], controlled by *LabView* (LV) applications. Specifically, we used the chassis *NI PXIe-1085* equipped with the controller *NI PXIe-8135* and the data acquisition board *NI PXIe-6361*. The entire system is controlled by a LV-based code that exploits the built-in functions provided in the *RF Communications* toolkit. The transmitter and receiver sections of the modem were both entirely implemented in hardware. Figure 7.4 shows the complete test bench used for the modem implementation, composed by the controller board within the chassis, a PC running *ad-hoc* LV application software and also a spectrum analyzer (Fig. 7.5 shows the spectrum of the transmitted signal generated during the test).

Focusing on the LV application running on the PC, Fig. 7.6 shows a section of the main control panel, from which the values of all physical-layer modem parameters can be set up. Figure 7.7 shows the analysis tool developed for the graphic control and performance evaluation of the entire transmission/reception chain. In particular, a sample plot of the instantaneous amplitude of the transmitted RF signal is presented

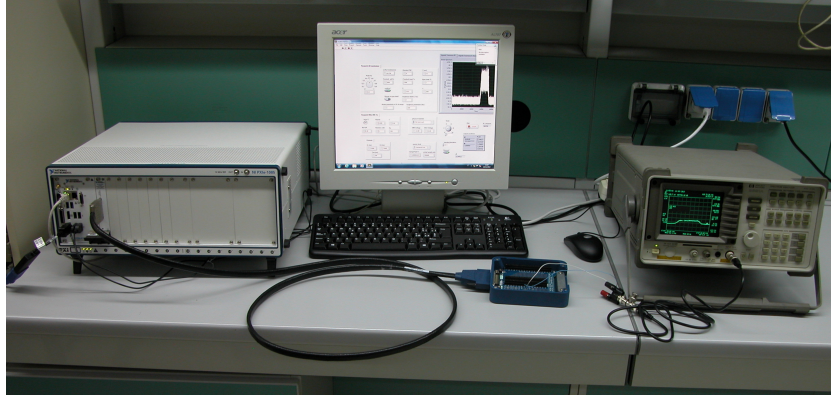


Figure 7.4: Test bench: NI chassis hosting controller and data acquisition board, PC with LabView, spectrum analyzer.

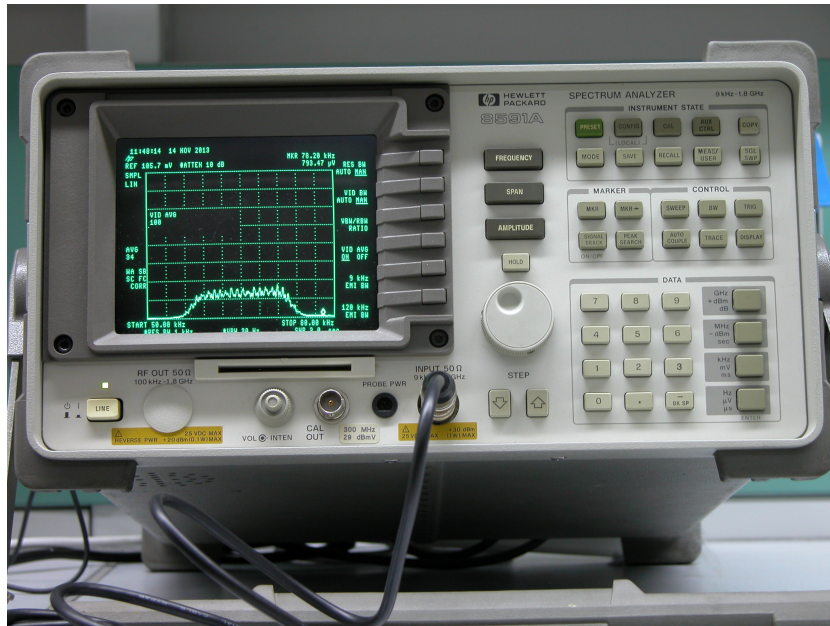


Figure 7.5: Transmitted signal displayed on spectrum analyzer.

on the left, while a noisy I/Q diagram at the symbol detector input is visible on the right. Further, Fig. 7.8 shows a fragment of LabView visual code developed for the implementation of synchronization circuitry. The discussion of details of the LabView code is out of the scope of this chapter and we limit ourselves to remark that this

block implements part of the algorithm for the search of correlation peaks, hence it is placed after the block computing the squared correlation (7.13) and generates the K timing estimates to be used in the receiver parallel branches visible in Fig. 7.1.

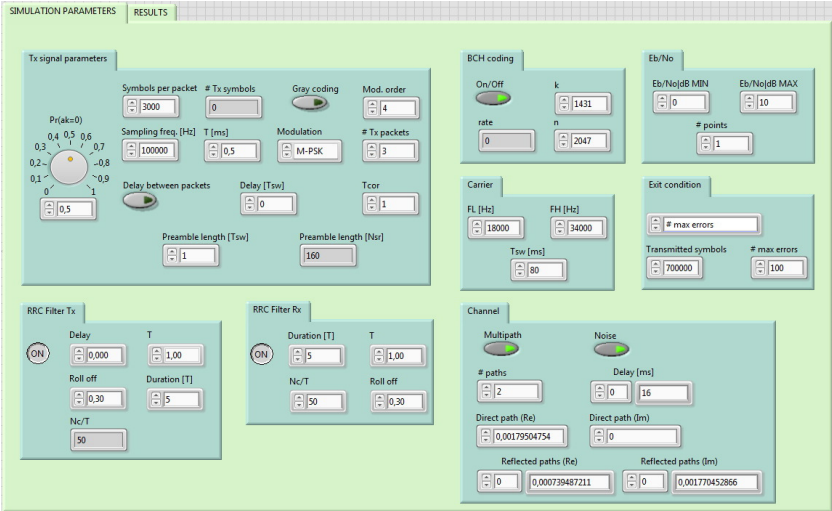


Figure 7.6: LabView control interface: particular of the main control panel.

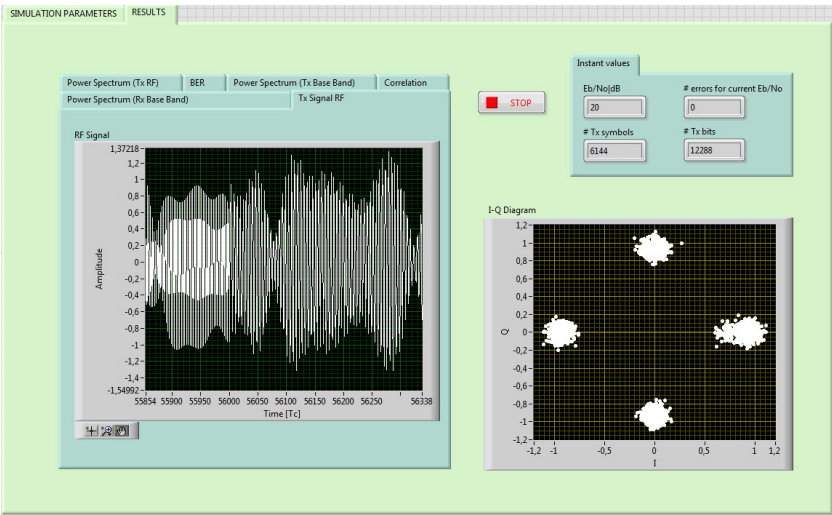


Figure 7.7: LabView control interface: particular of the analysis tools.

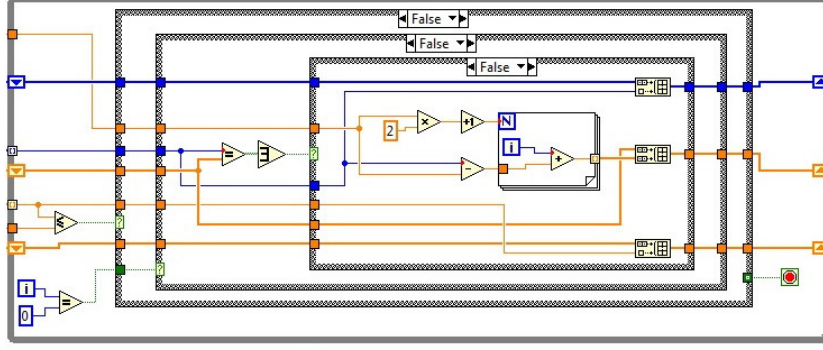


Figure 7.8: A functional block of the synchronization circuitry (LabView code).

7.6 Experimental results

The transmission architecture in Fig. 7.1 was implemented and assessed using the hardware testbed previously described, in conjunction with the software package *Bellhop* [102], a popular open-source simulator of the UWA environment. In particular, this simulator permits to identify both the coherent and non-coherent channel profile, i.e., for a fixed number of paths, their complex-valued (modulus and phase) gains, or simply their RMS values, vs. propagation delay, to be associated to an arbitrary UWA operating scenario.

For simplicity, in the following we limit our consideration to a single, albeit rather challenging, scenario characterized by shallow water (130 m) with sound speed profile vs. depth typical of the summer period and plotted in the left section of Fig. 7.9. The

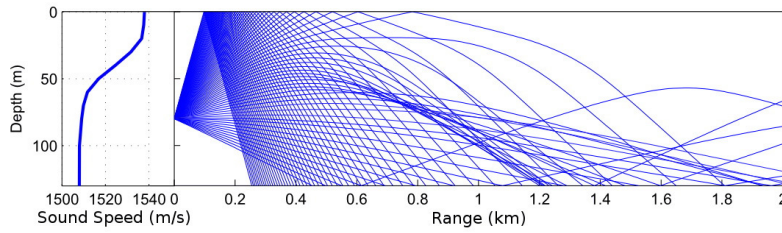


Figure 7.9: Ray tracing produced by Bellhop.

values assumed for the main geometric and acoustic parameters of the UWA scenario are summarized in Tab. 7.1, while Fig. 7.10 provides a pictorial representation of the

link geometry. In the right section of Fig. 7.9 we also show the curves produced by the Bellhop ray tracing tool, that can be used to calculate the channel power-delay profile.

Using the parameter values of Tab. 7.1, it is found that there are three dominant

TX depth	80 m
RX depth	5 m
Horizontal distance	500 m
Bottom type	gravel
Bottom depth	130 m
Surface	sea state 0
Sound speed profile	see Fig. 7.9
Center frequency	26 kHz
TX launching angles	$-60^\circ : +60^\circ$

Table 7.1: Main acoustic and geometric parameters of the UWA scenario.

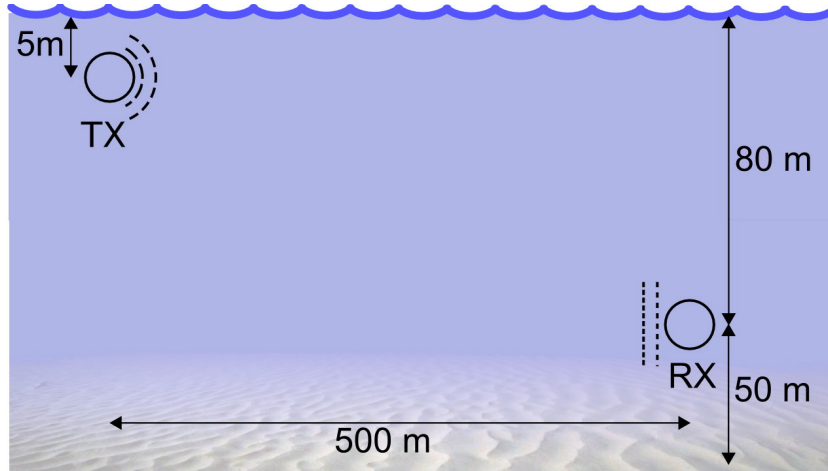


Figure 7.10: Geometry of the UWA link.

paths, namely the direct path and the two paths experiencing a single reflection from the surface or the bottom. The resulting power-delay profile for the geometry of Fig. 7.10 is identified in Tab. 7.2. Finally, the physical layer communications parameters used throughout the trials are specified in Tab. 7.3.

Path	Normalized power	Relative delay [ms]	Spectral shift [kHz]
0	0.402	0	0
1	0.393	16.11	2.86, 13.14
2	0.205	60.05	10.68, 5.32

Table 7.2: *Power-delay profile for the 3-path channel.*

T_{sw}	90 ms
T_P	$2T_{sw}$
\mathcal{M}	13.33
α	0.2
Symbol spacing	1 ms
Packet length	1024 symbols
Modulation	DQPSK
Codec	uncoded, BCH (1431, 2047)
f_L	18 kHz
f_H	34 kHz
T_{cor}	$8/(f_H - f_L)$

Table 7.3: *Physical layer parameters.*

The three-path channel defined by Tab. 7.2 was implemented in the NI testbed using the previously described model. In particular, the receiver input is generated by combining three versions of the transmitted waveform, each with a different delay and attenuation as specified in Tab. 7.2. The signal-to noise ratio (SNR), defined as the ratio between the average energy per symbol received through *all* paths to the noise power spectral density, is varied by injecting AWGN with variable spectral level.

Specifically, our purpose here is to compare the performance of the conventional receiver in [100] with that achievable by the three-branch parallel structure in Fig. 7.1. To this aim, we observe that, from (7.23) and from the values of Tab. 7.2, the maximum expected gain of the three-branch receiver is $G_R \approx 3.96$ dB. This margin seems to be actually available in view of the fact that the parameters $\delta\tau_{min}$ and $\delta\tau_{max}$ do largely satisfy condition (7.21): $\delta\tau_{max}/\delta\tau_{min} \approx 3.73 \ll \mathcal{M}-1$. Further to be

noted, since the three signal components can be exactly separated by the receiver, the relative phase rotations associated to the path gains are immaterial, and the receiver performance is only affected by the non-coherent power-delay profile. Figure 7.11 shows plots of the bit error rate (BER) vs. SNR obtained for uncoded transmission and error-free channel estimation and carrier/symbol synchronization in all receiver branches. The two curves of BER are relevant to the conventional single-branch ($K = 1$) and to the three-branch ($K = 3$) receivers. It is observed that the latter scheme asymptotically outperforms the former by around 4 dB, i.e., by the asymptotic gain G_R . Figure 7.12 shows curves of BER vs. SNR for the same single-branch and three-

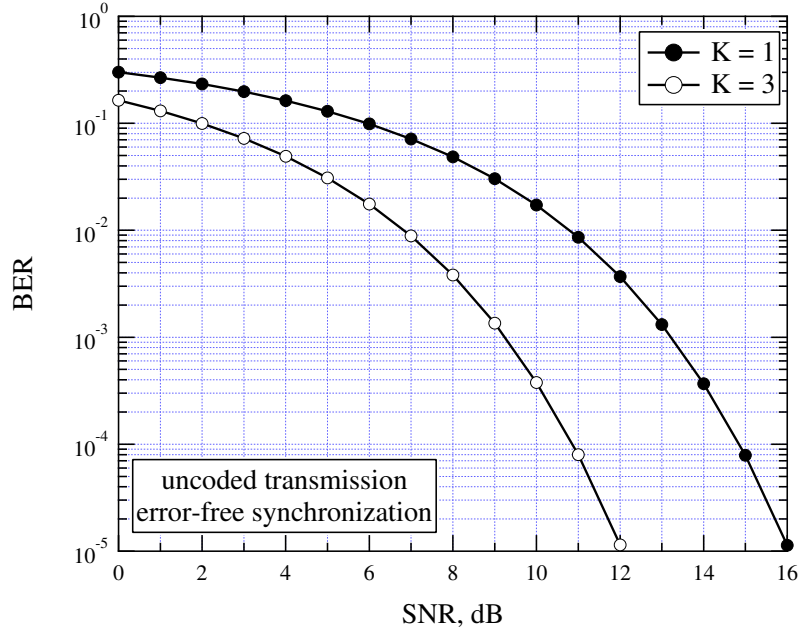


Figure 7.11: *BER vs SNR, uncoded transmission, 3-path channel, single-branch and three-branch receivers.*

branch receivers, obtained in the more realistic situation in which the transmitter employs a BCH encoder, with coding rate $r = 1431/2047 \simeq 0.7$ and the receiver actually incorporates the channel estimator and the carrier/symbol synchronizer. The benefit in terms of SNR gain provided by the multi-branch receiving structure is still apparent. For example, at $\text{BER} = 10^{-5}$ this gain is around the asymptotic value of 4 dB, while the advantage provided by the BCH encoder with respect to uncoded

transmission (curves in Fig. 7.11) is more than 3 dB.

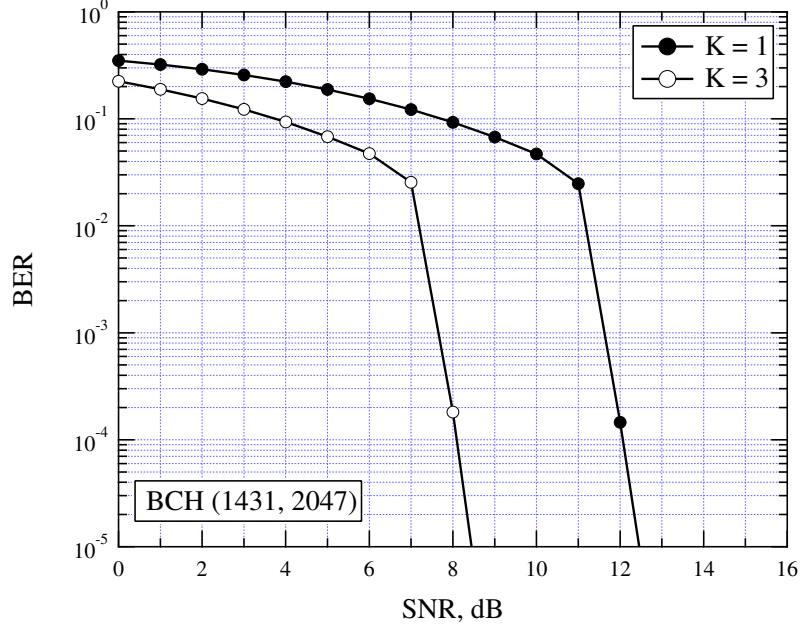


Figure 7.12: *BER vs SNR, coded transmission, 3-path channel, single-branch and three-branch receivers.*

It is now appropriate to briefly discuss the performance of the path delay estimator which, as we have seen, plays an important role for synchronization of the despreading waveforms in the multi-branch receiver, as well as for symbol timing recovery. As previously discussed, the delay is estimated by determining the instant at which the squared correlation (7.13) exhibits a peak. Of course, a necessary condition to get an accurate estimate is that the sampling rate at the receiver input be adequately high. The results presented here are obtained using a sampling rate of 100 kHz, a condition which, recalling the data of Tab. 7.3, corresponds to taking 100 samples per symbol and slightly more than 3 samples per cycle at the highest instantaneous frequency f_H of the waveform $c(t)$. In addition, to further improve the accuracy of the above estimator, we resorted to a parabolic interpolator operating on the highest sample of the squared correlation and on the adjacent two. This scheme was considered satisfactory insofar as a further increase of the sampling rate was observed not to entail any additional gain in terms of root mean square estimation error (RMSEE).

Figure 7.13 shows plots of RMSEE affecting the delay estimates for each path of the three-path scenario defined by Tabs. 7.1–7.3 as a function of SNR. As expected, the lowest curve is the one relevant to the strongest (direct) path ($k = 0$) while the other two curves, relative to the surface-reflected and bottom-reflected paths ($k = 1, 2$), are somewhat shifted versions of the former along the SNR axis, where the shifts are to be ascribed to the different (smaller) path gains. Also to be noted, when the SNR grows, all curves do not decrease indefinitely, but rather they tend asymptotically to different constant (floor) values. This behavior can be explained observing that even though the three signal replicas are sufficiently shifted from one another as to be uncorrelated, nevertheless they exert a mutual irreducible disturbance whose impact is felt even when the noise vanishes. Accordingly, the different floor levels are related to the different values of signal-to-mutual-interference existing between the signal replicas. Furthermore, we found that the delay estimates are substantially unbiased for all paths, and this holds true in general provided that the correlation peaks are well separated from one another, i.e., when conditions (7.21) are met.

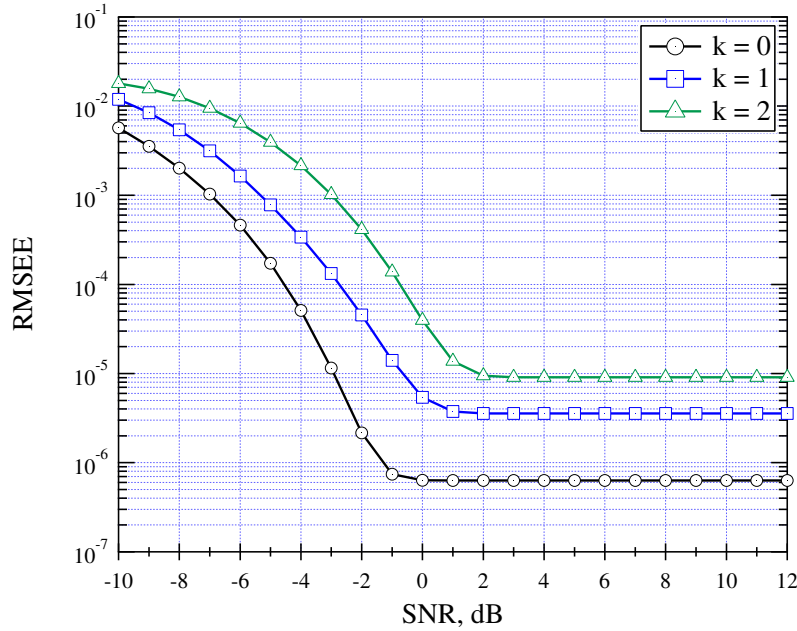


Figure 7.13: *RMSEE vs SNR, 3-path channel, delay estimate for $k = 0, 1, 2$.*

7.7 Concluding remarks

We have shown how to significantly improve the power efficiency of an S2C-based link, operating over a time-dispersive UWA channel, through the use of a multiple-branch parallel receiver structure, where each branch has the task to extract and process the signal received from one of the paths, and the outputs of the branches are finally combined together in an optimal way. In particular, we have identified the conditions allowing the signal replicas from the various paths to be exactly separated. A real-time version of the system has been implemented using a hardware testbed, and its performance has been assessed in laboratory over typical UWA channel models. For the common situation where in addition to the direct path there are also surface- and bottom-reflected paths of non-negligible level, we have shown that it is possible to achieve power gains of a few decibels in comparison with the traditional single-path-based receiver. We also presented an algorithm for synchronization of the despreading signal and for symbol timing recovery, and analyzed its impact on the receiver performance.

Chapter 8

VFIDES - An Autonomous Vehicle for Underwater Identification, Detection and Exploration

8.1 Introduction

In this chapter we highlight some aspects relevant to the activity carried out during the VFIDES project [103], [104]. First we report some details taken from the technical specification of the three main stages in which we were involved (out of a total of 23 for the entire project). Finally, to give an idea of the global complexity, the chapter concludes with a series of pictures about practical tests carried out during the project. At each deadline a technical report on the outcomes of the corresponding work packages was produced. Unfortunately the content of these documents is partially confidential and not all relevant results can be reproduced here in full detail.

The VFIDES project includes the development of an autonomous underwater vehicle (AUV) to be used for several missions such as:

- environmental monitoring of sea water;

- exploration of sea bottoms;
- monitoring of sea life;
- archaeological prospection.

VFIDES is also characterized by the ability to work either as AUV or as a remote controlled vehicle.

8.1.1 Features of the acoustic sensors and radio equipment

The first stage was primarily relevant to system analysis with the aim to outline functionalities and devices the vehicle should be equipped with, in order to satisfy the technical specifications. In particular the vehicle must be able to carry out missions involving exploration and monitoring of the underwater environment by gathering and storing information. Furthermore the AUV must be equipped with telemetry devices that allow the remote control of position, velocity and attitude as well as of equipment for data transmission from/to the mother ship. The arrangement of the devices within the volumes and surfaces available onboard had to take into account the mechanical and structural constraints of the hull.

Some key points of the activity were:

- evaluation of devices such as a side-scan sonar (SSS) or alternatively a multi-beam echo sounder (MBES) for exploration of the underwater environment;
- investigation of a hydrophone for passive environmental monitoring in a frequency band from few Hz to few tens of kHz;
- analysis of the underwater link when acoustic modems are employed and definition of minimum required performance in terms of range and bit rate;
- study of solutions for communications between the emerged AUV and the mother ship through direct radio link or by satellite modems with a particular attention on the antenna features (a pressure resistant case is necessary);
- proposal of devices for localization purpose.

8.1.2 Selection and performance evaluation of radio and sonar systems

Within this activity we first carried out market research to identify the appropriate commercial devices strictly complying with the technical specifications and whose typology and features were identified in the prior stage. Next, a performance evaluation step was necessary before the final purchase of the apparatus. For this task, computer modeling based on data provided by the manufacturer of the apparatus was developed and the simulation results carried out by emulating environmental conditions similar to those provided by the technical specification were compared with the expected performance. Finally, after the acquisition of all the devices, some on-field trials (parts of which are reported in section 8.2) were necessary to effectively verify the correct operation of the system, to optimize the parameters setting, and to make them ready for the successive step of integration.

8.1.3 Integration of acoustic and radio equipment

The target of this stage was relevant to the onboard integration of all the devices and the subsequent interfacing with the electronic control board (ECB) of the vehicle. The ECB contains the central processing unit and runs all the algorithms and procedures necessary to manage the execution of the operative missions. In particular the core functions supervised by the ECB pertain to:

- the acoustical and radio communication system;
- the management of all the active and passive transducers;
- the guidance, navigation and control algorithms.

Particular attention was put on the development of suitable software packages that can run on the ECB.

8.2 Experimental tests

Next we propose some highlights of the practical tests carried out during the project activities. The target of the trials was to validate and test the various devices in environmental conditions close to real operation scenarios. We remark that the

following is only a small selection of the test campaign necessary to correctly tune and validate all the devices and the related software.

8.2.1 Hydrophone testing and calibration

The performance evaluation of the hydrophone was carried out in a WASS facility near La Spezia. The aim of the test was to measure the performance of the device under different operating conditions and to compare these results with those provided by the manufacturer and by a sample hydrophone. Basically the test consisted in a series of measures realized with both the hydrophone under test and a calibrated hydrophone (used as benchmark) when a training acoustic signal was transmitted by the acoustic projectors. From the successive data analysis we obtained some curves of performance (for example sensitivity as a function of the frequency) useful to correctly calibrate the parameters of the hydrophone and to allow an improved use of the device. In Figs. 8.1–8.3 some particulars taken during the tests are shown.



Figure 8.1: *Particular of the test pool with the bridge crane and the rotating shaft.*



Figure 8.2: *Hydrophone under testing.*



Figure 8.3: *Projectors used throughout the tests.*

8.2.2 Pool test of the acoustic communication system

This type of test was carried out to verify the correctness of the acoustic communication process between the two modems. In addition, the accuracy of the USBL (ultra-short baseline) functionality, useful to measure the distance between the two nodes, was checked out. The primary target of the test was to establish a data connection between the two acoustic modems immersed in the water. The execution of the trials in a highly reverberant environment as a small pool was very useful to reproduce a severe multipath channel typical of shallow water communications. Figures 8.4–8.6 show the two modems and the test pool, within the WASS plant in Livorno.

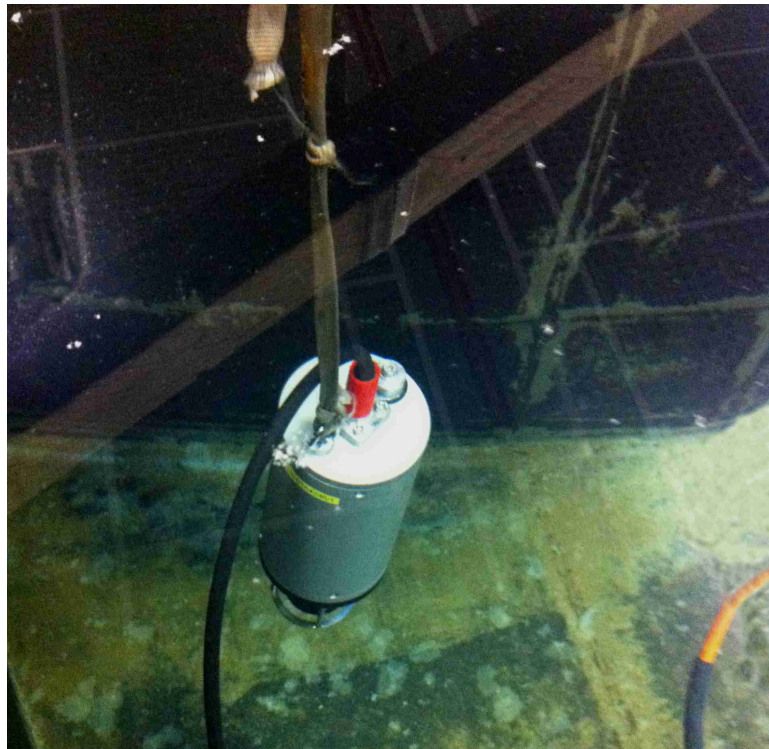


Figure 8.4: *Detail of the USBL modem.*

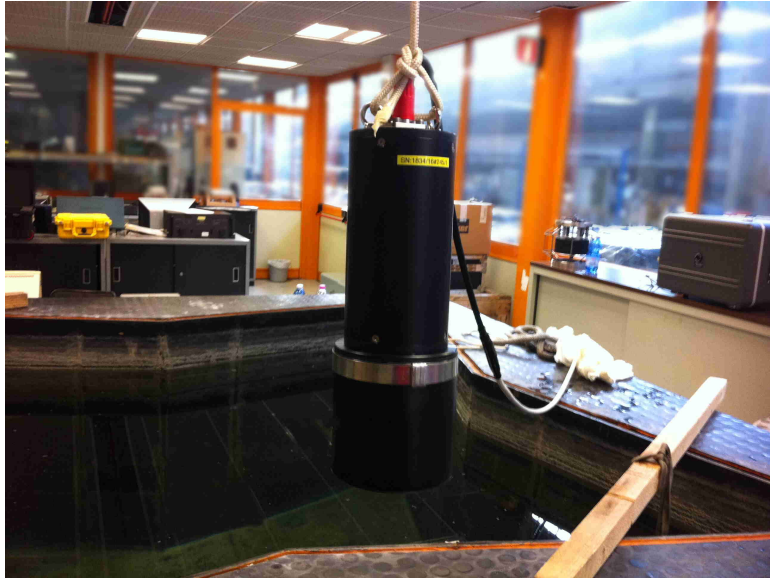


Figure 8.5: Detail of the modem hanged on a winch before the immersion.

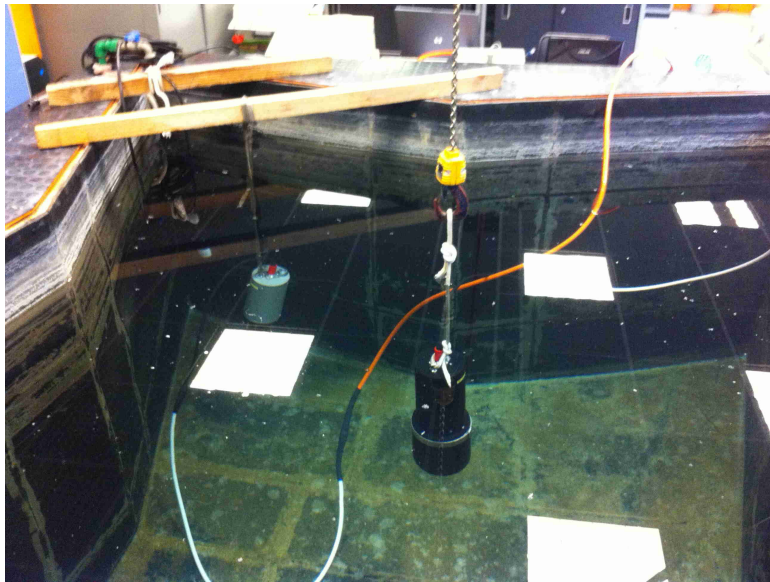


Figure 8.6: Modems lowered in the test pool.

8.2.3 Radio modem test over the sea surface

To better emulate the behavior of the radiocommunication system on a two-ray channel (typical of the over-the-sea links) we chose to carry out the test in conditions very similar to the real ones, even though the transmitting and receiving stations were placed on the mainland. The test consisted in a series of bit rate measures relevant to the connection established on a radio link between the two nodes with various settings of communication parameters and antenna positions. The trials took place on the Massaciuccoli lake and on the littoral zone of Viareggio. Some pictures relevant to the measure campaign are reported in Figs. 8.7–8.10.



Figure 8.7: *Receiving station during the test on Massaciuccoli lake.*



Figure 8.8: *Transmitting station during the test in Viareggio.*



Figure 8.9: *Detail of the modem connections to control station and antenna.*



Figure 8.10: *Paths of the tested radio links highlighted on a map.*

8.2.4 The VFIDES

Finally in Fig. 8.11 we show a picture of the final version of the vehicle equipped with all the devices and fully functioning.



Figure 8.11: *The VFIDES.*

Conclusions

This work mainly deals with a deep investigation of some specific aspects concerning synchronization issues in wireless communication systems based on a multicarrier air-interface. Not only many of the current commercial standards are based on this technology but the adoption of multicarrier signaling format is expected to be a consolidated basis for future generation systems. Although the major design challenges will turn the attention to higher layer and network operation aspects, synchronization procedures and algorithms, mainly relating to frequency reuse and cross-interference management, will remain key aspects in systems involving technologies of which cooperative communications, cognitive radio, massive MIMO, small-cells and overlay networks, represent only a few examples and whose strong investigation in many research centers is tracing the route towards 5G and beyond.

Bibliography

- [1] *Measuring the Information Society Report 2014*. International Telecommunication Union.
- [2] M.-o. Pun, M. Morelli, and C. C. J. Kuo, *Multi-Carrier Techniques For Broadband Wireless Communications: A Signal Processing Perspectives*. London, UK, UK: Imperial College Press, 2007.
- [3] G. Cherubini, “Filter-bank modulation techniques for transmission over frequency-selective channels,” in *Signal Processing for Mobile Communications Handbook*, M. Ibnkahla, Ed. CRC PressINC, 2005.
- [4] S. M. Kay, *Fundamentals of Statistical Signal Processing: Estimation Theory*. Prentice-Hall, Inc., 1993.
- [5] J. Proakis and M. Salehi, *Digital Communications, 5th Ed*. McGraw-Hill, 2007.
- [6] D. Fudenberg and J. Tirole, *Game Theory*. The MIT Press, 1991.
- [7] X. Lurton, *An Introduction to Underwater Acoustics: Principles and Applications*, ser. Geophysical Sciences Series. Springer, 2002.
- [8] C. Ciochina, D. Mottier, and H. Sari, “An analysis of three multiple access techniques for the uplink of future cellular mobile systems,” *European Transactions on Telecommunications*, vol. 19, no. 5, pp. 581–588, 2008.
- [9] 3GPP, “Evolved Universal Terrestrial Radio Access (E-UTRA); Physical channels and modulation,” 3rd Generation Partnership Project (3GPP), TS 36.211, Sep. 2011.

- [10] R. Müllner, C. F. Ball, M. Boussif, J. Lienhart, P. Hric, H. Winkler, K. Kremnitzer, and R. Kronlachner, "Enhancing uplink performance in UTRAN LTE networks by load adaptive power control," *European Transactions on Telecommunications*, vol. 21, no. 5, pp. 458–468, 2010.
- [11] "IEEE standard for local and metropolitan area networks part 16: Air interface for broadband wireless access systems," *IEEE Std 802.16-2009 (Revision of IEEE Std 802.16-2004)*, pp. 1–2080, May 2009.
- [12] L. Li, P. Zhou, H. Hu, and X. Zhang, "A robust cell search scheme for OFDMA systems," *European Transactions on Telecommunications*, vol. 19, no. 8, pp. 935–940, 2008.
- [13] X. Fu and H. Minn, "Initial uplink synchronization and power control (ranging process) for OFDMA systems," in *Global Telecommunications Conference, 2004. GLOBECOM '04. IEEE*, vol. 6, 2004, pp. 3999–4003 Vol.6.
- [14] D. H. Lee, "OFDMA uplink ranging for IEEE 802.16e using modified generalized chirp-like polyphase sequences," in *Internet, 2005. The First IEEE and IFIP International Conference in Central Asia on*, 2005, pp. 1–5.
- [15] Y. Zhou, Z. Zhang, and X. Zhou, "OFDMA initial ranging for IEEE 802.16e based on time-domain and frequency-domain approaches," in *Communication Technology, 2006. ICCT '06. International Conference on*, 2006, pp. 1–5.
- [16] H. Mahmoud, H. Arslan, and M. Ozdemir, "Initial ranging for WiMAX (802.16e) OFDMA," in *Military Communications Conference, 2006. MILCOM 2006. IEEE*, 2006, pp. 1–7.
- [17] S. Sesia, I. Toufik, and M. Baker, *LTE - The UMTS Long Term Evolution: From Theory to Practice*. Wiley, 2009.
- [18] X. Zhuang, K. Baum, V. Nangia, and C. M., "Ranging improvement for 802.16e OFDMA PHY," in *IEEE C802.16e-04/143*, 2004, pp. 1–32.
- [19] X. Fu, Y. Li, and H. Minn, "A new ranging method for OFDMA systems," *Wireless Communications, IEEE Transactions on*, vol. 6, no. 2, pp. 659–669, 2007.

- [20] M. Morelli, L. Sanguinetti, and H. Poor, "A robust ranging scheme for OFDMA-based networks," *Communications, IEEE Transactions on*, vol. 57, no. 8, pp. 2441–2452, 2009.
- [21] L. Sanguinetti, M. Morelli, and H. Poor, "An ESPRIT-based approach for initial ranging in OFDMA systems," *Communications, IEEE Transactions on*, vol. 57, no. 11, pp. 3225–3229, 2009.
- [22] L. Sanguinetti and M. Morelli, "An initial ranging scheme for the IEEE 802.16 OFDMA uplink," *Wireless Communications, IEEE Transactions on*, vol. 11, no. 9, pp. 3204–3215, September 2012.
- [23] W. W. Smith and J. M. Smith, *Handbook of real-time fast Fourier transforms: algorithms to product testing*. New York, NY: IEEE Computer Society Press, 1995.
- [24] ITU-R, "Guidelines for evaluation of radio transmission technology for IMT-2000," in *Recommendation ITU-R M. 1225, Tech. Rep.*, 1997, pp. 1–60.
- [25] T. Schmidl and D. Cox, "Robust frequency and timing synchronization for OFDM," *Communications, IEEE Transactions on*, vol. 45, no. 12, pp. 1613–1621, 1997.
- [26] M. Morelli and U. Mengali, "An improved frequency offset estimator for OFDM applications," *Communications Letters, IEEE*, vol. 3, no. 3, pp. 75–77, 1999.
- [27] H. Minn, V. Bhargava, and K. Letaief, "A robust timing and frequency synchronization for OFDM systems," *Wireless Communications, IEEE Transactions on*, vol. 2, no. 4, pp. 822–839, 2003.
- [28] "IEEE standard for information technology- telecommunications and information exchange between systems- local and metropolitan area networks- specific requirements- part 11: Wireless LAN medium access control (MAC) and physical layer (PHY) specifications," *ANSI/IEEE Std 802.11, 1999 Edition (R2003)*, pp. i–513, 2003.
- [29] M. Morelli and M. Moretti, "Integer frequency offset recovery in OFDM transmissions over selective channels," *Wireless Communications, IEEE Transactions on*, vol. 7, no. 12, pp. 5220–5226, 2008.

- [30] K. Pushpa, C. Kishore, and Y. Yoganandam, "A new method for frame synchronization in OFDMA mode of WMAN," in *TENCON 2008 - 2008 IEEE Region 10 Conference*, 2008, pp. 1–6.
- [31] T. Bhatt, V. Sundaramurthy, J. Zhang, and D. McCain, "Initial synchronization for 802.16e downlink," in *Signals, Systems and Computers, 2006. ACSSC '06. Fortieth Asilomar Conference on*, 2006, pp. 701–706.
- [32] F. Suliman, N. Elhassan, and T. Ibrahim, "Frequency offset estimation and cell search algorithms for OFDMA based mobile WiMAX," in *Advanced Communication Technology (ICACT), 2012 14th International Conference on*, 2012, pp. 1128–1131.
- [33] T. Hurnanen, J. Poikonen, and J. Paavola, "Coarse time- and frequency synchronization applied in a mobile WiMAX system," in *Wireless Communication Systems, 2009. ISWCS 2009. 6th International Symposium on*, 2009, pp. 230–233.
- [34] J.-J. van de Beek, M. Sandell, and P. Borjesson, "ML estimation of time and frequency offset in OFDM systems," *Signal Processing, IEEE Transactions on*, vol. 45, no. 7, pp. 1800–1805, 1997.
- [35] K. Pushpa, C. Kishore, and Y. Yoganandam, "Estimation of frequency offset, cell ID and CP length in OFDMA mode of WMAN," in *TENCON 2008 - 2008 IEEE Region 10 Conference*, 2008, pp. 1–5.
- [36] M. Ruan, M. Reed, and Z. Shi, "A universal frequency offset estimator for OFDM applications," in *Global Telecommunications Conference, 2009. GLOBECOM 2009. IEEE*, 2009, pp. 1–5.
- [37] H. Zhou, H. Hayashi, T. Kubo, and J. Zhang, "A novel carrier frequency offset estimation method for IEEE 802.16e system," in *Global Telecommunications Conference, 2007. GLOBECOM '07. IEEE*, 2007, pp. 2826–2830.
- [38] J. Choi, M. Park, S. Cha, and H.-S. Lee, "An adaptive cell search and integral frequency offset estimation in mobile WiMAX," in *Vehicular Technology Conference, 2009. VTC Spring 2009. IEEE 69th*, 2009, pp. 1–5.

- [39] J.-H. Deng, S.-H. Chang, J.-K. Hwang, and S.-M. Liao, "A differential cross-correlation cell search algorithm for IEEE 802.16e OFDMA systems," in *Vehicle Technology Conference (VTC 2010-Spring), 2010 IEEE 71st*, 2010, pp. 1–5.
- [40] Y.-C. Lin, S.-L. Su, and H.-C. Wang, "A low complexity cell search method for IEEE 802.16e OFDMA systems," in *Advanced Communication Technology, 2009. ICACT 2009. 11th International Conference on*, vol. 02, 2009, pp. 980–984.
- [41] K.-C. Hung and D. Lin, "Joint detection of integral carrier frequency offset and preamble index in OFDMA wimax downlink synchronization," in *Wireless Communications and Networking Conference, 2007. WCNC 2007. IEEE*, 2007, pp. 1959–1964.
- [42] J. Lee, J. Choi, and H.-L. Lou, "Joint maximum likelihood estimation of channel and preamble sequence for WiMAX systems," *Wireless Communications, IEEE Transactions on*, vol. 7, no. 11, pp. 4294–4303, 2008.
- [43] J.-S. Sheu and W.-H. Sheen, "Characteristics and modelling of inter-cell interference for orthogonal frequency-division multiple access systems in multipath rayleigh fading channels," *Communications, IET*, vol. 6, no. 17, pp. 3015–3025, 2012.
- [44] S. Sorooshyari, C. wei Tan, and H. Poor, "On maximum-likelihood SINR estimation of MPSK in a multiuser fading channel," *Vehicle Technology, IEEE Transactions on*, vol. 59, no. 8, pp. 4175–4181, 2010.
- [45] M. Ghogho, A. Swami, and P. Ciblat, "Training design for CFO estimation in OFDM over correlated multipath fading channels," in *Global Telecommunications Conference, 2007. GLOBECOM '07. IEEE*, 2007, pp. 2821–2825.
- [46] M. J., "FFT pruning," *Audio and Electroacoustics, IEEE Transactions on*, vol. 19, no. 4, pp. 305–311, 1971.
- [47] F. Gini and R. Reggiannini, "On the use of cramer-rao-like bounds in the presence of random nuisance parameters," *Communications, IEEE Transactions on*, vol. 48, no. 12, pp. 2120–2126, 2000.

- [48] "Supplement to IEEE standard for information technology - telecommunications and information exchange between systems - local and metropolitan area networks - specific requirements. part 11: Wireless LAN medium access control (MAC) and physical layer (PHY) specifications: High-speed physical layer in the 5 GHz band," *IEEE Std 802.11a-1999*.
- [49] W. Namgoong and T. Meng, "Direct-conversion RF receiver design," *Communications, IEEE Transactions on*, vol. 49, no. 3, pp. 518–529, Mar 2001.
- [50] B. Razavi, "Design considerations for direct-conversion receivers," *Circuits and Systems II: Analog and Digital Signal Processing, IEEE Transactions on*, vol. 44, no. 6, pp. 428–435, Jun 1997.
- [51] F. Yan, W.-P. Zhu, and M. Ahmad, "Carrier frequency offset estimation for OFDM systems with I/Q imbalance," in *Circuits and Systems, 2004. MWSCAS '04. The 2004 47th Midwest Symposium on*, vol. 2, July 2004, pp. II-633–II-636 vol.2.
- [52] L. Lanante, M. Kurosaki, and H. Ochi, "Low complexity compensation of frequency dependent I/Q imbalance and carrier frequency offset for direct conversion receivers," in *Circuits and Systems (ISCAS), Proceedings of 2010 IEEE International Symposium on*, May 2010, pp. 2067–2070.
- [53] H. Lin, X. Zhu, and K. Yamashita, "Low-complexity pilot-aided compensation for carrier frequency offset and I/Q imbalance," *Communications, IEEE Transactions on*, vol. 58, no. 2, pp. 448–452, February 2010.
- [54] S. De Rore, E. Lopez-Estraviz, F. Horlin, and L. Van der Perre, "Joint estimation of carrier frequency offset and IQ imbalance for 4G mobile wireless systems," in *Communications, 2006. ICC '06. IEEE International Conference on*, vol. 5, June 2006, pp. 2066–2071.
- [55] Y.-C. Pan and S.-M. Phoong, "A new algorithm for carrier frequency offset estimation in the presence of I/Q imbalance," in *Vehicular Technology Conference (VTC 2010-Spring), 2010 IEEE 71st*, May 2010, pp. 1–5.
- [56] M. Morelli and M. Moretti, "Carrier frequency offset estimation for OFDM direct-conversion receivers," *Wireless Communications, IEEE Transactions on*, vol. 11, no. 7, pp. 2670–2679, July 2012.

- [57] G. Xing, M. Shen, and H. Liu, "Frequency offset and I/Q imbalance compensation for direct-conversion receivers," *Wireless Communications, IEEE Transactions on*, vol. 4, no. 2, pp. 673–680, March 2005.
- [58] J. Park, Y. Lee, and H. Park, "Preamble design for joint estimation of CFO and I/Q imbalance for direct conversion OFDM system," *Communications, IET*, vol. 3, no. 4, pp. 597–602, April 2009.
- [59] Y.-C. Pan and S.-M. Phoong, "A time-domain joint estimation algorithm for CFO and I/Q imbalance in wideband direct-conversion receivers," *Wireless Communications, IEEE Transactions on*, vol. 11, no. 7, pp. 2353–2361, July 2012.
- [60] X. Wang, Y. Xue, L. Liu, F. Ye, and J. Ren, "Carrier frequency offset estimation in the presence of I/Q mismatch for wideband OFDM systems," in *Circuits and Systems (MWSCAS), 2012 IEEE 55th International Midwest Symposium on*, Aug 2012, pp. 924–927.
- [61] R. Kume, H. Lin, and K. Yamashita, "Repeated preamble based carrier frequency offset estimation in the presence of I/Q imbalance," in *Communications (ICC), 2012 IEEE International Conference on*, June 2012, pp. 4867–4871.
- [62] M. Morelli and H. Lin, "ESPRIT-based carrier frequency offset estimation for OFDM direct-conversion receivers," *Communications Letters, IEEE*, vol. 17, no. 8, pp. 1513–1516, August 2013.
- [63] M. Morelli and M. Moretti, "A SAGE approach to frequency recovery in OFDM direct-conversion receivers," *Communications Letters, IEEE*, vol. 18, no. 4, pp. 536–539, April 2014.
- [64] U. Tureli, H. Liu, and M. Zoltowski, "OFDM blind carrier offset estimation: ESPRIT," *Communications, IEEE Transactions on*, vol. 48, no. 9, pp. 1459–1461, Sep 2000.
- [65] J. Fessler and A. Hero, "Space-alternating generalized expectation-maximization algorithm," *Signal Processing, IEEE Transactions on*, vol. 42, no. 10, pp. 2664–2677, Oct 1994.

- [66] M. Valkama, M. Renfors, and V. Koivunen, "Advanced methods for I/Q imbalance compensation in communication receivers," *Signal Processing, IEEE Transactions on*, vol. 49, no. 10, pp. 2335–2344, Oct 2001.
- [67] M. Meyers and L. Franks, "Joint carrier phase and symbol timing recovery for PAM systems," *Communications, IEEE Transactions on*, vol. 28, no. 8, pp. 1121–1129, Aug 1980.
- [68] G. Cherubini, E. Eleftheriou, and S. Ölçer, "Filtered multitone modulation for very high-speed digital subscriber lines," *Selected Areas in Communications, IEEE Journal on*, vol. 20, no. 5, pp. 1016–1028, 2002.
- [69] ETSI, "Digital Video Broadcasting (DVB); Interaction channel for Digital Terrestrial Television (RCT) incorporating Multiple Access OFDM," European Telecommunications Standards Institute (ETSI), EN 301 958, 2002.
- [70] M. Nouri, V. Lottici, R. Reggiannini, D. Ball, and M. Rayne, "TEDS: A high speed digital mobile communication air interface for professional users," *Vehicular Technology Magazine, IEEE*, vol. 1, no. 4, pp. 32–42, 2006.
- [71] V. Lottici, R. Reggiannini, and M. Carta, "Pilot-aided carrier frequency estimation for filter-bank multicarrier wireless communications on doubly-selective channels," *Signal Processing, IEEE Transactions on*, vol. 58, no. 5, pp. 2783–2794, 2010.
- [72] M. Moretti, V. Lottici, R. Reggiannini, and G. Dainelli, "Combined pilot-aided and decision-directed carrier synchronization for filtered multitone wireless systems," *Wireless Communications, IEEE Transactions on*, vol. 12, no. 2, pp. 748–757, 2013.
- [73] O. Takeshita and D. Costello, "New deterministic interleaver designs for turbo codes," *Information Theory, IEEE Transactions on*, vol. 46, no. 6, pp. 1988–2006, 2000.
- [74] ETSI, "Terrestrial Trunked Radio (TETRA); Release 2; Designer's Guide; TETRA High-Speed Data (HSD); TETRA Enhanced Data Service (TEDS)," European Telecommunications Standards Institute (ETSI), TR 102 580, Oct. 2007.

- [75] G. Auer, O. Blume, V. Giannini, I. Godor, M. Imran, Y. Jading, E. Kataranaras, M. Olsson, D. Sabella, P. Skillermark *et al.*, “D2.3: Energy efficiency analysis of the reference systems, areas of improvements and target breakdown,” *INFSOICT-247733 EARTH (Energy Aware Radio and NeTwork TecHnologies)*, Tech. Rep, 2010.
- [76] Y. Chen, S. Zhang, S. Xu, and G. Li, “Fundamental trade-offs on green wireless networks,” *Communications Magazine, IEEE*, vol. 49, no. 6, pp. 30–37, June 2011.
- [77] The Climate Group, “SMART 2020: Enabling the low carbon economy in the information age,” Tech. Rep., 2008.
- [78] <http://www.greentouch.org>.
- [79] S. Lasaulce and H. Tembine, *Game Theory and Learning for Wireless Networks: Fundamentals and Applications*, 1st ed. Academic Press, 2011.
- [80] G. Miao, N. Himayat, and G. Li, “Energy-efficient link adaptation in frequency-selective channels,” *Communications, IEEE Transactions on*, vol. 58, no. 2, pp. 545–554, February 2010.
- [81] G. Miao, N. Himayat, G. Li, and S. Talwar, “Distributed interference-aware energy-efficient power optimization,” *Wireless Communications, IEEE Transactions on*, vol. 10, no. 4, pp. 1323–1333, April 2011.
- [82] G. Bacci, E. Belmega, and L. Sanguinetti, “Distributed energy-efficient power optimization in cellular relay networks with minimum rate constraints,” in *Acoustics, Speech and Signal Processing (ICASSP), 2014 IEEE International Conference on*, May 2014, pp. 7014–7018.
- [83] C. Koksai and P. Schniter, “Robust rate-adaptive wireless communication using ACK/NAK-feedback,” *Signal Processing, IEEE Transactions on*, vol. 60, no. 4, pp. 1752–1765, April 2012.
- [84] R. Aggarwal, C. Koksai, and P. Schniter, “Joint scheduling and resource allocation in OFDMA downlink systems via ACK/NAK feedback,” *Signal Processing, IEEE Transactions on*, vol. 60, no. 6, pp. 3217–3227, June 2012.

- [85] S. Huang, X. Liu, and Z. Ding, "Distributed power control for cognitive user access based on primary link control feedback," in *INFOCOM, 2010 Proceedings IEEE*, March 2010, pp. 1–9.
- [86] E. Belmega, H. Tembine, and S. Lasaulce, "Learning to precode in outage minimization games over MIMO interference channels," in *Signals, Systems and Computers (ASILOMAR), 2010 Conference Record of the Forty Fourth Asilomar Conference on*, Nov 2010, pp. 261–266.
- [87] F. Facchinei and C. Kanzow, "Generalized nash equilibrium problems," *4OR*, vol. 5, no. 3, pp. 173–210, 2007.
- [88] S. Pillai, T. Suel, and S. Cha, "The perron-frobenius theorem: some of its applications," *Signal Processing Magazine, IEEE*, vol. 22, no. 2, pp. 62–75, March 2005.
- [89] R. Yates, "A framework for uplink power control in cellular radio systems," *Selected Areas in Communications, IEEE Journal on*, vol. 13, no. 7, pp. 1341–1347, Sep 1995.
- [90] C. Saraydar, N. B. Mandayam, and D. Goodman, "Efficient power control via pricing in wireless data networks," *Communications, IEEE Transactions on*, vol. 50, no. 2, pp. 291–303, Feb 2002.
- [91] R. G. Gallager, *Information Theory and Reliable Communication*. John Wiley & Sons, Inc., 1968.
- [92] J. Hoydis, M. Kobayashi, and M. Debbah, "Green small-cell networks," *Vehicular Technology Magazine, IEEE*, vol. 6, no. 1, pp. 37–43, March 2011.
- [93] 3GPP, "Evolved Universal Terrestrial Radio Access (E-UTRA); Further advancements for E-UTRA physical layer aspects," 3rd Generation Partnership Project (3GPP), TR 36.814, Mar. 2010.
- [94] D. Kilfoyle and A. Baggeroer, "The state of the art in underwater acoustic telemetry," *Oceanic Engineering, IEEE Journal of*, vol. 25, no. 1, pp. 4–27, Jan 2000.

- [95] E. Sozer, M. Stojanovic, and J. Proakis, "Underwater acoustic networks," *Oceanic Engineering, IEEE Journal of*, vol. 25, no. 1, pp. 72–83, Jan 2000.
- [96] M. Stojanovic and J. Preisig, "Underwater acoustic communication channels: Propagation models and statistical characterization," *Communications Magazine, IEEE*, vol. 47, no. 1, pp. 84–89, January 2009.
- [97] P. van Walree, "Propagation and scattering effects in underwater acoustic communication channels," *Oceanic Engineering, IEEE Journal of*, vol. 38, no. 4, pp. 614–631, Oct 2013.
- [98] M. Stojanovic, J. Catipovic, and J. Proakis, "Phase-coherent digital communications for underwater acoustic channels," *Oceanic Engineering, IEEE Journal of*, vol. 19, no. 1, pp. 100–111, Jan 1994.
- [99] S. Zhou and Z. Wang, *OFDM for Underwater Acoustic Communications*. John Wiley & Sons, Ltd, 2014.
- [100] K. G. Kebkal and R. Bannasch, "Sweep-spread carrier for underwater communication over acoustic channels with strong multipath propagation," *The Journal of the Acoustical Society of America*, vol. 112, no. 5, pp. 2043–2052, 2002.
- [101] <http://www.ni.com/>.
- [102] <http://oalib.hlsresearch.com/>.
- [103] <http://opencoesione.gov.it/progetti/6to447895/>.
- [104] A. Caiti, F. Di Corato, D. Fenucci, S. Grechi, M. Novi, F. Pacini, and G. Paoli, "The Project V-FIDES: a new generation AUV for deep underwater exploration, operation and monitoring," in *OCEANS - St Johns, 2014 MTS/IEEE*, September 2014.